Kinematic Fitting On CLAS EG6

Exclusive Coherent π^0 Electroproduction Off ^{4}He

Frank Thanh Cao

Abstract

Careful event selection is paramount for extracting a meaningful beam-spin asymmetry. Even with positively identified particles, event selection is needed to discriminate whether a set of particles is from the process of interest or just background. The standard event selection, known as exclusivity cuts, relies on forming exclusivity variables from measured 4-momenta, and then cutting on their various distributions around the expected values. Additional cuts are often developed to further clean the sample.

A confrontation needs to be made with the fact that measurements from detectors are not perfect; it may be possible to improve both the measurements and the method of event selection. Here, an alternative to the standard event selection, called kinematic fitting, is presented. Kinematic fitting is an event-by-event method that allows for all measured 4-momenta to simulataneously move around, within detector resolutions, to better satisfy the constraints of conservation of momentum and energy. Sets of particles insufficiently conserving energy and momentum with respect to the hypothesis of the process of interest can be ruled out as background events.

Kinematic fitting is applied to EG6 data for the first time and a comparison with exclusivity cuts is shown with some surprising results.

Contents

I. Introduction

1. Overview

The CLAS EG6 experiment is a unique experiment, with its gas ^{4}He target, to study fully exclusive nuclear processes of Deeply Virtual Compton Scattering (DVCS):

$$e\ {}^4\text{He} \to e\ {}^4\text{He}\ \gamma \tag{1.1}$$

and Deeply Virtual Meson Production (DVMP):

$$\begin{gathered} e\ {}^4\text{He} \to e\ {}^4\text{He}\ \pi^0 \\ e\ {}^4\text{He} \to e\ {}^4\text{He}\ \eta \end{gathered} \tag{1.2}$$

The existing CLAS measures the scattered electron, the addition of the Inner Calorimeter (IC) allows for detecting high energy, low-polar-angle photons and the addition of the Radial Time Projection Chamber (RTPC) allows for detecting low-momentum recoiled ^{4}He nuclei (discussed in **Chapter II.**).

To study full exclusivity, every particle (or its decay products) on both sides of **Eq. 1.1** and **Eqs. 1.2** needs to be identified. The initial ^{4}He is taken to be at rest and the initial electron is taken to be from the beam. Particle identification of the final state particles follows the procedure outlined in [1] and is shown in full in **Chapter III.**. Identification of the scattered electron, the scattered ^{4}He, and the produced photons then suffices the full exclusivity of **Eq. 1.1** since π^0 and η are reconstructed through its decay into two photons (with a 98.8% branching ratio for π^0 [2] and 39.4% for η [3]).

Event selection is then required to take these positively identified particles into a set of particles involved in the aforementioned exclusive process. The accepted standard event selection is done through a series of exclusivity cuts that is ubiquitous in analyses including similar studies done in [1] and [4], among many others (discussed in **Chapter IV.**). As an improvement, this thesis introduces kinematic fitting as event selection following the nonlinear least-squares fit formalism of A. G. Frodesen [5] (discussed in **Chapter V.**). Though this is not the first time kinematic fitting has been used in CLAS (previous works in CLAS [6–10]), it is, however, a first look at kinematic fitting applied to electron scattering off nuclei. Both event selection methods will be described and their results are then compared in **Chapter IX.**.

To check the robustness of the kinematic fitting procedure, the fit is first applied for coherent Deeply Virtual Compton Scattering (DVCS) :

$$e\ {}^4\mathrm{He} \rightarrow e\ {}^4\mathrm{He}\ \gamma \tag{1.3}$$

event selection, using only conservation of momentum and energy of an exclusive process (discussed in **Section 10.**). This starting point has many advantages: the particles involved are convenient –every particle involved DVCS is also involved in DVπ^0P; there are fewer particles involved in this reaction so all correlations entering the construction of the fit can be better isolated and studied; and there are many more events –the results will not be limited by statistics and the shapes of the distributions are better characterized.

Naturally, by just including another photon into the fit, we can begin to look at coherent DVπ^0P events:

$$e\ {}^4\mathrm{He} \rightarrow e\ {}^4\mathrm{He}\ \gamma\ \gamma, \tag{1.4}$$

discussed in **Section VIII.**. Here, the power of kinematic fitting coupled with exclusivity is fully exemplified. The fit, termed a $4C$-fit, only uses conservation of momentum and energy of the particles in **Eq. 1.4**. However, when looking at the invariant mass of distribution of two selected photons, a clear peak with very little background is shown at the nominal value of M_{π^0} without the nominal value being mentioned anywhere in the fit.

To ensure the events selected are from coherent DVπ^0P events, an additional invariant mass cut on the photon pair can be applied.

Finally, a fit which also includes the decay of the π^0:

$$\begin{gathered} e\ {}^4\text{He} \rightarrow e\ {}^4\text{He}\ \pi^0 \\ \pi^0 \rightarrow \gamma\ \gamma \end{gathered} \quad , \tag{1.5}$$

termed a 5C-fit, is introduced and deployed (discussed in **Section VIII.**). The results of this final 5C-fit is compared to the results of the previously studied exclusivity cuts for event selection, discussed in **Chapter IX.**.

Once we have the selected events, by whichever method, an extraction of the beam-spin asymmetry (BSA) of the longitudinally polarized electron beam on an unpolarized, spin-0 helium target is measured, represented as A_{LU}:

$$A_{LU}(\phi) = \left(\frac{1}{P_B}\right)\frac{N^+(\phi) - N^-(\phi)}{N^+(\phi) + N^-(\phi)} \quad ,$$

where

- ϕ is the angle between the leptonic plane (formed by the beam and scattered electron) and the hadronic plane (formed by the initial and final ^{4}He),
- $N^{\pm}$ is the positive (+) and negative (-) counts of the beam helicity, and
- P_B is the beam polarization.

This measurement can be compared to the model-independent expression:

$$A_{LU} = \frac{\alpha \sin\phi}{1 + \beta\cos\phi + \gamma\cos 2\phi} \tag{1.6}$$

where α, β, and γ are parametrized by kinematics and structure functions.

By measuring this asymmmetry, we can gain access to generalized parton distributions (GPDs), that encode the spatial distribution of quarks inside the nucleon and the nucleus, through the structure functions.

II. CLAS EG6 Experimental Setup

Since particle identification of only the electron, helium, and photons are required, the experimental setup will only focus on the accelerator, the target, and the detectors involved in identifying these particles. The rest of the detectors, all pictured in **Fig. 2.1b**, will be skipped over as many of them are fully described in other theses and papers [1, 4, 11].

2. Existing CEBAF and CLAS

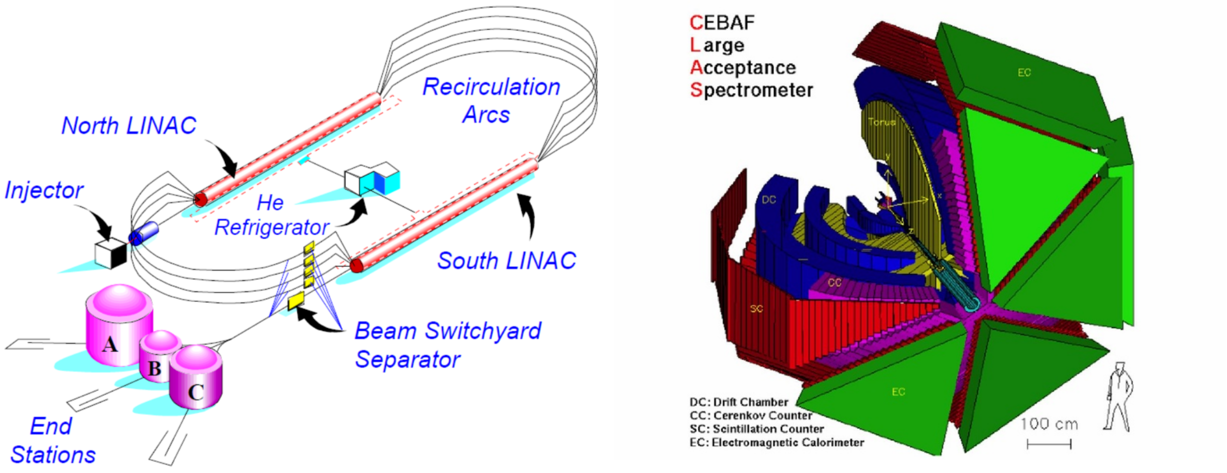

(a) CEBAF layout [4]

(b) Color-coded GEANT simulation view of CLAS [4]

Figure 2.1: CEBAF (a) and CLAS (b) [4]

2.1 Continuous Electron Beam Accelerator Facility (CEBAF)

CEBAF is capable of delivering a continuous polarized 6 GeV electron beam with luminosity of a few 10^{38} cm^{2}s^{-1}. Polarized electrons start at the polarized photocathode injector with 67 MeV and are accelerated through 5 successive orbits of CEBAF, pictured in **Fig. 2.1a**, to achieve energies up to 6.064 GeV with up to 85% polarization [4]. The beam is delivered to three experimental halls, A, B, and C end stations where different detectors are set up for different experiments. Hall B, where CLAS is housed, is delivered electron beam with a luminosity 10^{34} cm^{2}s^{-1}, but makes up for the loss with CLAS' high solid-angle acceptance of about 4π.

2.2 CEBAF Large Acceptance Spectrometer (CLAS)

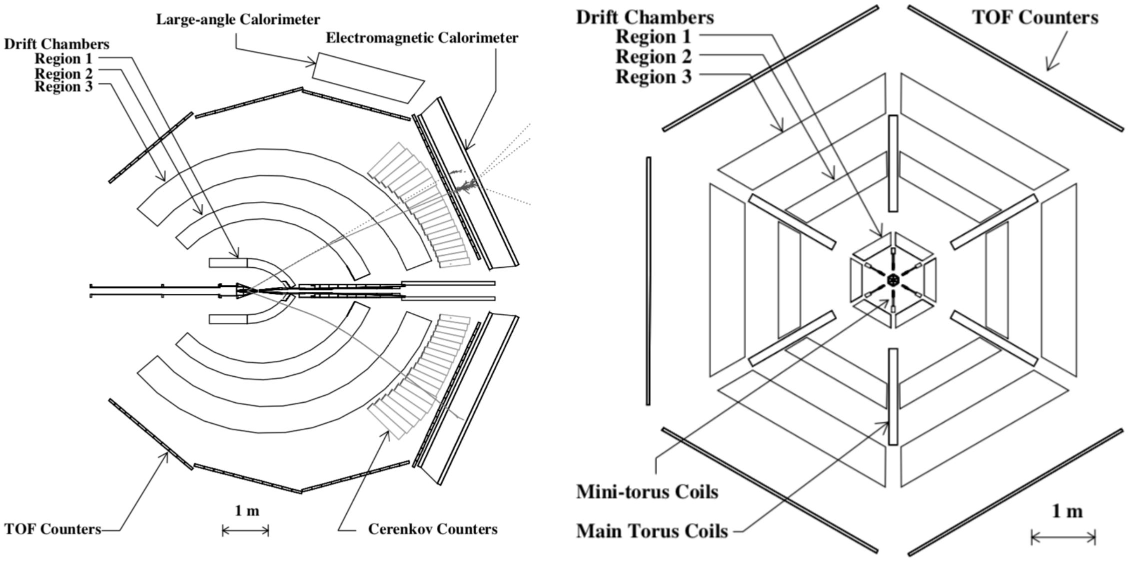

(**a**) CLAS profile

(**b**) CLAS face

Figure 2.2: Schematic view of CLAS [12]

The existing CLAS uses an array of detectors to detect and to distinguish particles with a large coverage for high acceptance [12]. The hexagonal face of CLAS is conveniently divided into 6 azimuthal (with respect to the beam axis) triangular sectors as can be in **Fig. 2.2b**. The relevant parts that make up the existing CLAS are shown presented in teh following subsections.

2.2.1 Superconducting Torus Magnet

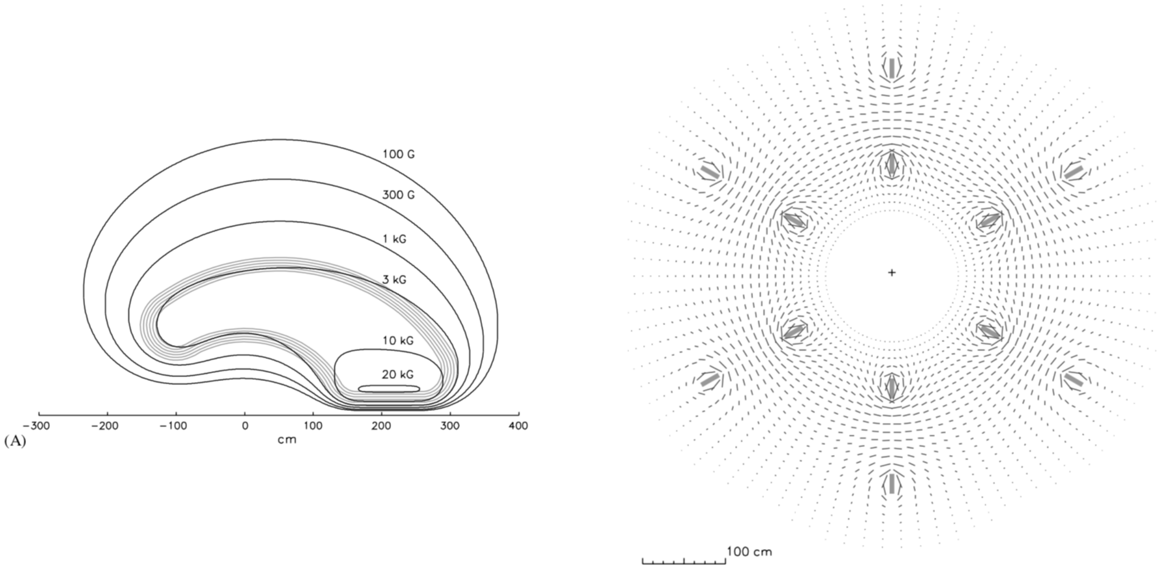

(**a**) Magnetic field map profile view

(**b**) Magnetic field map face view

Figure 2.3: Torus magnet's field maps [12]

To accurately measure the momentum of charged particles, a strong magnetic field is needed to bend the trajectories of the fast moving charged particles so that a radius of curvature can be extracted. A quick Lorentz force calculation determines the particles momentum, p:

$$p = qBr \tag{2.1}$$

where q is the particle's charge, determined by whether the particle bends away or toward the beam-line, B is the applied magnetic field, and r is the radius of curvature.

2.2.2 Drift Chambers (DC)

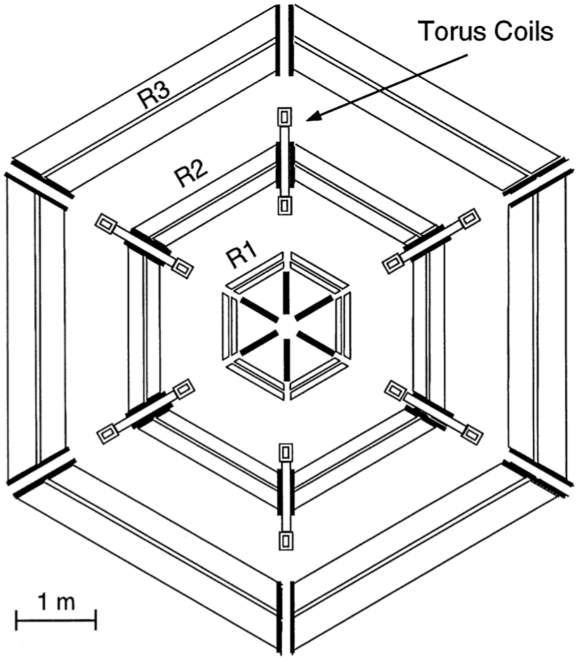

Figure 2.4: The torus embedded inside the DC, extending from the 2nd DC region to 3rd [13].

In order to take full advantage of the bending fields produced by the torus magnet, the drift chambers allows for track reconstruction. The DC, with angular coverage of 8° to 154°, is comprised of three regions, in succession of radial distance from the target, filled with a 90% argon-10% CO_2ionizing gas mixture and interwoven with sense wires hexagonally surrounded by field wires [13]. As particles traverse the gas mixture, the particle ionizes the gas along its path, and the ionized electrons are accelerated from the nearby field wires to their neighboring sense wires. A series of registered sense wire hits are strung together with drift times and distance of closest approach (DOCA) to determine the path of the particle (see **Fig.** 2.5).

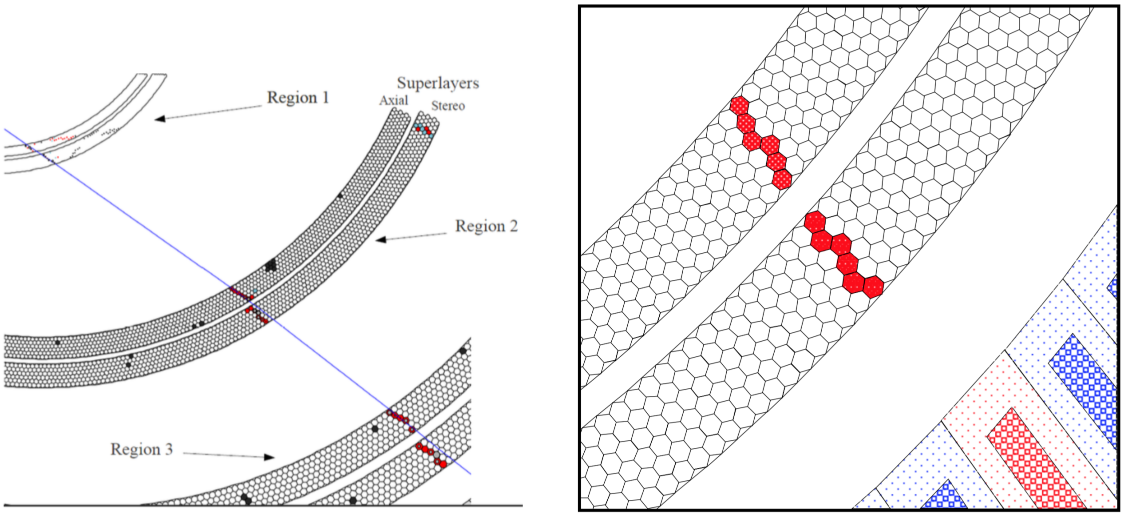

(a) Simulated track of particle traversing drift region (in blue), triggering sense wires cells (in red)

(b) Simulated track traversing drift region zoomed with red hexagonal cells belonging to the sense wires hit

Figure 2.5: DC track [12, 14, 15]

The negatively (positively) charged particle is bent toward (away from) the beam axis, under the influence of the toroid magnet's magnetic field. The bent track is fitted and the radius of curvature can be measured to determine the charge particle's momentum via **Eq. 2.1**.

Overall, the DC achieves resolutions:

Table 2.1: DC Resolutions

Variable	Value(s)	Units
$\delta p/p$ (@1 GeV/c)	1.5	%
$\delta\theta$	1	mrad
$\delta\phi$	4	mrad

2.2.3 Time of Flight Scintillation Counters (SC)

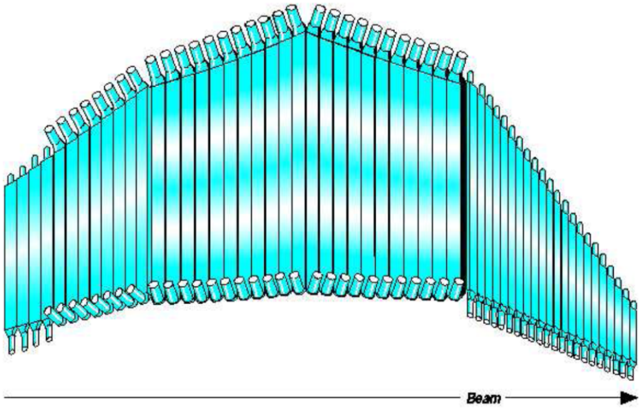

Figure 2.6: Profile view of a sector of the SC: Pictured are the 57 scintillator strips and PMTs on each end of the strips. [4]

The SC provides timing information with the scattered electron as the trigger, using its time as the reference time. Paired together with the known distances between detectors, absent of magnetic field, a particle's velocity can be determined. Tying this timing information together with the momentum from the DC, the mass can be inferred.

The SC is equipped with 57 Bicron BC-408 scintillator strips with a magnetically shielded photomultiplier tube (PMT) on each end of the strip. The configuration in **Fig. 2.6** allows for timing resolutions between 120 and 250 ps depending on the kinematics, which is well below the needed timing resolution of 300 ps to mass-separate out pions, kaons, and protons with momenta up to 2.5 GeV/*c* [4].

Table 2.2: SC Resolutions [4]

Variable	**Values**	**Units**
δt	$\in [120, 250]$	ps

2.2.4 Electromagnetic Calorimeter (EC)

The electromagnetic calorimeter is a sampling calorimeter with alternating layers of lead-scintillating material (see **Fig.** 2.7), with a lead:scintillator thickness ratio of 0.2. The EC measures energy deposited by particles with a polar angle coverage of 8° to 45° [16]. A particle impinges the EC and produces a shower that deposits its energy into both the insensitive lead and sensitive scintillating material. The EC is designed so that about a third of the energy is deposited into the scintillating material[1].

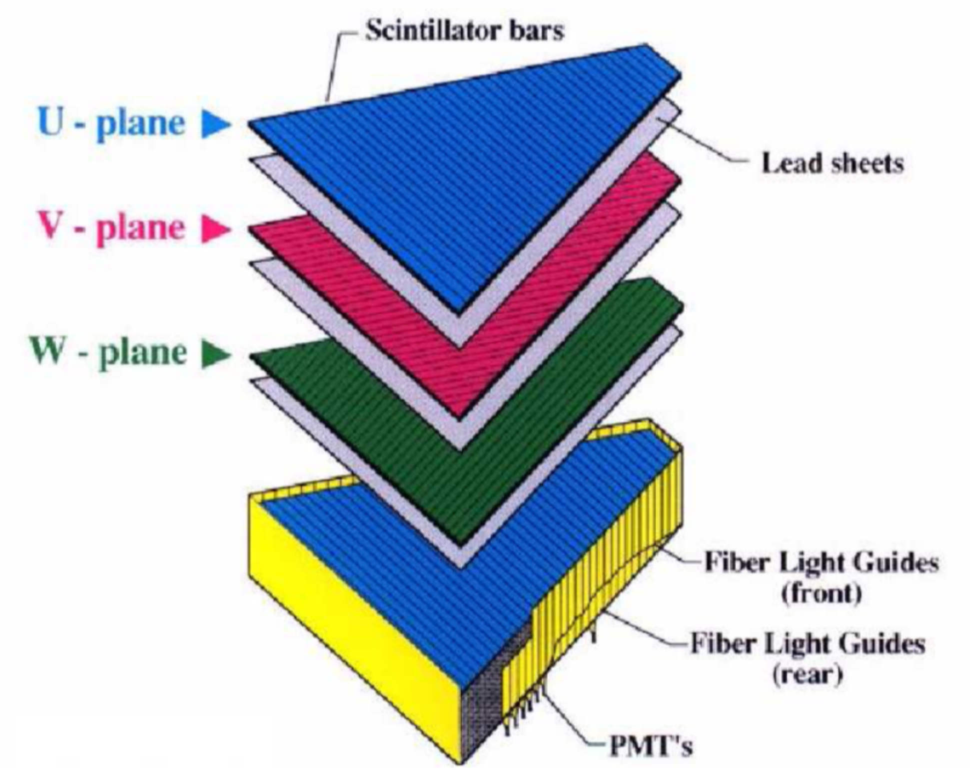

Figure 2.7: The layers of the EC [4]

---

[1] Calibration to this fraction are discussed in **Appendix** A.3.1.

Additionally, the layers are arranged so that the scintillating bars of each successive layer are parallel to each of the three sides of the sector's equilateral triangle (see **Fig.** 2.7). This coordinate system, with positions u, v, and w, allows for reconstruction of the particle's position, as can be seen in **Fig.** 2.8. Ultimately, since photon trajectories are not affected by magnetic fields, the photon's momentum vector can be inferred.

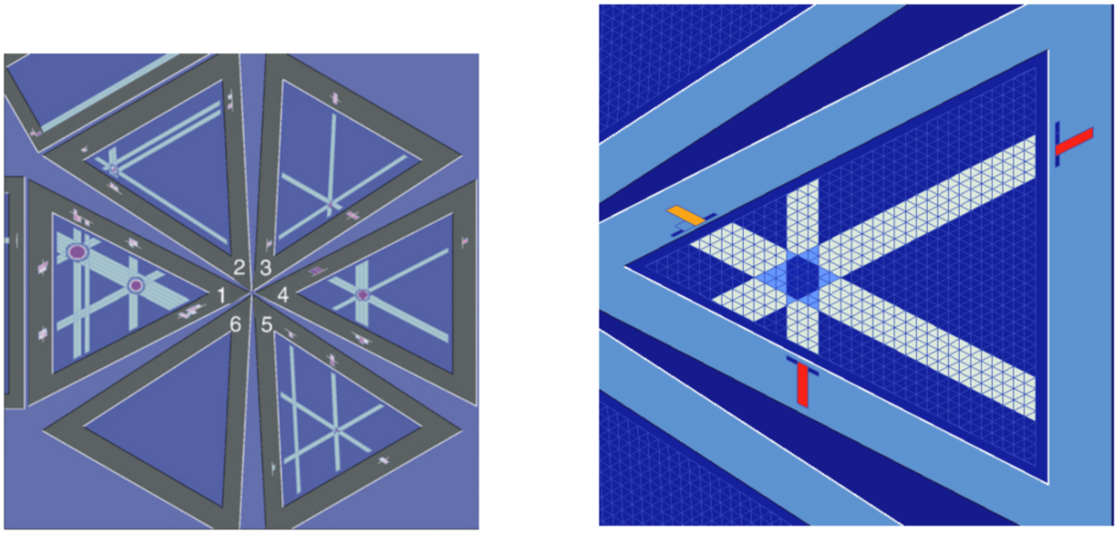

(a) Hits in the EC: The strips that are hit are highlighted in light blue, showing that the position of the initial hit in the EC in red.

(b) Sector view of EC hit where position is determined from successive hits of the alternating layers scintillation strips

Figure 2.8: EC hits [12,14]

The EC is able to achieve position, timing, and energy resolutions listed in **Table** 2.3. These resolutions together give a percent mass resolution below the 15% needed to distinguish π^0 and η in two-photon decays.

Table 2.3: EC Resolutions [4]

Variable	Value(s)	Units
$\delta E/E$ (@1GeV)	< 10	%
δx	2	cm
δt	1	ns
$\delta m/m$	< 15	%

3. EG6 Defining Features and Upgrades

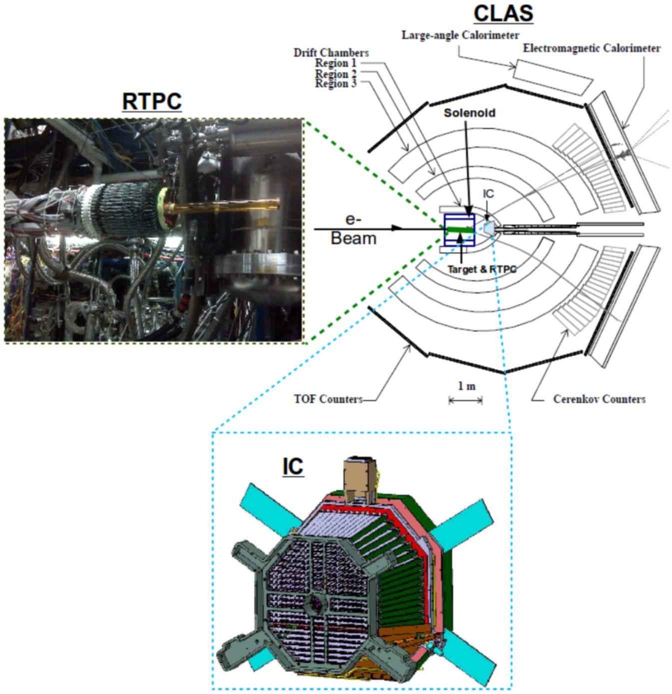

Figure 3.1: The defining upgrades to the CLAS EG6 experiment [4]

In order to make a fully exclusive DVCS or DVMP measurement in the coherent channel, the topic of this study, a few features beyond the orginal CLAS is required. In the following subsections, these will be discussed.

3.1 Target

The CLAS EG6 target, very similar to the previous CLAS EG4 experiment, BoNuS, is a fixed ^{4}He gas target held at 6 atm. The cylindrical target, 6 mm in diamter and 200 mm in length, is enclosed by an insulating 27 μm thick Kapton film cylinder with end-cap windows of 15 μm thick aluminum [1].

3.2 Inner Calorimeter (IC)

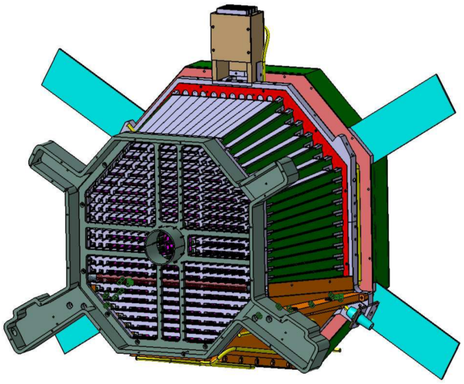

Figure 3.2: The IC represented in GEANT [14]

Resolution	Values	Units
$\delta E/E$	$\in [3,4]$	%
$\delta\theta$	$\in [3,5]$	mrad
$\delta\phi$	$\in [3,5]$	mrad

Table 3.1: IC resolutions [4] (for $E \in [2,5]$ GeV)

The IC, a part of a 2005 upgrade for the CLAS-E1DVCS experiment [17], shown in **Fig. 3.2**, allows for the measurement of the low-polar-angle photons that would otherwise never make it to CLAS: the EC is only sensitive to photons with polar angle between 8° and 45°. The need of coverage below 8° required by the kinematics of DVCS was addressed by the installation of the IC covers polar angles between 5° and 15°. Unlike the EC, the IC is outfitted with a projective array of 424 lead-tungstate ($PbWO_4$) crystals (see **Fig. 3.4**). This construction allows for resolutions in **Table 3.1**.

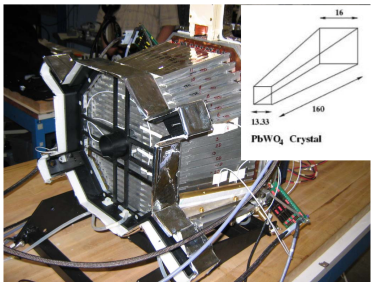

Figure 3.3: The IC with dimensions in mm [1]

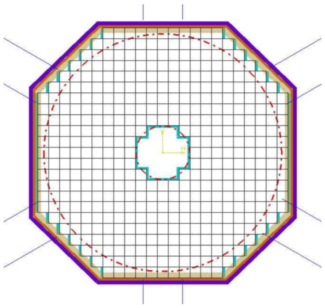

Figure 3.4: Schematic of crystal array for IC [14]

3.3 Solenoid Magnet

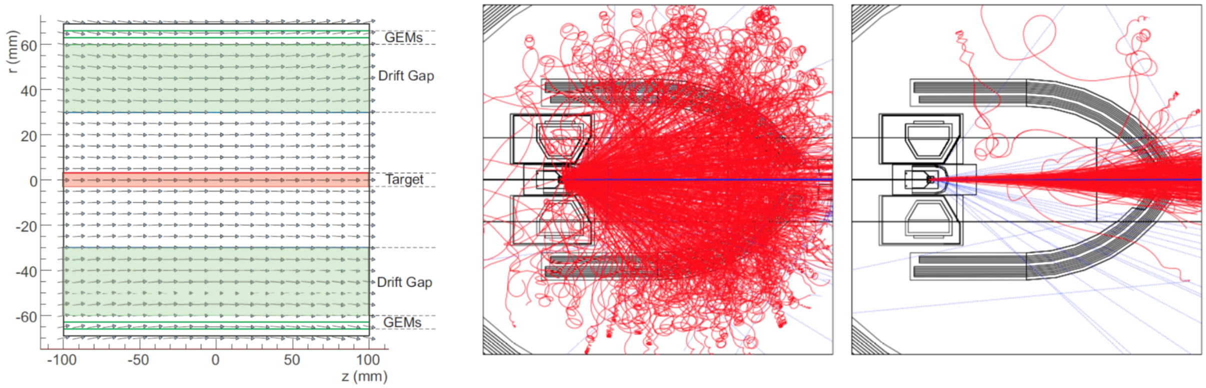

(**a**) Profile view of the magnetic field map in the RTPC produced by the solenoid [4].

(**b**) Affect of solenoid $\vec{B}$-field: GEANT simulation of the Møller electrons, in red, with (right) and without (left) the solenoid field [4].

Figure 3.5: Solenoid magnet field map (**a**) and effect on electrons in simulation (**b**).

The use of the solenoid magnet, which produces a 4.5 T, essentially uniform, magnetic field parallel to the beam-line around the target, is two-fold. The solenoid magnet sends the low-lying, low-energy Møller electrons, produced at the target, spiraling down the beam-line, heavily reducing the contamination the electrons of interest, as displayed in **Fig. 3.5b** from simulation. Secondly, the solenoid magnet produces a magnetic field, shown in **Fig. 3.5a**, that bends the path of the recoiled nuclei in the target to allow determination of its radius of curvature and, ultimately, its momentum.

The beam, solenoid, and torus configurations are listed in **Table 3.2**.

Table 3.2: EG6 Run Configurations [4]

Beam Energy [GeV]	Beam Current [nA]	Torus Current [A]	Solenoid Current [A]
1.204	150	2100	450
1.269	100	1900	450
5.700	100	1900	450
6.064	120-150	2100	450

3.4 Radial Time Projection Chamber (RTPC)

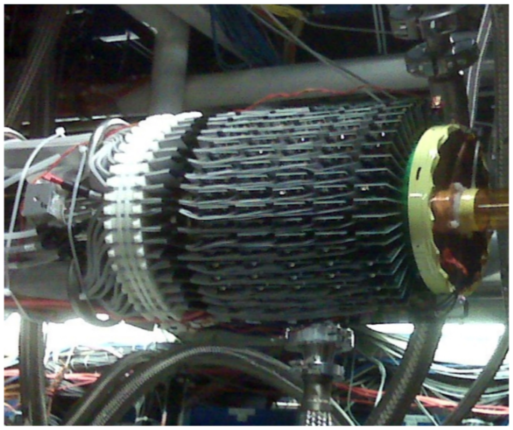

Figure 3.6: The physical RTPC where the beam would be coming from the left [4].

Coupled with the solenoid, the RTPC measures the recoiling ^{4}He that would never make its way to CLAS. Coherent DVCS and DVMP processes, where the target helium stays intact, has the recoiling helium with an average momentum per charge of about 100 MeV/c [18]. The existing CLAS system, however has a momentum per charge threshold of 250 MeV/c [4].

The cylindrical RTPC, shown in **Fig.** 3.7, surrounds the 6 atm ^{4}He gas target with three gaps, in increasing radial distance:

1. A 1 atm ^{4}He gas region to reduce secondary interaction of the recoiled helium with Møller electrons
2. A region filled with the drift gas
3. The drift region which is also filled with the drift gas but starts with a cathode foil that accelerates the drift electrons to the anode, the three subsequent gas electron multiplier (GEM) layers, pictured in **Fig.** 3.8, and to the 3200 readout pads. The

GEM layers amplify the signal of the few drift electrons with a 400 V potential difference at each layer and a 150 V potential difference between each subsequent layer, giving an overall gain on the order of 10^6.

The drift region of the RTPC is comprised of a mixture of 80% neon, and 20% dimethyl ether (C_2H_6O). This gas mixture is chosen for its characteristics of low diffusivity and small Lorentz angles, the angle between the applied magnetic field's and electric field's forces on the drift electron. Effectively, these characteristics minimize the changes in drift speed of the ionized electrons used to determine the track of the helium in the RTPC.

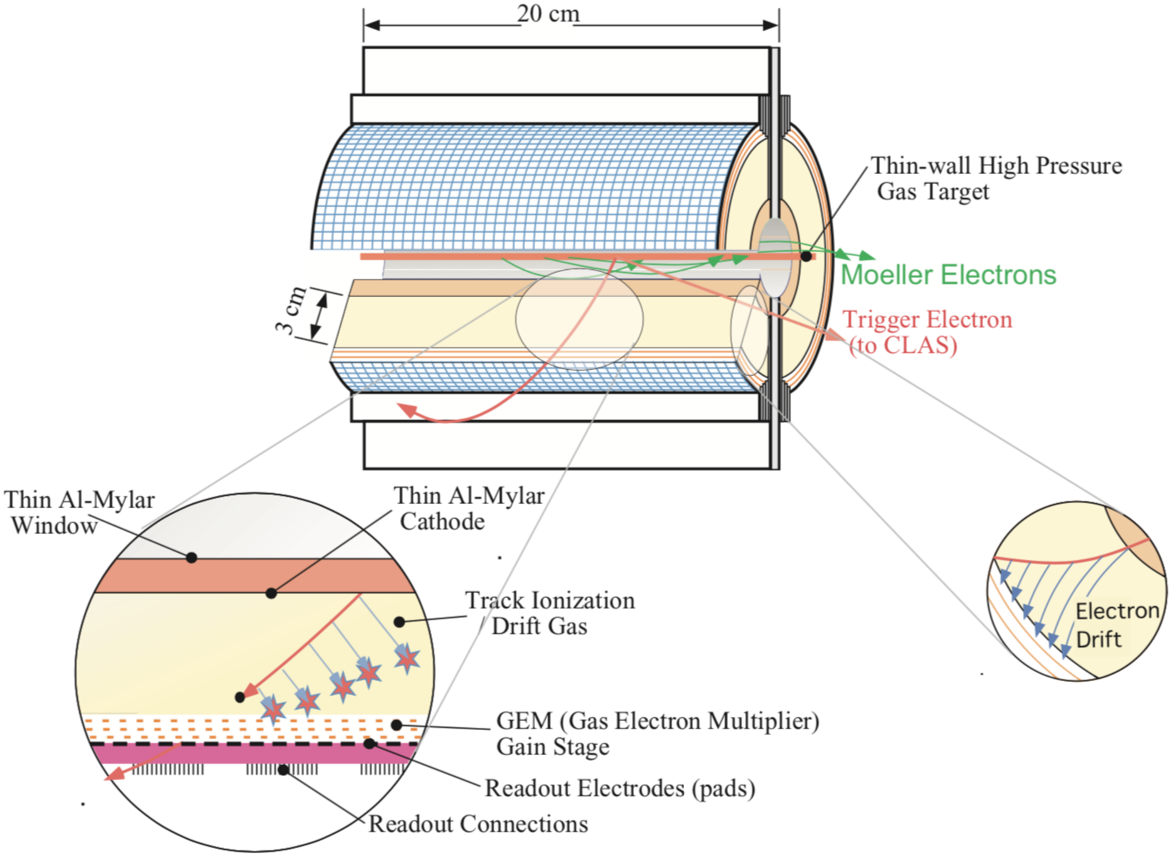

Figure 3.7: The RTPC schematic [1]

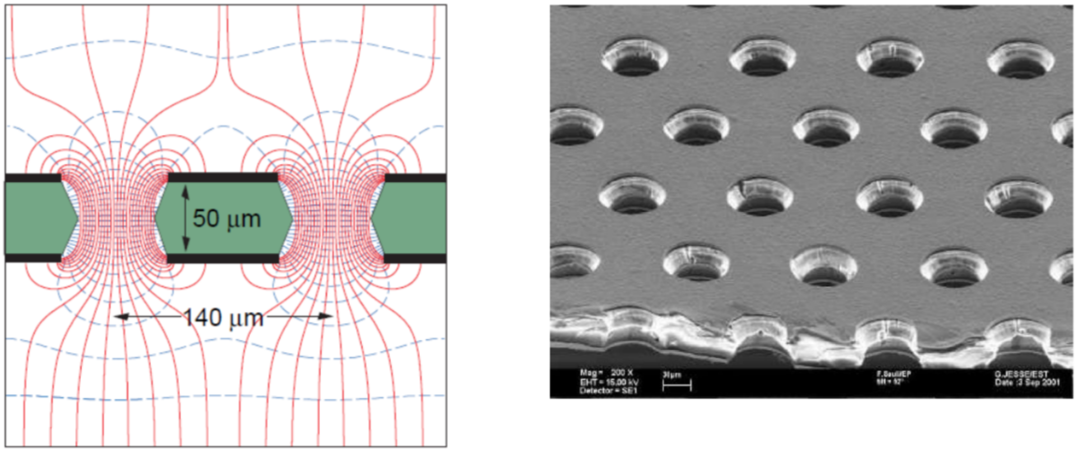

(a) Schematic of a GEM layer used at the anode of the RTPC **(b)** Scanning Electron Microscope of a GEM layer

Figure 3.8: GEM layers [15]

As the helium traverses the RTPC drift region, it ionizes the drift gas and the ionized electrons are curled by the solenoid's magnetic field and accelerated toward the anode, by its potential difference with the cathode, as seen in the schematic **Fig. 3.9b**. The drift electrons cascade through each successive layer of the GEM and creates an avalanche

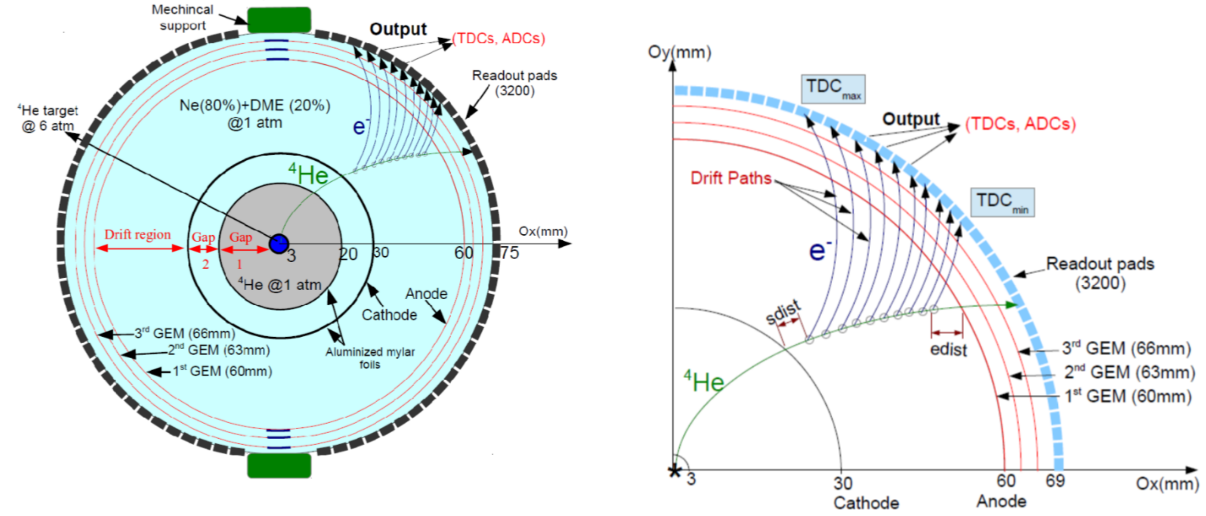

(a) Schematic of ^{4}He track, in green, with ionized electrons, in dark blue, in RTPC **(b)** Zoomed quadrant of RTPC with GEM layers and readout pads shown

Figure 3.9: RTPC track [15]

of secondary electrons that produce a sizable signal. Coupled with the position of the readout pad and the timing information from the TDCs, the point of ionization can be determined. A track fitting algorithm can then be used to string these points together to determine the track of the recoiled ^{4}He. With a good understanding of the energy loss along the path, the final state momentum of the ionizing particle can be determined by its track's radius of curvature using a modified version of **Eq. 2.1**.

- -

With the CLAS upgrades of the IC and the RTPC, with the help of the solenoid magnet, the full exclusivity required in studying DVπ^0P, among other processes, can be realized.

III. Particle Identification (PID)

$$e\,^4\text{He} \to e'\,^4\text{He}'\pi^0 \to e'\,^4\text{He}'\gamma\gamma$$

To study coherent DVCS or DVMP with a ^{4}He target, the particles that need to be identified are the scattered electron with CLAS, the recoiled helium with the RTPC, and the photon(s) produced with the IC and EC. This analysis' particle identification follows exactly the procedure outlined in [1] so that a fair comparison can be made between the quality of the two event selection methods.

\- -

The starting-point files, broken up into `2 GB` chunks, are accessible on the JLab scientific computing cluster, `ifarm` and can be found on the mass storage system, tape library:

`/mss/clas/eg6/production/pass2/6gev/HROOT/`

The files have the form:

`hroot_`N_{run}`_`N_{file}`_pass2.root`

where N_{run} is the run number ($\in \{61510, \ldots, 61930\}$) and N_{file} is the two to three digit file number, starting from `00`.

The following histograms will be from just the `61510` run since they capture the signficance of each cut.

For clarity, some efforts are made to highlight the important aspects of each cut:

- In the following 1D histograms,
    - The light-blue filled histograms are the distributions that pass every other particle identifcation cut except its own.
    - The unfilled distributions have no cuts applied.
    - Dotted lines (··········) and dashed lines (----) are used to indicate the low end and high end of the cut, respectively. That is, all values greater than the low end and all values to lower than the high end are accepted.
- For 2D histograms, distributions that are of interest are colored and rejected distributions are in grayscale.
- Finally, psuedocode is provided to help clarify what was explicitly done.

4. Electron Identification (eID)

$$e\,^4\text{He} \rightarrow e'\,^4\text{He}'\gamma\gamma$$

Identification of the scattered electron identification is done by a series a tests and cuts. Particles passing all of these tests are accepted as electrons and will be subjected to event selection after. No other particle identifcation is done if the particle fails any of the tests or cuts. For the following procedure, the iteration variable `ipart` will loop over the `EVNT` bank from 0 to `gpart`.

4.1 Pre-Cuts

Particles failing any one of these pre-cuts are skipped over entirely. These are the minimal requirements to identifying the electron.

4.1.1 Status Cut

The status, stored in the array `stat` of the `EVNT` bank, tells whether the particle passed both hit-based tracking (HBT) and time-based tracking (TBT) for DC track reconstruction. In particular, if

$$\texttt{stat[ipart] > 0}\ , \tag{4.1}$$

the particle passes both HBT and TBT tracking. The distributions can be seen in **Fig. 4.1**.

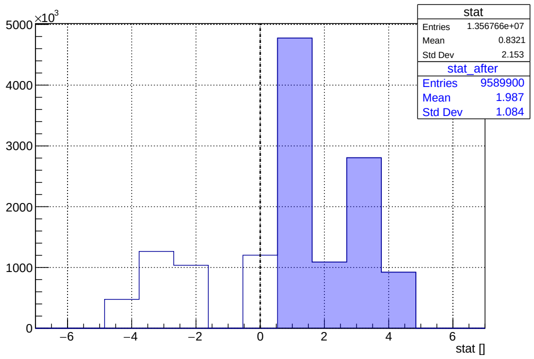

Figure 4.1: Status Cut: Only Good (positive) are accepted.

4.1.2 Charge Cut

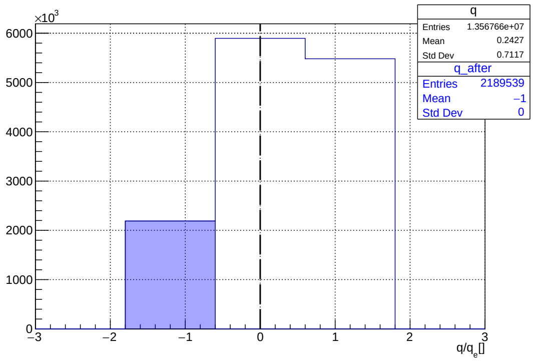

Figure 4.2: Charge Cut: Only negative tracks pass this cut.

The status cut tells us that the DC track reconstruction is good so we can tell whether the partcle traversing the DC is negatively charge, positively charge, or neutral by how it bends under the influence of the torus' magnetic field. Since we are looking for electrons, we want

$$\texttt{q[ipart] == -1} \; , \tag{4.1}$$

where the `q` array holds whether the particle is positively(`+1`)/negatively(`-1`) charged or neutral(`0`), as seen in **Fig.** 4.2.

4.1.3 Sector Matching

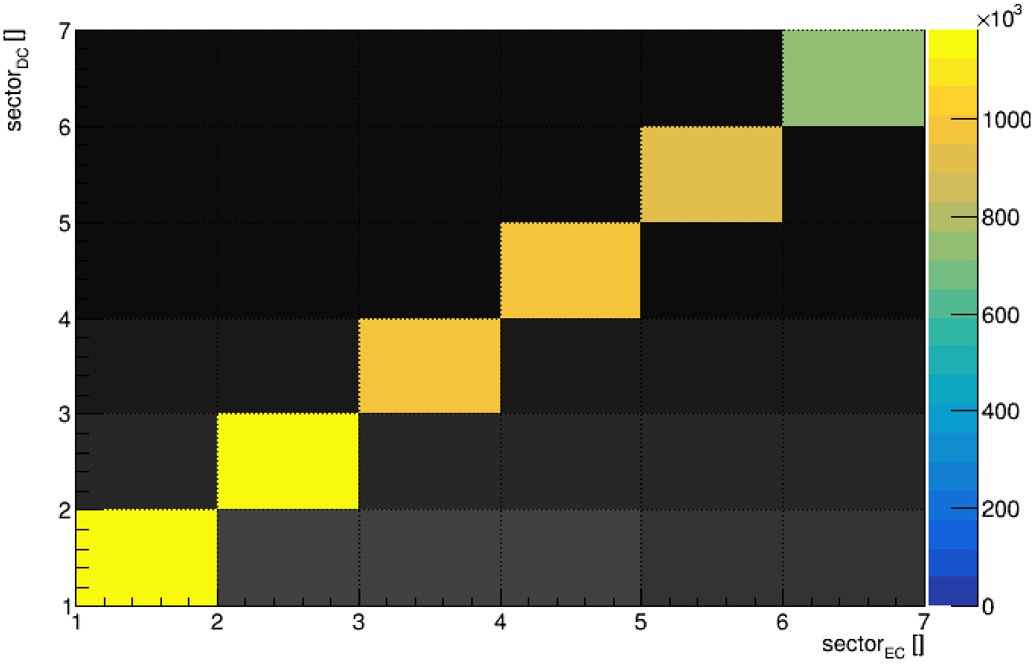

Figure 4.3: DC sector vs. EC sector: Only matching sectors will pass this cut.

To minimize accidentals and sector edge effects, the sectors of the different detectors are matched:

$$\begin{aligned} &\texttt{dc\_sect[dc[ipart]-1] == ec\_sect[ec[ipart]-1]} \\ &\texttt{sc\_sect[sc[ipart]-1] == cc\_sect[cc[ipart]-1]}\ , \\ &\texttt{dc\_sect[dc[ipart]-1] == sc\_sect[sc[ipart]-1]} \end{aligned} \tag{4.1}$$

where `dc_sect`, `ec_sect`, `sc_sect`, and `cc_sect` are fortran arrays in the `DCPB`, `ECPB`, `SCPB`, and `CCPB` banks, respectively. The `dc`, `ec`, `sc`, and `cc` are arrays in the `EVNT` that translate the banks used for the DC, EC, SC, and the Cherenkov counters (CC) subdetectors into the `EVNT` bank. As can be seen in **Fig. 4.3**, only equal sectors, along the diagonal, pass this cut.

4.2 Vertex Cut

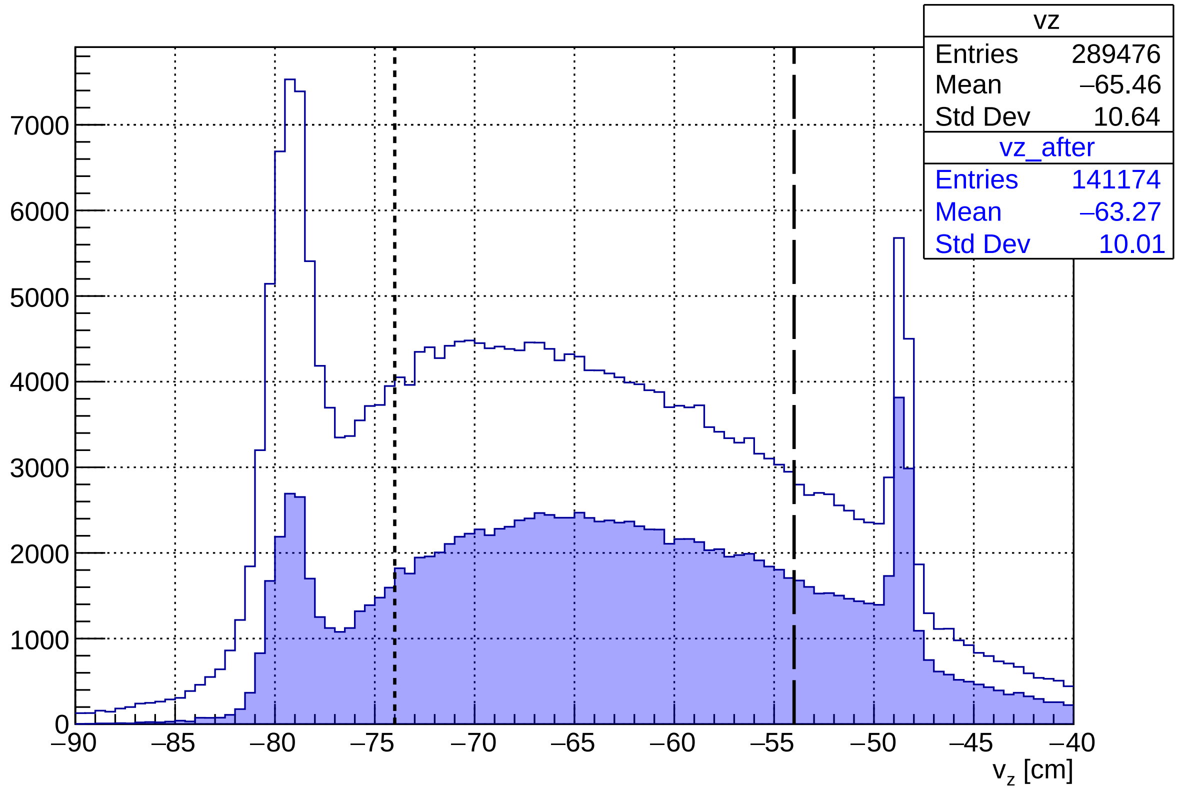

Figure 4.4: Vertex Cut: Only particles coming from well inside the target walls are accepted.

An electron vertex cut is made to ensure that the detected scattered electron interacted with the target. The center of the target is placed upstream from the nominal center of CLAS at -64 cm. Thus, the walls of the target should be around -80 and -50 cm. Cuts are placed well within the target walls, with the length of the RTPC, to ensure the source of the interaction is well understood.

(4.1) `-74 < vz[ipart] && vz[ipart] < -54 ,`

where `vz` is the array storing the z-component of the vertex in the `EVNT` bank in cm.

4.3 Solenoid Fiducial Cut

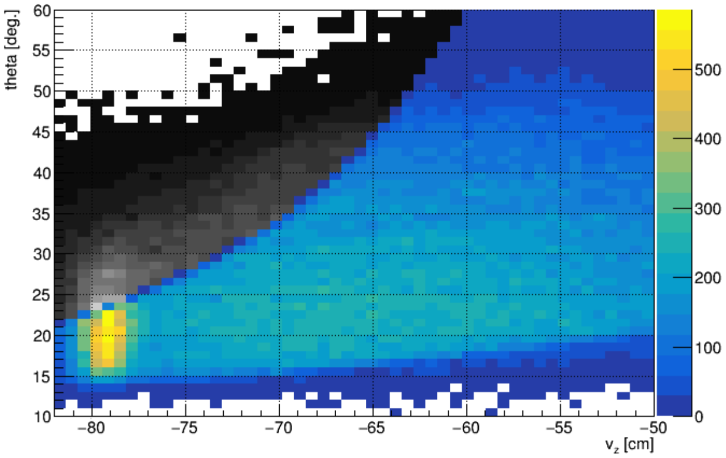

Figure 4.5: Solenoid Fiducial Cut: Particles that have hit the solenoid are rejected.

Although the solenoid is crucial in this experiment for reducing background Møller electrons and for measuring the momenum of the recoiling helium, scattered electrons with large polar angle will interact with the physical solenoid, making momentum reconstruction of these particles lousy.

Therefore, a polar angle cut depending on the electron vertex is introduced to eliminate these particles:

$$\texttt{cz[ipart] > cos(theta\_sol)}, \tag{4.1}$$

with

$$\texttt{theta\_sol = atan2(11, z\_sol - vz\_corr)},$$

$$\texttt{z\_sol = -64 + 20.96/2}\ ,$$

where `vz_corr` is the z-component of the corrected particle's vertex, `z_sol` is the center of the solenoid with respect to CLAS, both in cm, and `cz` is the array with values of the z-direction or z-component of the particle's momentum.

4.4 DC Momentum Cut

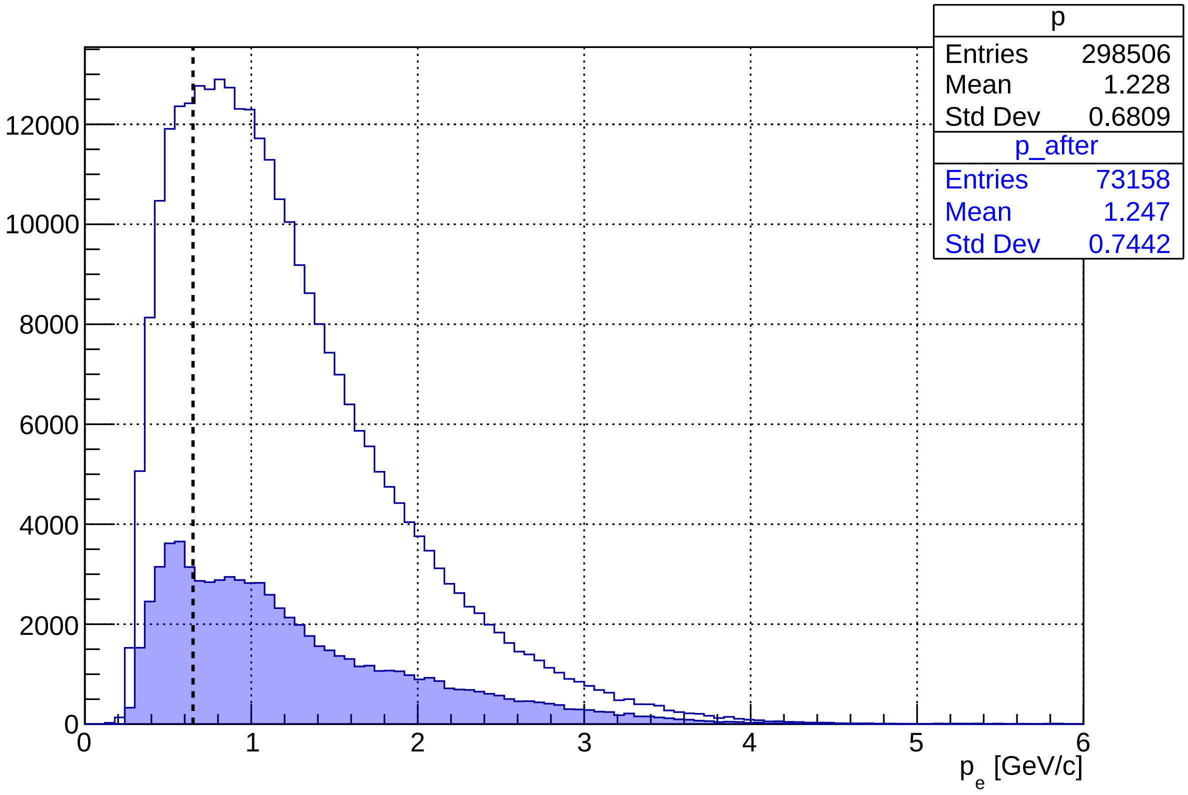

Figure 4.6: Momentum cut: To protect against Møller electrons and π^- a cut on the momenum is applied.

To minimize radiative effects from low energy electrons and to separate from other negatively charged particles, namely π^-, a cut on the particle's momentum is at least 650 MeV:

(4.1) `p[ipart] > 0.65 ,`

with `p` being the array in the `EVNT` that holds the momentum of the particle in GeV.

4.5 DC Fiducial Cut: IC-Shadow

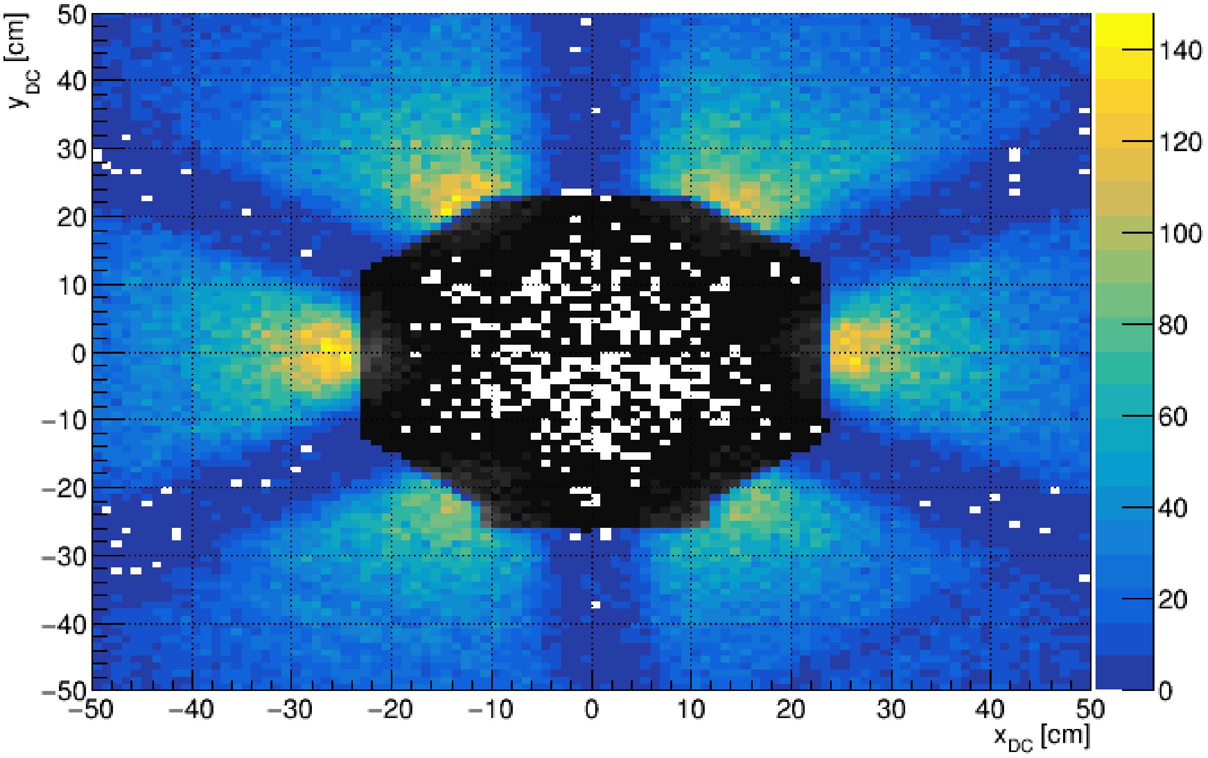

Figure 4.7: DC Fid. Cut: Tracks directly coming from the IC have energy loss that is unaccounted for.

Particles from the target, on their way to CLAS, that hit the IC lose energy so both track and energy reconstruction become imperfect. To avoid this altogether, a fiducial cut is placed to rule out these poorly reconstructed particles:

(4.1) `!(geo->IsInside(x,y))` ,

where `geo` is a shape defined by successive connection of the points in **Table 4.1** and the exclamation mark (`!`) indicates logical negation.

Table 4.1: Boundary of IC Shadow Fiducial Cut

Index *i*	x_i **[cm]**	y_i **[cm]**
1	-11.15	-26.07
2	-11.15	-23.10
3	-23.10	-12.85
4	-23.10	11.50
5	-10.30	22.95
6	9.91	22.95
7	23.73	13.10
8	23.73	-12.40
9	12.30	-22.36
10	12.30	-26.07
11	-11.15	-26.07

x and y are the x- and y- components of $\vec{x}_{\text{IC}}$, which are back-projections of the DC hit to the IC:

$$\vec{x}_{\text{IC}} = \left(\frac{16}{z_{\text{DC}}}\right)\vec{x}_{\text{DC}}$$

with

$$\vec{x}_{\text{DC}} = \begin{bmatrix} \texttt{tl1\_x[dc[ipart]-1]} \\ \texttt{tl1\_y[dc[ipart]-1]} \\ \texttt{tl1\_z[dc[ipart]-1]} \end{bmatrix}$$

being the DC track position, where `tl1_x`, `tl1_y`, and `tl1_z` are arrays in the `DCPB` bank that have the DC's track x-, y-, and z-positions in the first layer, respectively, all in cm.

As seen in **Fig.** 4.7, DC hits that are constructed on the interior of this geometry are rejected (grayscale), and hits on the exterior are accepted (colored).

4.6 EC Energy Cut

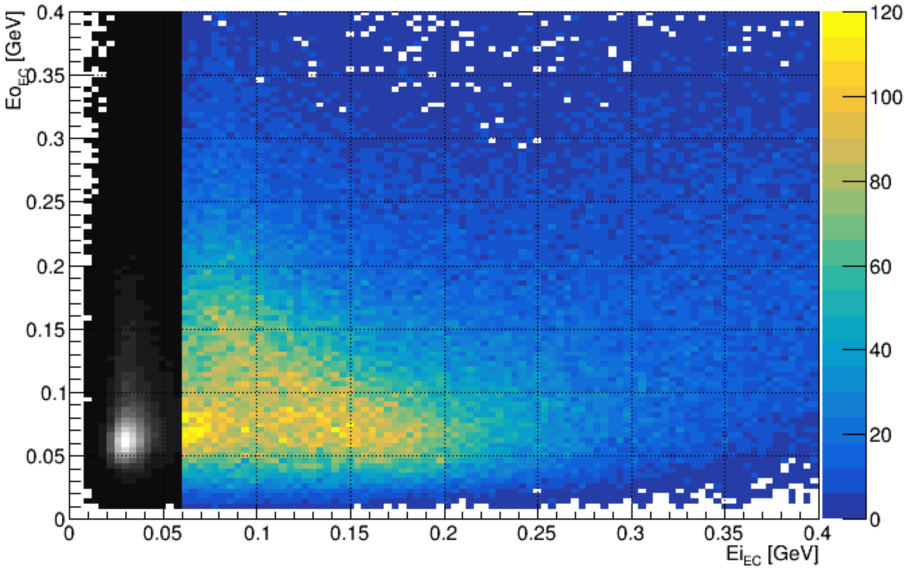

Figure 4.8: EC Energy Cut: The minimum ionizing π^- imprint can be seen in grayscale are rejected.

Even with the DC momentum cut, there are still π^- that can contaminate the electron sample. This is dealt with by using an EC energy cut. Pions are minimum ionizing particles that lose its energy mostly through ionzination [19]. The EC layers is divided into two parts: an inner part made of thick 5 super-layers and a remaining outer part with 8 super-layers of the 3 cm lead-scintillating material. The pion's energy loss is propotional to the length of EC super-layers it traverses through at 2 MeV/cm, totalling to 60 Mev by the time it passes through the inner part of the EC.

A cut is made at 60 MeV to reject π^-:

(4.1) `ec_in[ec[ipart]-1] > 0.06 ,`

where `ec_in` is the array storing the energy deposited in the inner part of the EC, in GeV, in the `ECPB` bank. The effect can be seen in **Fig.** 4.8, where the π^- distribution can be seen in white with $\mathtt{EI}_{EC} < 0.06$ GeV.

4.7 EC Sampling Fraction Cut

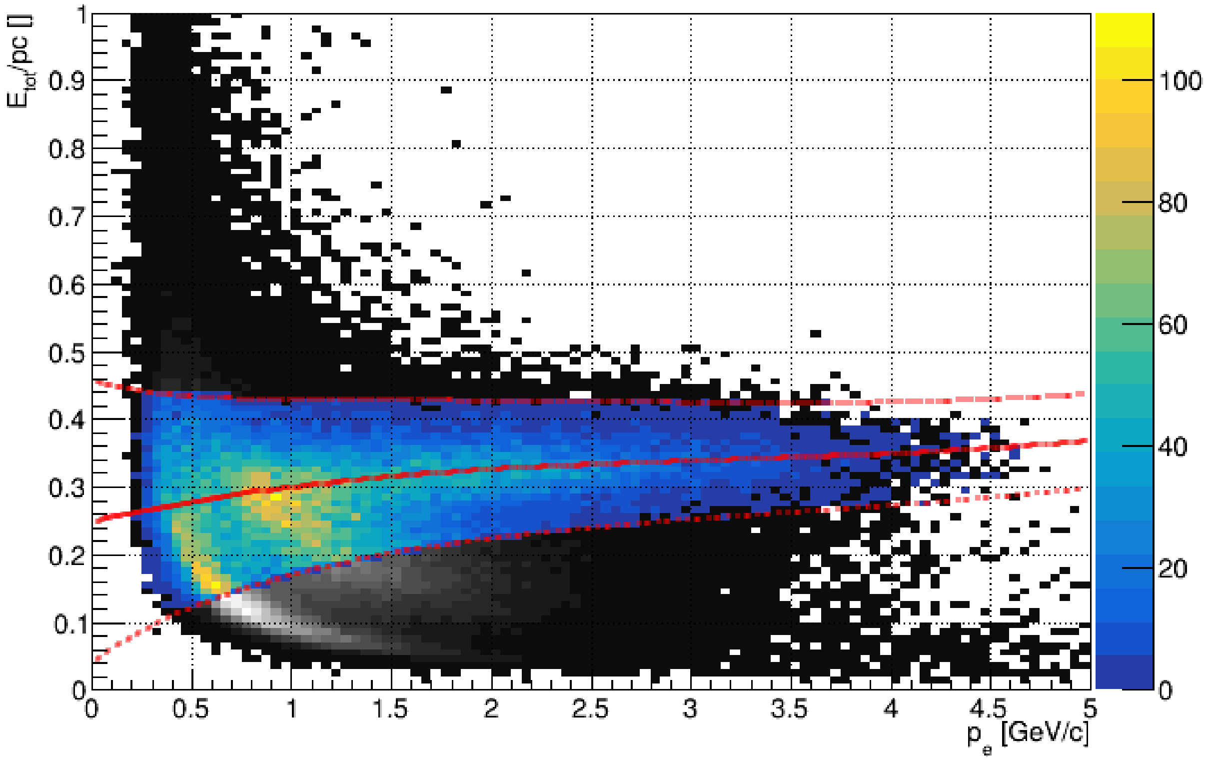

Figure 4.9: EC Sampling Fraction Cut: The distributions of the energy and sector dependent EC sampling fraction as a function of momentum are shown (for sector 1). The dependence is fitted and measurements 3.5 σ outside the fit are rejected (shown in red).

The electron's sampling fraction, `SF`, is ratio of the measured energy in the EC to the momentum in the DC. If all of the energy is measured in the EC, this ratio should be more or less unity. However, because the EC is a sampling calorimeter with, energy deposited in the lead layers cannot be measured. The EC was designed and optimized through simulation to have this sampling fraction ratio at about 0.3 but due to energy loss, radiative effects, and produced shower geometry, especially at low momentum, the quality of energy reconstruction is hindered. To address this, a cut on the sampling fraction is

Table 4.2: Sampling Fraction Parameters (transpose can be found in [1])

	Paramter					
Sector	a	b	c	d	e	f
1	0.2490	0.0676	-0.0182	0.00190	0.0469	0.6123
2	0.2636	0.0557	-0.0132	0.00120	0.0508	1.3342
3	0.2721	0.0563	-0.0127	0.00125	0.0518	1.5067
4	0.2727	0.0507	-0.0117	0.00110	0.0427	0.6838
5	0.2593	0.0476	-0.0100	0.00090	0.0469	0.4713
6	0.2517	0.0562	-0.0137	0.00130	0.0440	0.4299

made:

(4.1) `abs( SF - mu ) < 3.5 * sigma ,`

where `mu` and `sigma` are calculated from the electron's momentum:

$$\texttt{mu}(p) = a + bp + cp^2 + dp^3$$
$$\texttt{sigma}(p) = \frac{e}{\sqrt{f+p}}$$

with the parameters, $a, b, c, d, e,$ and f are sector dependent, tabulated in **Table** 4.2.

The measured sampling fraction, `SF`, is the energy from the EC, taken to be the maximum between the total energy measured and the sum of the energy deposited in the inner and outer parts of the EC, in the `ECPB` bank over the momenum from the `EVNT` bank:

```
SF = max( Ei + Eo, Etot )/p[ipart];

    Ei = ec_ei[ec[ipart]-1]
                                 .
    Eo = ec_eo[ec[ipart]-1]

  Etot =  etot[ec[ipart]-1]
```

`SF` outside the 3.5 `sigma` cut are thrown out and the resulting cut can be seen in **Fig.** 4.9.

4.8 EC Fiducial Cut

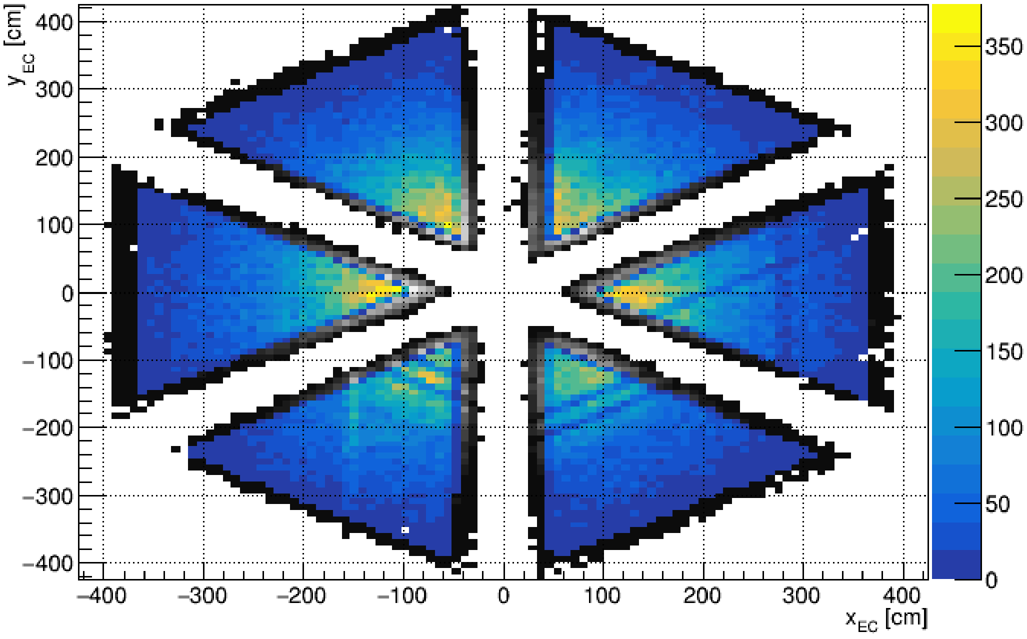

Figure 4.10: EC Fid Cut: x- and y-coordinates of the face of the EC that are rejected (grayscale) and accepted (colored).

To reject partial energy reconstruction from particles hitting the edge of the EC, a fiducial cut is introduced.

The triangular coordinate system in the EC, where the u-, v-, and w-axes are parallel to the scintillating strips of a layer is utilized to conveniently define the edges of each EC sector. The cuts that are placed are then:

$$\begin{array}{r} \texttt{60 < u \&\& u < 390} \\ \texttt{v < 360} \\ \texttt{w < 390} \end{array} \quad , \tag{4.1}$$

The EC coordinates u, v, and w are shown explicitly in **Appendix B.1** in terms of the EC's Cartesian coordinates x, y and z.

- -

If no electrons are identified for a given event, the event is skipped over since the identification of other particles rely on a good determination of the scattered electron. The electron takes the momentum:

$$P_e = (\vec{\boldsymbol{p}}_e, p_e)$$

where $p_e = \texttt{p[ipart]}$ and

$$\vec{\boldsymbol{p}}_e = p_e * \begin{bmatrix} \texttt{cx[ipart]} \\ \texttt{cy[ipart]} \\ \texttt{cz[ipart]} \end{bmatrix}$$

with `cx`, `cy`, and `cz` being arrays in the `EVNT` bank that house the x-, y-, and z- components of the unit direction vector.

- -

5. Photon Identification (γID)

$$e^4\text{He} \to e'^4\text{He}'\gamma\gamma$$

Both calorimeters, the EC and IC are capable of detecting photons. The difference in geometry alone require different cuts for photon identification. Ultimately, the difference in detector makeup require entirely independent methods for qualifying whether a photon is "good" or not.

5.1 EC Photon Identification (γ_{EC}ID)

The photons that make their way to the EC have larger polar angle and typically lower energies. To determine whether or not a photon has made it to the EC, the following cuts are applied. Note, since EC photons do not make it their way into the previous analysis [1], a slightly modified version of Hattawy's particle identification [4], which now includes other EC corrections (see **Appendix A.3**), is applied. Again, the index variable, `ipart`, loops over the `EVNT` bank from 0 to `gpart` and the `ec` array translate the indices of `EVNT` bank to the `ECPB` bank that holds the EC's information.

5.1.1 Charge Cut

We only want neutral particles, so a cut is made on the charge:

(5.1) `q[ipart] == 0 ,`

`q` again is the array in the `EVNT` bank that holds the charge of the particle. This cut is displaced in **Fig. 5.1**.

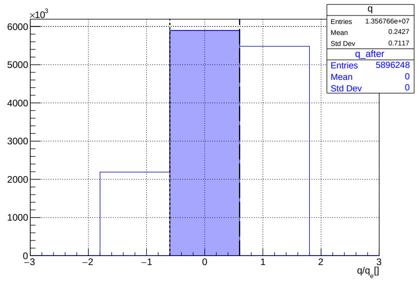

Figure 5.1: Charge Cut: Neutral particles are accepted.

5.1.2 β Cut

To reject other neutral particles, like the neutron, a cut to the normalized velocity, $\beta = v/c$, is applied to all neutral particles.

(5.1) `abs( b[ipart] - 1 ) < 0.07 ,`

`b` is the array in the `EVNT` bank that holds the measured β values. The resulting cut is shown in **Fig. 5.2**.

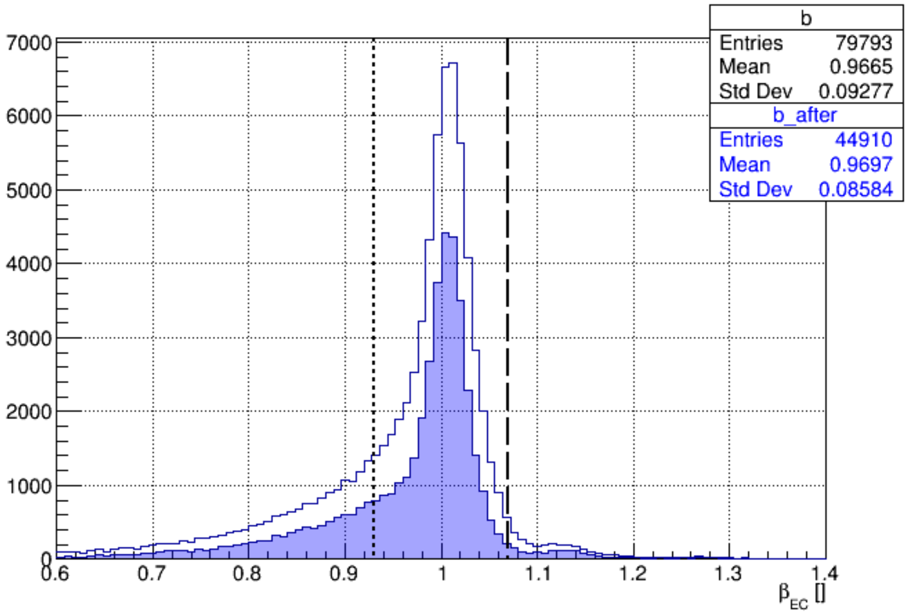

Figure 5.2: β Cut: To reject neutrons, a β cut is applied to accept the much faster photons.

5.1.3 Energy Cut

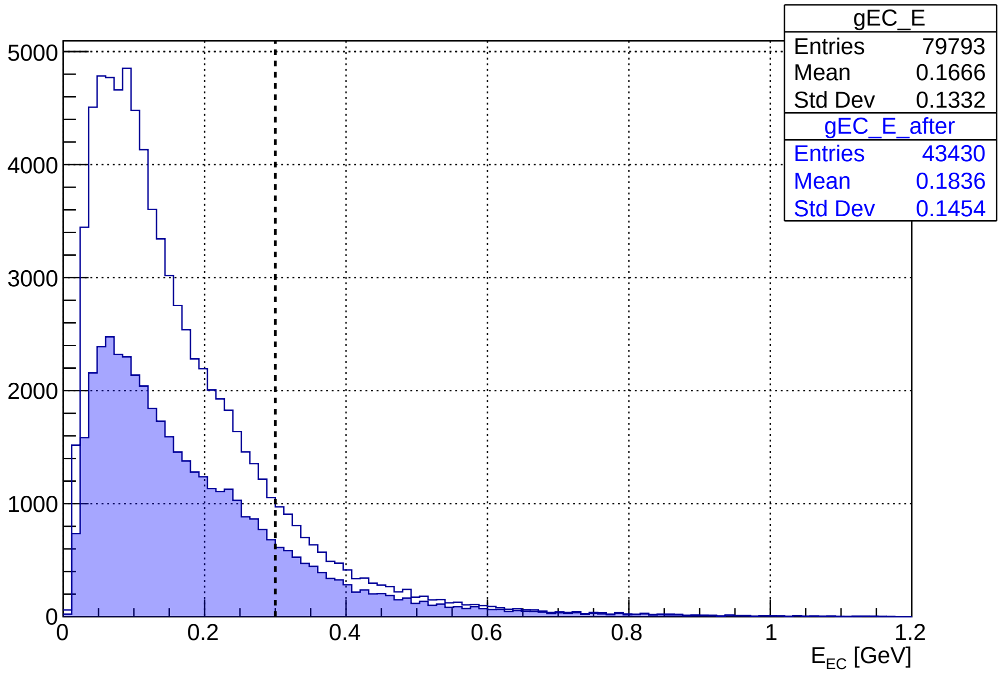

Figure 5.3: Energy Cut: Lower energy particles are poorly reconstructed. These particles are rejected.

Photon reconstruction becomes increasingly difficult at low energies, especially with a sampling calorimeter; the low energy photon can only make it through a few layers of the lead and scintillating material and the showers produced may be fully absorbed in the insensitive layer of lead, never making it to the next scintillating layer.

$$\texttt{E > 0.3 ,} \tag{5.1}$$

where `E` is the photon's total energy taken to be

$$\texttt{E = max(Etot, Ei + Eo)/ 0.273 ,}$$

with `Etot`, `Ei`, and `Eo` are defined previously in **Section 4.7** and 0.273 is the nominal sampling fraction, the optimized and designed value of the ratio of the energy deposited to the total energy in the EC. The accepted and rejected distributions are shown in **Fig. 5.3**.

5.1.4 EC Fiducial Cut

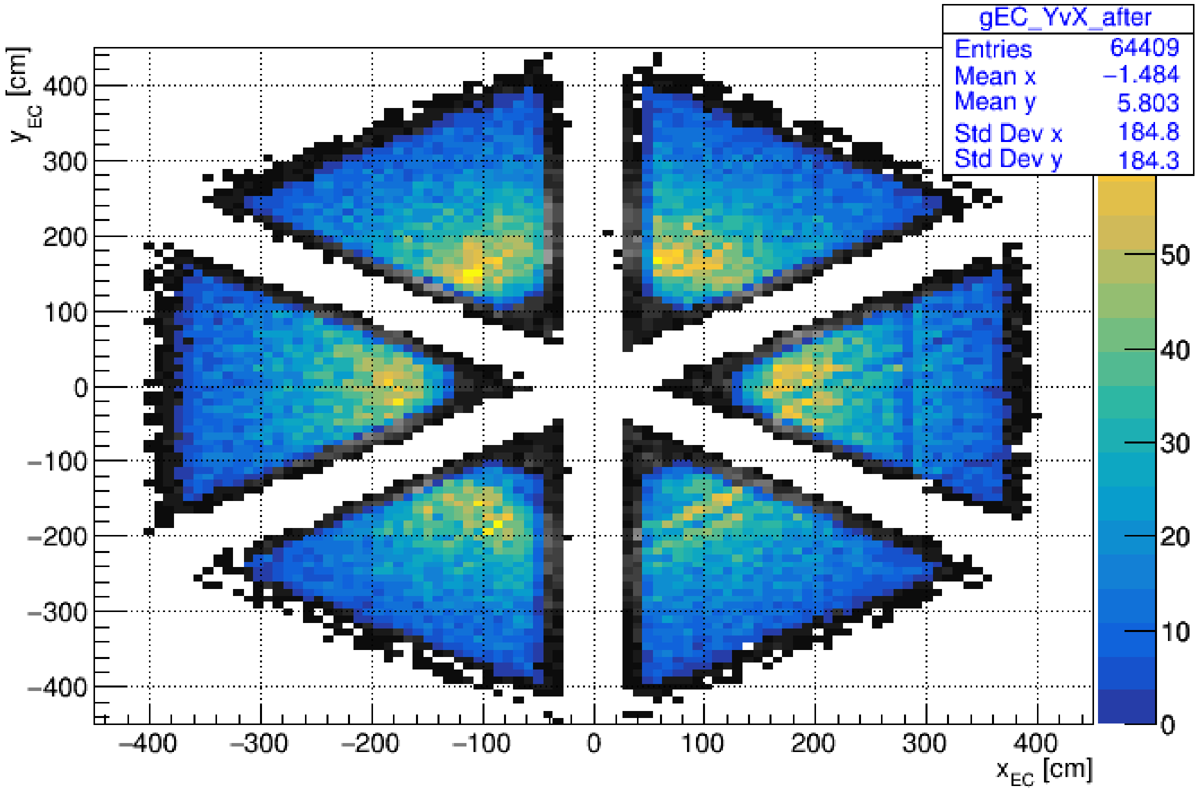

Figure 5.4: EC Fid. Cut: Reject particles hitting the edges of the EC.

To reject partial energy reconstruction from particles hitting the edge of the EC, the fiducial cut is used:

```
100 < u && u < 390
            v < 360
            w < 390
```
(5.1)

where u, v, and w are constructed in the same way as it is in **Section 4.8**.

\- -

Accepted EC photons take momentum

$$P_\gamma = (\vec{\boldsymbol{p}}_\gamma, E_\gamma)$$

where

$$\vec{\boldsymbol{p}}_\gamma = E_\gamma \begin{bmatrix} \texttt{cx[ipart]} \\ \texttt{cy[ipart]} \\ \texttt{cz[ipart]} \end{bmatrix}$$

with

$E_\gamma =$ `E * scaleFac( E );`

`E = max( Etot, Ei + Eo )/ sampFrac(runnb, evntid, sector)`

`sampFrac`, which depends on the run number (`runnb`), event number (`evntid`), and sector, is the time and sector dependent EC sampling fraction correction done by N. Baltzell [20], as discussed in **Appendix A.3.1**. `scaleFac`, which depends on the measured energy, `E`, is energy dependent EC scaling factor correction done in this study, as discussed in **Appendix A.3.2**.

\- -

5.2 IC Photon Identification (γ_{IC}ID)

The geometry and position of the IC dictate the kinematics of what photons can be identified; they are lower angle (between 8° and 15°), high energy photons. Again, the procedure to pick out good photons follows the previously done work [1]. The following procedure will have index `iic` to loop over the `ICPB` bank ranging from 0 to `icpart`.

5.2.1 Energy Cut

Similar to the EC, lower energy photons are difficult to reconstruct. In the IC, the shower produced by lower energy photons are shallower but broader, making both energy and position reconstruction poor. An energy cut is applied:

(5.1) `etc[iic] > 0.2 ,`

with `etc` being the array in the `ICPB` bank that has the energy in GeV. The distributions and cut can be seen in **Fig. 5.5a**.

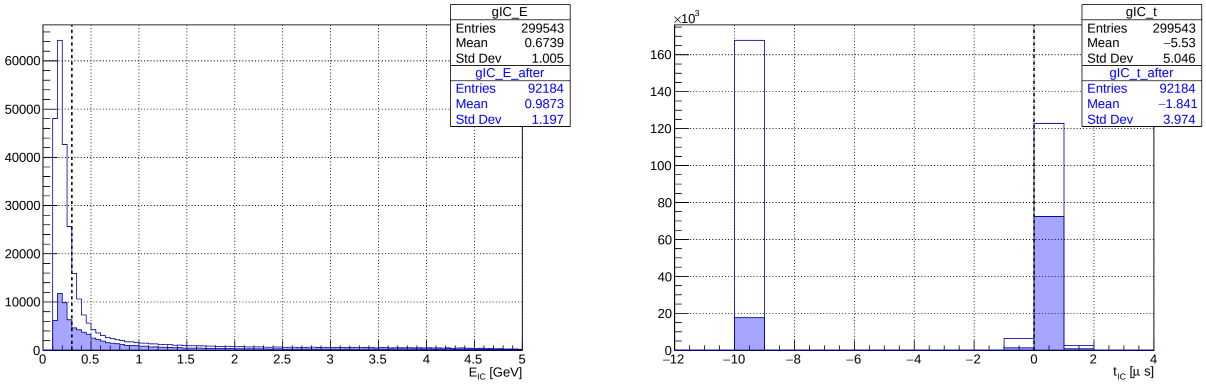

(a) Energy Cut: Lower energy particles are poorly reconstructed due to energy loss and radiative effects are rejected.

(b) Timing Cut: Particles with no IC cluster timing information are just background when forming photon pairs [1].

5.2.2 Timing Cut

Events that do not have cluster timing information are automatically placed at some fixed negative value. To exclude these poorly reconstructed particles, a cut on the cluster time is applied:

(5.1) `tc[iic] > 0 ,`

with `tc` being the array in the `ICPB` bank that has cluster timing information in ns. The disitribution, in μs, and cuts can be seen in **Fig. 5.5b**.

5.2.3 Møller Electron Cut

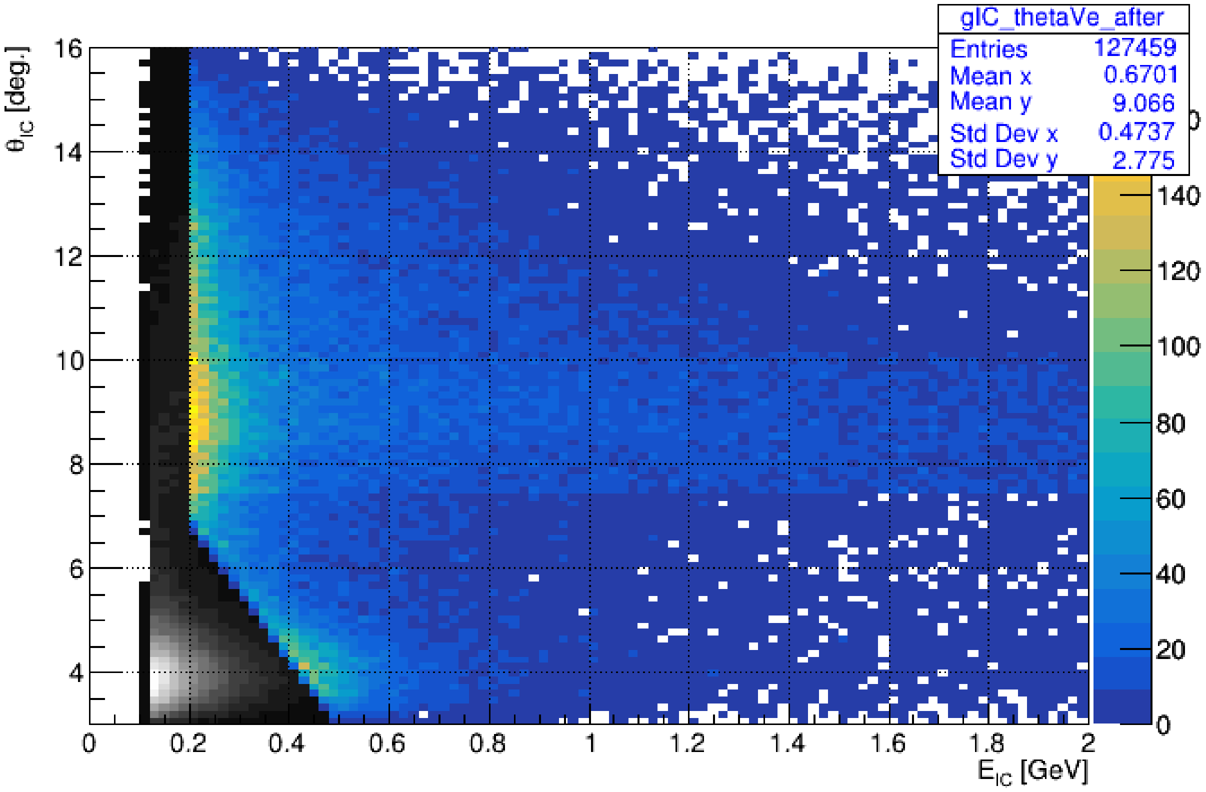

Figure 5.6: Møller Electron Cut: A geometric cut is applied to reject low-energy, low-angle Møller electrons

The number of pesky Møller electrons are minimized by the field produced by the solenoid but some still make it to the IC since the IC is designed to have acceptance of low-polar angle photons. A geometrical cut is introduced to deal with these:

$$\texttt{!isInMollerRegion(etc[iic], theta),} \tag{5.1}$$

where `theta`, in degrees, is obtained from the position vector $\vec{r}_{\text{IC}}$:

$$\vec{r}_{\text{IC}} = \begin{bmatrix} \texttt{xc[iic]} \\ \texttt{yc[iic]} \\ \texttt{zc[iic] - vz\_e} \end{bmatrix}$$

with `vz_e` being the z-component of the trigger electron's vertex and `xc`, `yc`, and `zc` being IC hit positions in cm.

Explicitly, `isInMollerRegion` can be expressed as

```
isInMollerRegion( theta, E ){
  if( E < m * theta + b ) return true
  return false
}
```

with `m` the slope and `b` is the intercept of the cut having values:

```
m = -0.3/4
b =  2.9/4
```

5.2.4 Hot Channels Cut

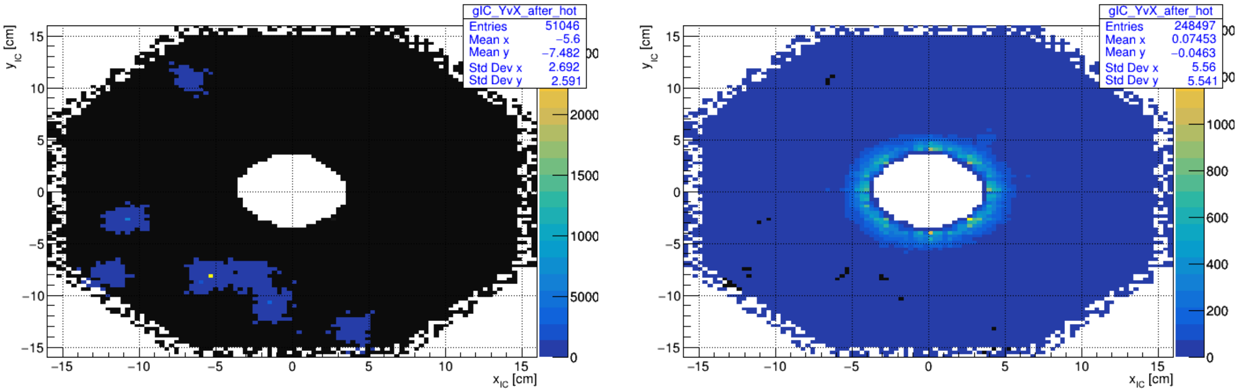

(a) Rejected hot channels.

(b) Accepted channels.

Figure 5.7: Hot Channels Cut: The position of the hits in the IC that are rejected (5.7a) and accepted (5.7b) by the cut.

Over the course of the experiment, some crystals were overheated and were registering many more hits than all other crystals. To deal with this, we reject these hot crystals:

(5.1)
```
!isInICHotChannel(ix, iy)
```

where

```
ix = (int) round(x_ichb/dx)
iy = (int) round(y_ichb/dy)
```

are the pixel indices for `x_ichb` and `y_ichb`, the x- and y- positions, in cm, of the `ICHB` bank given by

```
x_ichb = ich_xgl[ihit]
y_ichb = ich_ygl[ihit]
```

with `ihit` being the hit ID in the `ICHB` bank given by

```
ihit = (statc[iic] - statc[iic]%10000) / 10000 - 1 .
```

The hard-coded values `dx` and `dy` are the width and height of each crystal with values tabulated in **Table 5.1**.

Table 5.1: Hard-Coded IC Values

Variable	Value	Units
dx	1.346	cm
dy	1.360	cm

5.2.5 IC Fiducial Cut

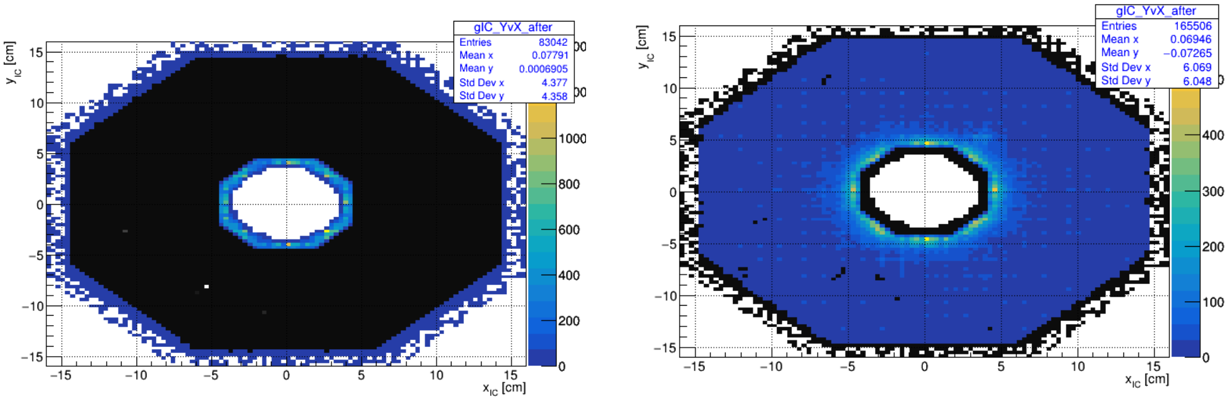

(a) Rejected IC hits.

(b) Accepted IC hits that pass both the Hot Channels and IC Fiducial Cuts.

Figure 5.8: IC Fiducial Cut: The position of the hits in the IC that are rejected (5.8a) by the cut and accepted (5.8b) by both the Hot Channels and Fiducial Cuts (to see features).

To ignore poor reconstruction of photons hitting the edges of the IC, are ignored. The fiducial cut follows the procedure outlined by F.X. Girod [21]:

(5.1) `isInICFiducial(x,y)`

here `isInICFiducial` is a method that depends on the IC hit positions, `x` and `y` and can be broken down into two parts:

```
isInICFiducial(x,y){
  if( isOutICOuterEdge(x,y) ) return false
  if( isInICnnerEdge(x,y)   ) return false
  return true
}
```

The x- and y- positions of the hits, `x` and `y` are given by:

```
x = xc[iic]
y = yc[iic]
```

where `xc` and `yc` are arrays from the `ICPB` bank that hold the x- and y- positions of the hit in cm.

`isOutICOuterEdge` returns whether or not the point (`x,y`) is outside the outer edge of the IC and `isInICInnerEdge` returns whether or not the point is inside the inner edge of the IC. Their explicit psuedocode is given in **Appendix B.3**.

The accepted IC photons take momentum

$$P_\gamma = (\vec{\boldsymbol{p}}_\gamma, E_\gamma)$$

where

$$\vec{\boldsymbol{p}}_\gamma = E_\gamma \hat{\boldsymbol{r}}_{\text{IC}}$$

$\hat{\boldsymbol{r}}_{\text{IC}}$ being the direction vector coming from the IC hit position vector w.r.t target, $\vec{\boldsymbol{r}}_{\text{IC}}$, defined in **Section 5.2.3** and the energy is:

$$E_\gamma = \texttt{etc[iic]}$$

----

6. Helium Identification (^{4}HeID)

$$e\,^4\mathrm{He} \rightarrow e'\,^4\mathrm{He}'\gamma\gamma$$

The recoiled ^{4}He identification is done by its own series of tests/cuts. Particles passing all of these tests are taken to be good tracks and will be subjected to event selection after.

For the following procedure, the iteration variables `igcpb` will loop over the `GCPB` bank from 0 to `gcpart` and `irtpc` will loop over the `RTPC` bank from 0 to `rtpc_npart`.

6.1 Pre-Cuts

Particles failing any one of these pre-cuts are skipped over entirely. These are the minimal requirements to identifying the helium.

6.1.1 Number of Pads Cut

Poor track reconstruction in the RTPC is due to too few pads firing. We therefore cut on:

$$\texttt{npd\_track[igcpb] > 3} \;, \tag{6.1}$$

where `npd_track` is the `GCPB` bank array that is filled with the number of pads fired for a given track.

6.1.2 Charge Cut

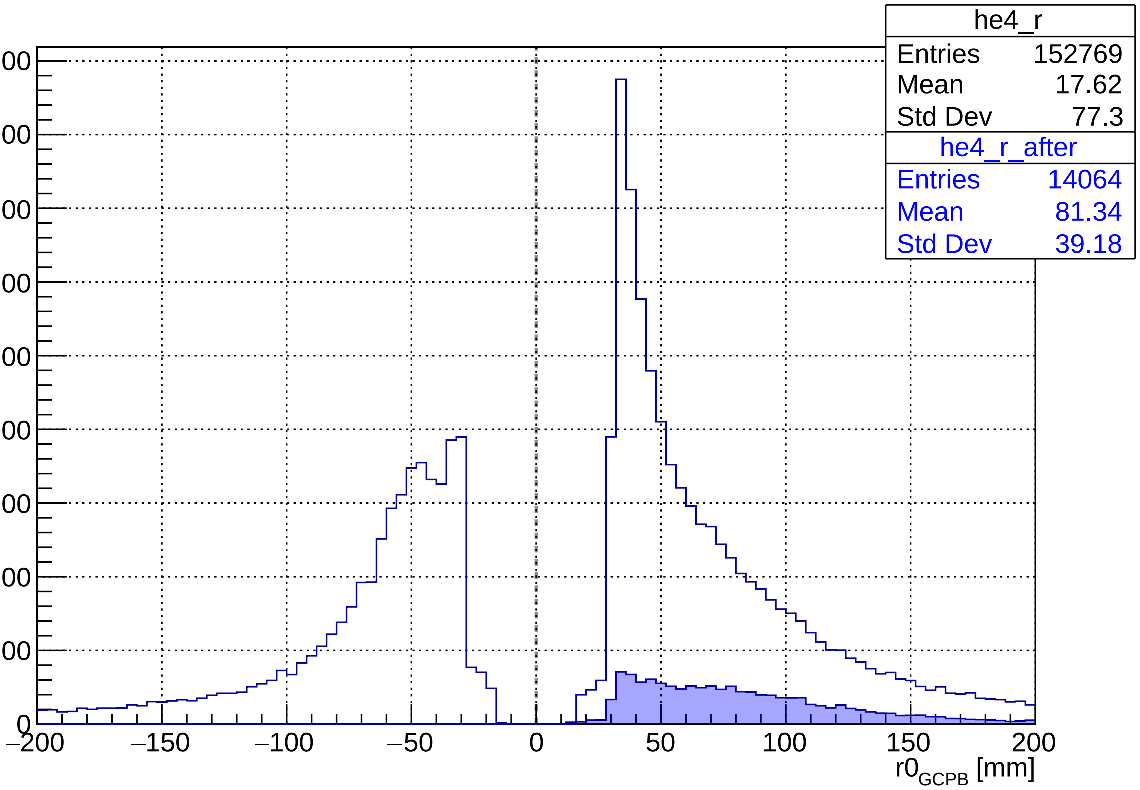

Figure 6.1: Charge Cut: Negatively charged tracks (negative radius of curvature) are thrown out.

To remove tracks of negatively charged particles, we throw away all tracks except for the ones with positive radius of curvature:

(6.1) `r_0[igcpb] > 0 ,`

where `r_0` is the `GCPB` bank array that is filled with the radius of curvature in mm, where the sign of the curvature corresponds to the sign of the particle.

6.2 χ^2 Cut

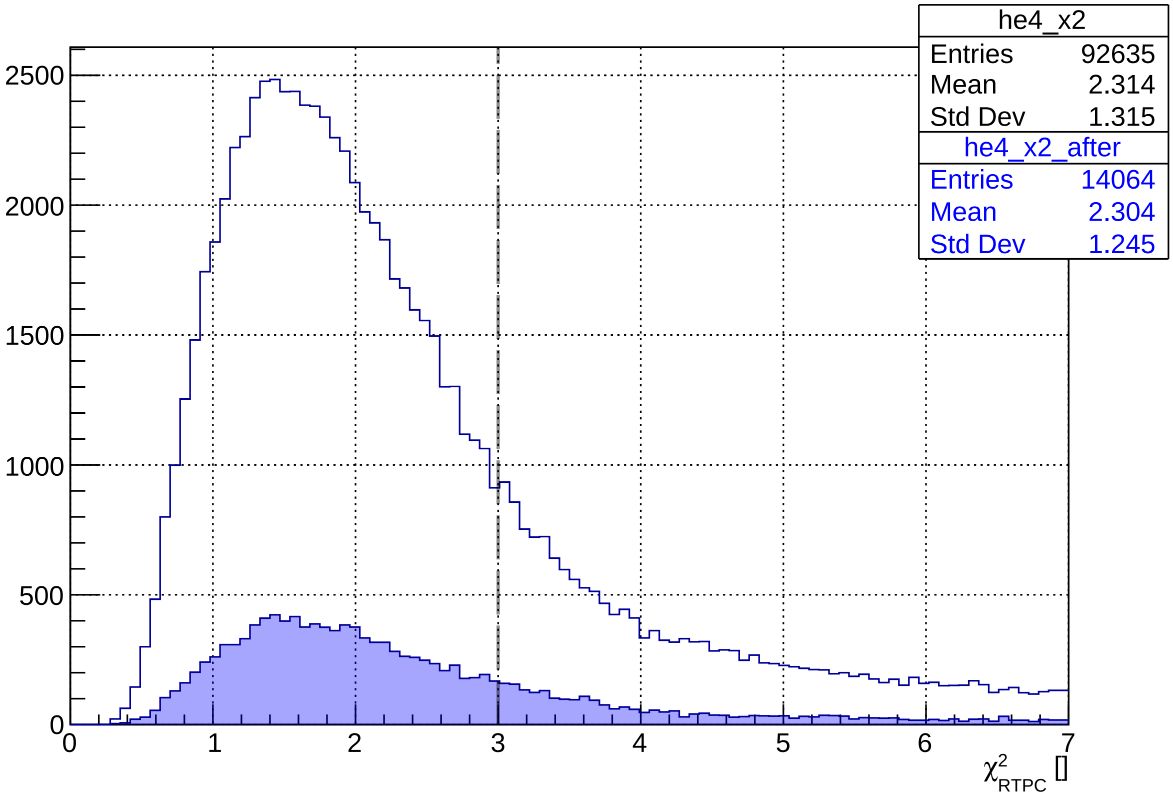

Figure 6.2: χ^2 Cut: The χ^2-distribution obtained from fitting the RTPC tracks correspond to how well the ionization points are fit. High χ^2, corresponding to poor fits, are rejected.

The quality of the track fit is encompassed by the χ^2-distribution. A low χ^2 signifies the fit to the hypothesized modified helix is satisfactory for the given number of degrees of freedom. To select the good fits, a cut on the χ^2 distribution is made:

(6.1) `x2[igcpb] < 3 ,`

where `x2` is the `GCPB` bank array that is filled with the calculated χ^2 for each track.

6.3 `edist` Cut

The end-distance, or `edist`, is the distance from the last point of ionization to the anode. We want to be sure that the last ionization point is coming from well within the drift region of the RTPC but at the same time close enough to the anode so that the track has ionization points spaced out:

(6.1) `-5 < edist[igcpb] && edist[igcpb] < 10 ,`

where `edist` is the `GCPB` bank array that is filled with the end-distance in mm. The distributions and the cuts can be seen in **Fig. 6.3a**.

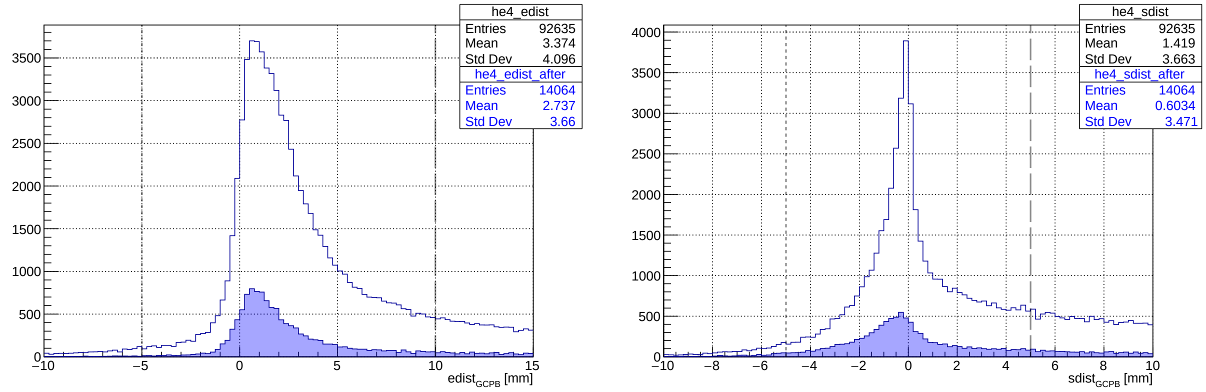

(a) `edist` Cut: Ionization too far from the anode are rejected. **(b)** `sdist` Cut: Ionization too far from the cathode are rejected.

Figure 6.3: Ionization Cuts

6.4 `sdist` Cut

The start-distance, or `sdist`, is the distance from the first ionization point to the cathode. For similar reasons as the cuts in **Section 6.3**, a cut is placed on the `sdist` distributions:

(6.1) `-5 < sdist[igcpb] && sdist[igcpb] < 5 ,` where `sdist` is the `GCPB` bank array that is filled with the start-distance in mm. The distributions and the cuts can be seen in **Fig.** 6.3b.

6.5 θ_{RTPC} Cut

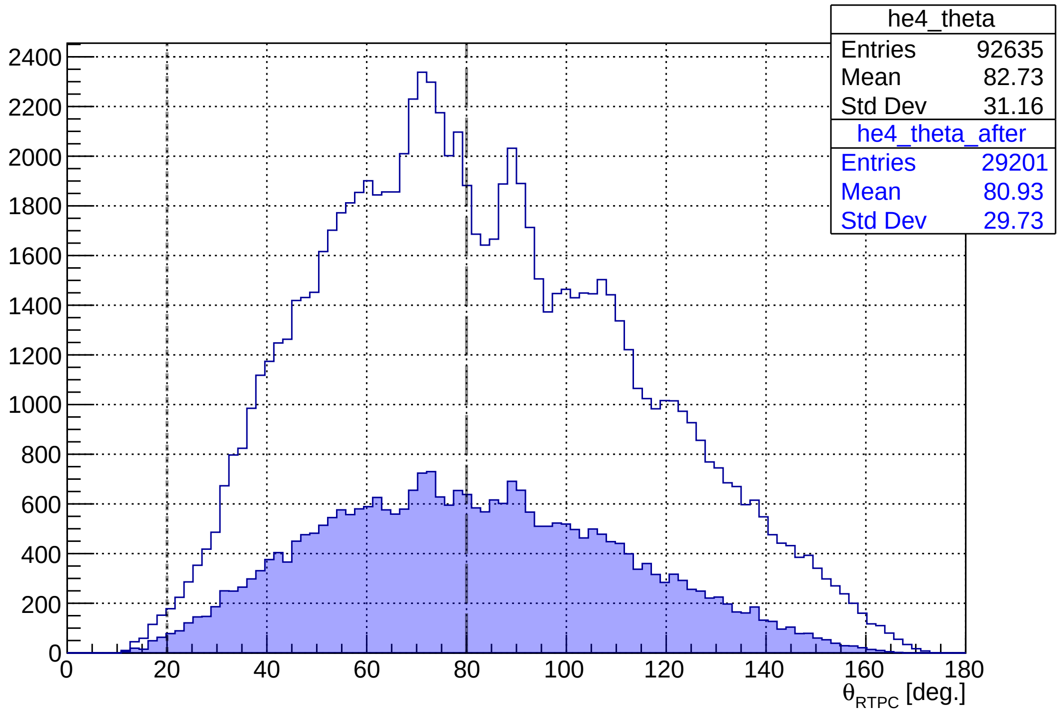

Figure 6.4: θ Cut: Backward traveling tracks are rejected.

Backward tracks, w.r.t the beam, and low polar-angle tracks are rejected. Polar angles in the range

$$20 < \mathtt{theta_{deg}} \ \&\& \ \mathtt{theta_{deg}} < 80 \ , \tag{6.1}$$

are accepted, where $\mathtt{theta_{deg}}$ is the corrected θ_{RTPC} (see **Appendix** A.2.1) in degrees. The distributions that pass all other cuts, no cuts, and the value of the cuts are shown in **Fig.** 6.4.

6.6 Vertex Cut

To ensure that the track is coming from inside the target and the RTPC, a vertex cut is applied:

(6.1) `abs( vz_mm ) < 110 ,`

where `vz_mm` is the corrected vertex vz_{RTPC} (see **Appendix A.2.2**) but in mm. The distributions of no cuts, all other cuts are shown in **Fig. 6.5b**, with the cuts shown as lines.

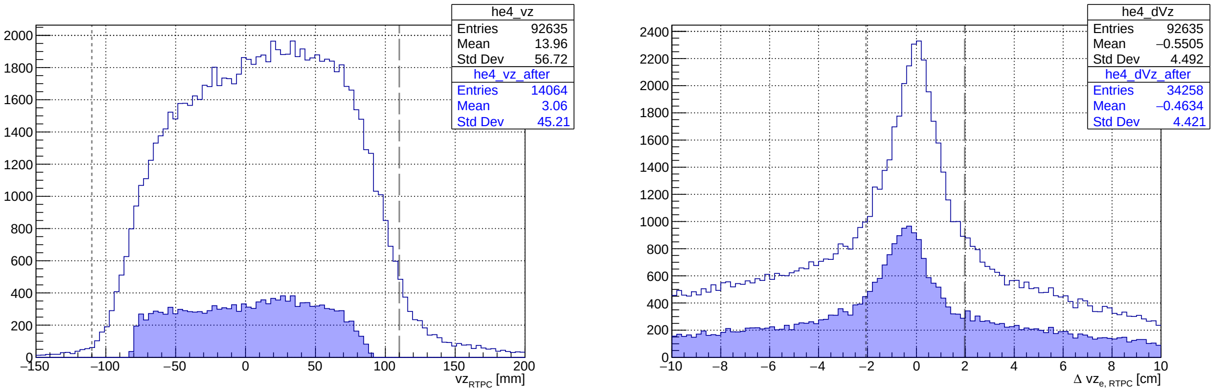

(a) Vertex Cut: Corrected, reconstructed vertices from outside the RTPC are rejected.

(b) Vertex Coincidence Cut: Vertices that are too far from the trigger electron are rejected.

Figure 6.5: RTPC Vertex Cuts

6.7 Vertex Coincidence Cut

To reasonably tie the track to coincide with the scattered electron, the vertex coincidence, `Dvz` distribution is cut on:

(6.1) `abs( Dvz - mu_Dvz ) < 3.5 sigma_Dvz ,`

where

```
mu_Dvz    = -0.043
sigma_Dvz =  0.673
```

are previously studied means and widths for the distribution and `Dvz` is the distance between the corrected vertex (see **Appendix A.2.2**) and the electron's vertex, are all in cm. The distributions are shown in **Fig. 6.5b**.

6.8 RTPC Fiducial Cuts

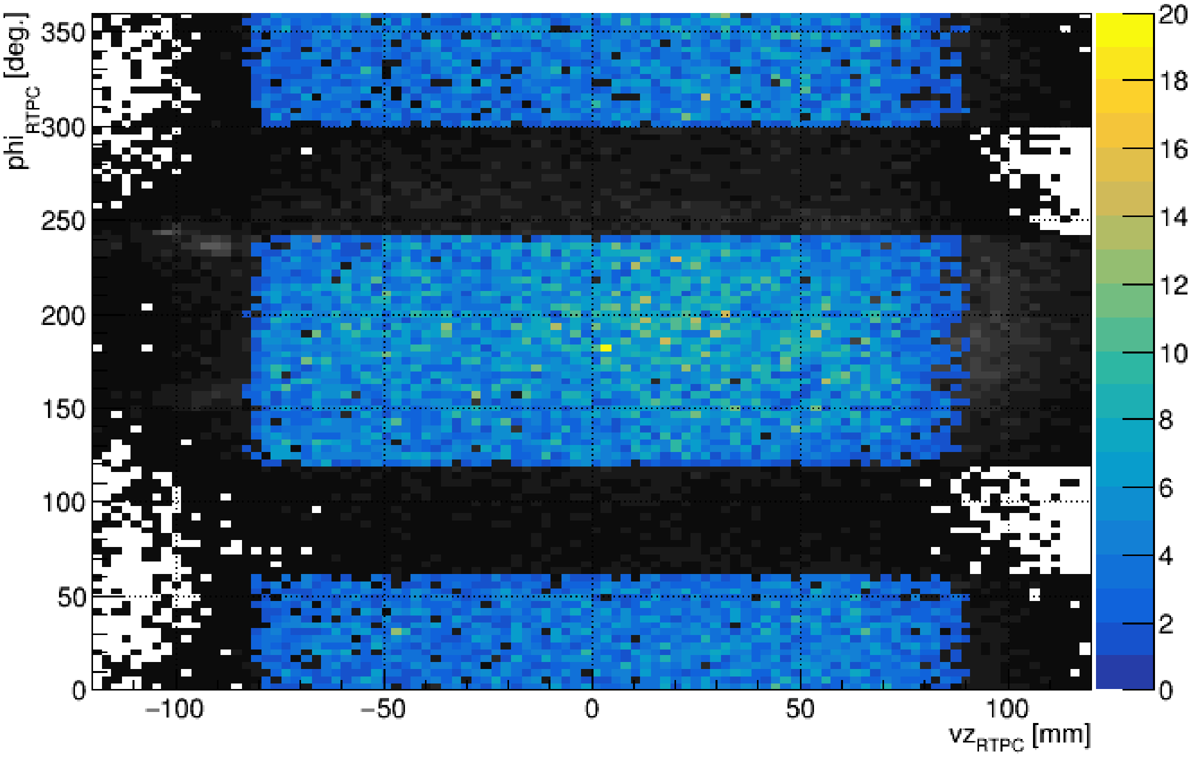

Figure 6.6: RTPC Fiducial Cuts: Distributions of the RTPC hits that fail the cuts are grayscale and the hits that pass are in color.

For good track reconstruction, the particle should (1) be within the anode and cathode, (2) not hit the top or bottom support regions, and (3) not hit the upstream target holder nose. A fiducial cut is applied to reject these troublesome tracks:

(6.1) `isInRTPCFiducial(vz, theta, phi)`

here `isInRTPCFiducial` is a method that depends on the track's corrected vertex, `vz`, corrected polar angle `theta`, and azimuthal angle, `phi`. It is a test that passes only if all three of subtests pass.

```
isInRTPCFiducial(vz, theta, phi){
  if( !isInRTPCDrift(vz, theta)   ) return false
  if(  isInRTPCSupport(phi)       ) return false
  if(  isInRTPCHolder(vz, theta)  ) return false
  return true
}
```

The helium that makes it through these cuts takes momentum

$$P_{^4\mathrm{He}} = (\vec{\boldsymbol{p}}_{^4\mathrm{He}}, E_{^4\mathrm{He}})$$

where

$$\vec{\boldsymbol{p}}_{^4\mathrm{He}} = p_{^4\mathrm{He}} \hat{\boldsymbol{r}}_{\mathrm{RTPC}}$$

where $\hat{\boldsymbol{r}}_{\mathrm{RTPC}}$ is the direction vector, uniquely defined by ϕ_{RTPC} = `rtpc_phi[irtpc]` and the corrected θ_{RTPC} (see **Appendix A.2.1**). The energy is:

$$E_{^4\mathrm{He}} = \sqrt{p^2_{^4\mathrm{He}} + M^2_{^4\mathrm{He}}} \quad ,$$

where $M_{^4\mathrm{He}}$ is the nominal value for the helium mass of 3.7284 GeV/c^2 and $p_{^4\mathrm{He}}$, in GeV/c, is:

$$p_{^4\mathrm{He}} = \texttt{rtpc\_p}i\texttt{[irptc] / 1000} \quad .$$

Here $i \in \{1, \ldots, 5\}$ is the first index where `rtpc_id`i `== 47` is satisfied. This condition tells which Bethe-Bloche curve the point $(p/q, dE/dx)$ is closest to (see **Fig. 6.7**), and is enumerated in **Table 6.1**.

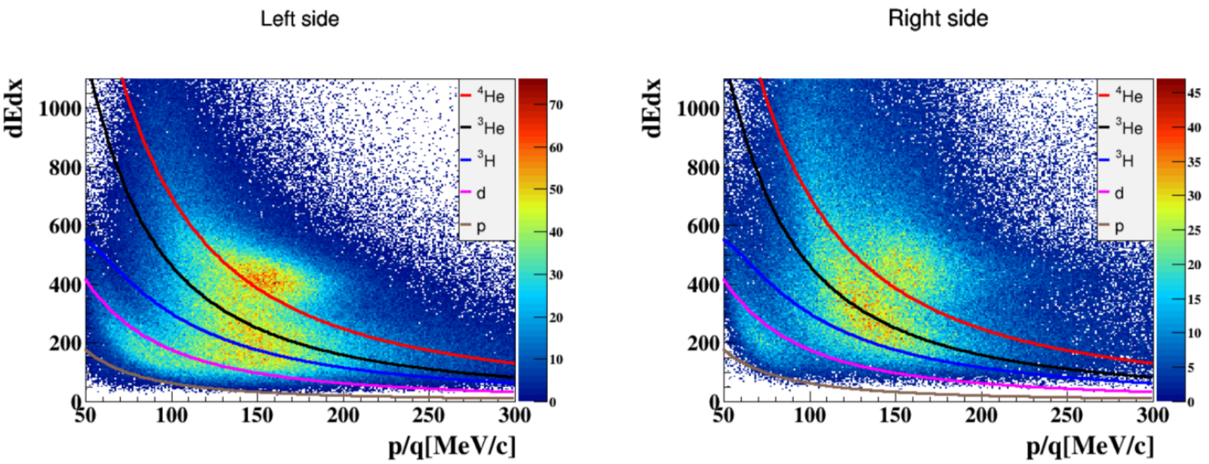

Figure 6.7: Bethe-Bloch curves overlaying the dE/dx vs. p/q distributions for the left and right sides of the RTPC [4].

Table 6.1: Index table for `rtpc_id`i

i	**Particle**
1	^{4}He
2	^{3}He
3	^{3}H
4	d
5	p

`rtpc_phi`, `rtpc_p`i, and `rtpc_id`i are `RTPC` bank arrays with `rtpc_phi` holding the azimuthal angle in rad. and `rtpc_p`i holding the energy-loss corrected momentum at vertex in MeV/c.

- -

IV. Event Selection Method I: Exclusivity Cuts

Before going into kinematic fitting, an overview of the standard and previously used technique [1,15] of exclusivity cuts is shown. First, definitions of the exclusivity variables are introduced. Then, distributions of these variables will be subjected to the cuts that will later be compared to the distributions produced from kinematic fitting.

7. Exclusivity Variable Definitions

Table 7.1: Configurations: X denotes produced particle (γ for DVCS and π^0 or η for DVMP). Grayed out particles are not measured.

Index	**Configuration**	
i	init.	fin.$_i$
0	$e\ ^4\text{He} \rightarrow$	$e\ ^4\text{He}\ X$
1	$e\ ^4\text{He} \rightarrow$	$e\ ^4\text{He}\ X$
2	$e\ ^4\text{He} \rightarrow$	$e\ ^4\text{He}\ X$

Let X$_i$ denote the missing particle in the final state configuration, indexed by i (listed in **Table 7.1**) and P_{Beam} and P_{Targ} denote the initial electron and helium, respectively. Then the following subsections define the exclusivity varibles to cut on.

7.1 Missing Mass^2: $M^2_{X_i}$

For missing 4-momentum P_{X_i},

$$\begin{aligned} P_{X_i} &= P_{\text{init}} - P_{\text{fin}_i} \\ &= \left(P_{\text{Beam}} + P_{\text{Targ.}}\right) - P_{\text{fin}_i} \end{aligned} \quad ,$$

where P_{fin_i} is the sum of the final state particles not grayed out in **Table 7.1**. We define the missing mass^2, $M^2_{X_i}$, to be

$$M^2_{X_i} = P^2_{X_i} = E^2_{X_i} - \|\vec{\boldsymbol{p}}_{X_i}\|^2 \quad .$$

The expected value, of a perfect measurement, of $M^2_{X_i}$ would be the nominal value-squared of the grayed out particle for the i-th configuration in **Table 7.1**.

7.2 Missing Momenta: $px_{X_2}, py_{X_2}, pt_{X_2}$

There are three components to the missing momenta to consider when applying exclusivity cuts: px_{X_2}, py_{X_2}, and pt_{X_2}.

py_{X_2} and py_{X_2} are the transverse x- and y- components and pt_{X_2} the magnitude of P_{X_2}:

$$pt_{X_2} = \sqrt{px^2_{X_2} + py^2_{X_2}} \quad .$$

The expected value, in a perfect measurement would have all of these be identically zero.

7.3 Missing Energy: E_{X_2}

The missing energy, E_{X_2} is just the energy component of P_{X_2}:

$$\begin{aligned} E_{X_2} &= E_{\text{init}} - E_{\text{fin}_2} \\ &= E_{\text{Beam}} + E_{\text{Targ.}} - (E_e + E_{^4\text{He}} + E_X) \end{aligned}$$

The expected value, in a perfect measurement, would have this be identically zero.

7.4 Cone angle: $\theta_{X_1,X}$

Cone angle, θ, is the angle between the 3-vectors of the missing and measured particle, following from:

$$\cos\theta = \frac{\vec{\boldsymbol{p}}_{X_1} \cdot \vec{\boldsymbol{p}}_X}{\|\vec{\boldsymbol{p}}_{X_1}\|\|\vec{\boldsymbol{p}}_X\|} \quad .$$

The expected value, in a perfect measurement, would have this be identically zero.

7.5 Coplanarity Angle: $\Delta\phi_{^4\mathrm{He},\ \gamma^*,\ X}$

The coplanarity angle measures the coplanarity between the scattered helium, ^{4}He, the virtual photon, γ^*, and the produced particle, X. Practically, this is measured by measuring the angle between the normal vectors of the plane defined by the virtual photon and final state helium; and the virtual photon and the produced particle. Let the norms to the planes $P1$ and $P2$ be defined as:

$$\begin{aligned} \vec{\boldsymbol{p}}_{P1} &= \vec{\boldsymbol{p}}_{^4\mathrm{He}} \times \vec{\boldsymbol{p}}_{\gamma^*} \\ \vec{\boldsymbol{p}}_{P2} &= \vec{\boldsymbol{p}}_{^4\mathrm{He}} \times \vec{\boldsymbol{p}}_X \end{aligned} \quad .$$

Then $\Delta\phi$ follows from

$$\cos\Delta\phi = \frac{\vec{\boldsymbol{p}}_{P1} \cdot \vec{\boldsymbol{p}}_{P2}}{\|\vec{\boldsymbol{p}}_{P1}\|\|\vec{\boldsymbol{p}}_{P2}\|} \quad .$$

The expected value, in a perfect measurement, would have this be identically zero.

V. Event Selection Method II: Kinematic Fitting

8. Formalism

An alternative to selecting events from a series of user-defined cuts is to apply kinematic fitting. Kinematic fitting takes in a set of measurements; the detectors' known resolutions and studied errors; a set of constraints; and produces a set of measurements that better satisfies the constraints. Measurements of momentum vectors along with conservation of momentum and energy of an exclusive process are ideal candidates for this procedure and additional constraints can be added as needed.

8.1 Pre-fit: Setting up

This method is a least squares fit that follow the recipe using Lagrange multipliers. The Lagrange multipliers are free parameters that extremizes a Lagrangian that balances the minimization of a χ^2 while satisfying a set of constraints. Thus, the ingredients that need to be constructed are χ^2 and a set of constraints. The following will sections will be using notation mostly from [6,7] and a bit from [5,10].

8.1.1 Constructing Constraints

Let $\vec{\eta}$ be a vector of n-measured variables. Then the true vector of the n-variables, $\vec{y}$, will have an associated error vector of n-variables, $\vec{\varepsilon}$. They are related simply by:

$$\vec{y} = \vec{\eta} + \vec{\varepsilon}$$

If there are, say m, unmeasured variables too, then they can be put in a vector, $\vec{x}$. The two vectors, $\vec{x}$ and $\vec{y}$, are then related by r constraint equations, indexed by k:

$$f_k(\vec{x},\vec{y}) = 0$$

Suppose $\vec{x}^0$ and $\vec{y}^0$ are our best guess or measurements of the vectors $\vec{x}$ and $\vec{y}$, respectively. Then Taylor expanding to first order each $f_k(\vec{x},\vec{y})$ about $\vec{x}^0$ and $\vec{y}^0$ gives:

$$f_k(\vec{x},\vec{y}) \approx f_k\left(\vec{x}^0,\vec{y}^0\right) + \sum_{i=0}^{m}\left(\frac{\partial f_k}{\partial x_i}\right)\bigg|_{\left(\vec{x}^0,\vec{y}^0\right)}\left(x_i - x_i^0\right) + \sum_{j=0}^{n}\left(\frac{\partial f_k}{\partial y_j}\right)\bigg|_{\left(\vec{x}^0,\vec{y}^0\right)}\left(y_j - y_j^0\right)$$

where

- x_i, y_j are the ith and jth components of $\vec{x}$, $\vec{y}$ and
- x_i^0, y_j^0 are the ith and jth components of $\vec{x}^0$, $\vec{y}^0$,

respectively.

If the initial guesses or measurements are insufficient (to be explained in **Section 8.3**), better $\vec{y}$ and $\vec{x}$ can be obtained from repeated linearization. So for the ν-th iteration, we have:

$$f_k^\nu := f_k(\vec{x}^\nu,\vec{y}^\nu) \approx f_k\left(\vec{x}^{\nu-1},\vec{y}^{\nu-1}\right) + \sum_{i=0}^{m}\left(\frac{\partial f_k}{\partial x_i}\right)^\nu\left(x_i^\nu - x_i^{\nu-1}\right) + \sum_{j=0}^{n}\left(\frac{\partial f_k}{\partial y_j}\right)^\nu\left(y_j^\nu - y_j^{\nu-1}\right) \tag{8.1}$$

that depends just on the previous, $(\nu-1)$-th iteration, where [2]

$$\begin{aligned}\left(\frac{\partial f_k}{\partial x_i}\right)^\nu &:= \left(\frac{\partial f_k(\vec{x},\vec{y})}{\partial x_i}\right)\bigg|_{\left(\vec{x}^{\nu-1},\vec{y}^{\nu-1}\right)} \\ \left(\frac{\partial f_k}{\partial y_j}\right)^\nu &:= \left(\frac{\partial f_k(\vec{x},\vec{y})}{\partial y_j}\right)\bigg|_{\left(\vec{x}^{\nu-1},\vec{y}^{\nu-1}\right)}\end{aligned} \quad .$$

---

[2] The reasons for labeling the iteration index for the derivatives ν and not $(\nu-1)$ will become apparent later in implementing the fit.

For convenience, let's introduce

$$\begin{aligned} A^{\nu}_{ij} &:= \left(\frac{\partial f_i}{\partial x_j}\right)^{\nu} \\ B^{\nu}_{ij} &:= \left(\frac{\partial f_i}{\partial y_j}\right)^{\nu} \\ c^{\nu}_{i} &:= f_i\left(\vec{\boldsymbol{x}}^{\nu-1}, \vec{\boldsymbol{y}}^{\nu-1}\right) \end{aligned} \quad , \tag{8.2}$$

and

$$\begin{aligned} \vec{\boldsymbol{\xi}}^{\nu} &:= \vec{\boldsymbol{x}}^{\nu} - \vec{\boldsymbol{x}}^{\nu-1} \\ \vec{\boldsymbol{\delta}}^{\nu} &:= \vec{\boldsymbol{y}}^{\nu} - \vec{\boldsymbol{y}}^{\nu-1} \\ \vec{\boldsymbol{\epsilon}}^{\nu} &:= \vec{\boldsymbol{y}}^{\nu} - \vec{\boldsymbol{\eta}} \\ &= \vec{\boldsymbol{y}}^{\nu} - \vec{\boldsymbol{y}}^{0} \end{aligned} \quad .$$

Then, since $f_k\left(\vec{\boldsymbol{x}}, \vec{\boldsymbol{y}}\right) \equiv 0 \;\; \forall k$, **Eq. 8.1** can be written in succinct matrix form as:

$$\vec{\boldsymbol{0}} \equiv A^{\nu}\vec{\boldsymbol{\xi}}^{\nu} + B^{\nu}\vec{\boldsymbol{\delta}}^{\nu} + \vec{\boldsymbol{c}}^{\nu} \tag{8.3}$$

where A^{ν} and B^{ν} are $(r \times n)$ and $(r \times m)$ matrices with components A^{ν}_{ij} and B^{ν}_{ij}, respectively, as defined by **Eqs. 8.2**. These will be our constraints moving forward.

8.1.2 Constructing χ^2

Now, if the correlations between the measured values are well understood, a covariance matrix, C_{η}, can be constructed from a vector of the resolution errors of $\vec{\boldsymbol{\eta}}$ (namely, $\vec{\boldsymbol{\sigma}}_{\eta}$), and a symmetric correlation matrix, ρ_{η}, whose components, $\left(\rho_{\eta}\right)_{ij} \in [-1, 1]$, house pairwise correlations coefficients between components η_i and η_j:

$$C_{\eta} = \vec{\boldsymbol{\sigma}}_{\eta}\rho_{\eta}\vec{\boldsymbol{\sigma}}^{T}_{\eta} \quad .$$

Then let's define χ^2, to account for correlations, for the ν-th iteration, as:

$$\chi^2_\nu = (\vec{\boldsymbol{\epsilon}}^\nu)^T\, C_\eta^{-1}\, \vec{\boldsymbol{\epsilon}}^\nu.$$

Note, if there are no correlations, then ρ_η is the unit matrix and so the covariance matrix becomes just a diagonal matrix of the variances, $C_\eta = \mathrm{diag}\left(\overrightarrow{\boldsymbol{\sigma}_\eta^2}\right)$. In this case:

$$\chi^2_\nu = (\vec{\boldsymbol{\epsilon}}^\nu)^T \left(\vec{\boldsymbol{\sigma}}\ \vec{\boldsymbol{\sigma}}^T\right)^{-1} \vec{\boldsymbol{\epsilon}}^\nu = \sum_{i=0}^{n} \frac{\left(y_i^\nu - y_i^0\right)^2}{\left(\sigma_\eta^2\right)_i} = \sum_{i=0}^{n} \frac{\left(y_i^\nu - \eta_i\right)^2}{\left(\sigma_\eta^2\right)_i} = \sum_{i=0}^{n} \frac{\left(\epsilon_i^\nu\right)^2}{\left(\sigma_\eta^2\right)_i}$$

becomes the recognizable χ^2, that follows a χ^2-distribution for n degrees of freedom.

8.2 Fitting

Given this χ^2 and the set of constraints above, we naturally introduce a Lagrangian, $\mathcal{L}$, with Lagrange multipliers $\vec{\boldsymbol{\mu}}$ such that:

$$\mathcal{L}\left(\vec{\boldsymbol{\mu}}, \vec{\boldsymbol{\delta}}, \vec{\boldsymbol{\xi}}\right) = \vec{\boldsymbol{\epsilon}}^T C_\eta^{-1} \vec{\boldsymbol{\epsilon}} + 2\vec{\boldsymbol{\mu}}^T \left(A\vec{\boldsymbol{\xi}} + B\vec{\boldsymbol{\delta}} + \vec{\boldsymbol{c}}\right) \tag{8.1}$$

is to be minimized.

8.2.1 Solving for Fitted Values

Explicitly, with the iteration index ν, the minimization conditions are:

$$\vec{\boldsymbol{0}} \equiv \frac{1}{2}\left(\frac{\partial \mathcal{L}}{\partial \vec{\boldsymbol{\delta}}}\right)^\nu = C_\eta^{-1} \vec{\boldsymbol{\epsilon}}^\nu + (B^\nu)^T\, \vec{\boldsymbol{\mu}}^\nu \tag{8.1a}$$

$$\vec{\boldsymbol{0}} \equiv \frac{1}{2}\left(\frac{\partial \mathcal{L}}{\partial \vec{\boldsymbol{\mu}}}\right)^\nu = A^\nu \vec{\boldsymbol{\xi}}^\nu + B^\nu \vec{\boldsymbol{\delta}}^\nu + \vec{\boldsymbol{c}}^\nu \tag{8.1b}$$

$$\vec{\boldsymbol{0}} \equiv \frac{1}{2}\left(\frac{\partial \mathcal{L}}{\partial \vec{\boldsymbol{\xi}}}\right)^\nu = (A^\nu)^T\, \vec{\boldsymbol{\mu}}^\nu \tag{8.1c}$$

Solving for such $\vec{\boldsymbol{\mu}}^{\nu}, \vec{\boldsymbol{\delta}}^{\nu}, \vec{\boldsymbol{\xi}}^{\nu}$ that satisfy **Eqs. 8.1**s' conditions results in:

$$\vec{\boldsymbol{\xi}}^{\nu} = -C_x^{\nu} \left(A^{\nu}\right)^T C_B^{\nu} \vec{\boldsymbol{r}}^{\nu} \tag{8.2a}$$

$$\vec{\boldsymbol{\mu}}^{\nu} = C_B^{\nu} \left(A^{\nu} \vec{\boldsymbol{\xi}}^{\nu} + \vec{\boldsymbol{r}}^{\nu}\right) \tag{8.2b}$$

$$\vec{\boldsymbol{\delta}}^{\nu} = -C_{\eta} \left(B^{\nu}\right)^T \vec{\boldsymbol{\mu}}^{\nu} - \vec{\boldsymbol{\epsilon}}^{\nu-1} \tag{8.2c}$$

where C_B, C_x, and $\vec{\boldsymbol{r}}^{\nu}$ are defined for convenience as

$$\begin{aligned} C_B^{\nu} &:= \left[B^{\nu} C_{\eta} \left(B^{\nu}\right)^T\right]^{-1} \\ C_x^{\nu} &:= \left[\left(A^{\nu}\right)^T C_B^{\nu} A^{\nu}\right]^{-1} \\ \vec{\boldsymbol{r}}^{\nu} &:= \vec{\boldsymbol{c}}^{\nu} - B^{\nu} \vec{\boldsymbol{\epsilon}}^{\nu-1} \end{aligned} \quad . \tag{8.3}$$

To see this explicitly, see **Appendix C.**.

With these vectors that satisfy the minimization condition, we can finally form our new fitted vectors $\vec{\boldsymbol{x}}$ and $\vec{\boldsymbol{y}}$:

$$\begin{aligned} \vec{\boldsymbol{x}}^{\nu} &= \vec{\boldsymbol{x}}^{\nu-1} + \vec{\boldsymbol{\xi}}^{\nu} \\ \vec{\boldsymbol{y}}^{\nu} &= \vec{\boldsymbol{y}}^{\nu-1} + \vec{\boldsymbol{\delta}}^{\nu} \end{aligned} \tag{8.4}$$

8.2.2 Minimizing χ^2

A simple minimization of χ^2 is deployed by iterating over the fit and stopping as soon as χ^2 increases, after the first iteration.

8.2.3 New Errors from Fit

The new covariance matrices, obtained from propagation of errors (See [5]), are C_x^ν (See **Eq. 8.3**) and C_y^ν :

$$\begin{aligned} C_y^\nu &= \left(\frac{\partial \vec{y}}{\partial \vec{\eta}}\right) C_\eta \left(\frac{\partial \vec{y}}{\partial \vec{\eta}}\right)^T \\ &= C_\eta - C_\epsilon^\nu \end{aligned} ,$$

where C_ϵ^ν and its intermediate matrices are defined as:

$$\begin{aligned} C_\epsilon^\nu &:= C_\eta G^\nu C_\eta - C_\eta H^\nu C_x^\nu \left(H^\nu\right)^T C_\eta; \\ G^\nu &:= \left(B^\nu\right)^T C_B^\nu B^\nu \\ H^\nu &:= \left(B^\nu\right)^T C_B^\nu A^\nu \end{aligned} .$$

8.3 Post-fit: Fit Quality

To check on the quality of the fit, we look to two sets of distributions: The **Confidence Level distribution** and the **Pull distributions**. Again, omission of the iteration index ν denotes the best fitted, final values.

8.3.1 Confidence Level

Since $\chi^2 (= \vec{\epsilon}^T C_\eta^{-1} \vec{\epsilon})$ will produce an χ^2-distribution for N degrees of freedom, let's define the confidence level, CL, as:

$$CL := \int_{x=\chi^2}^{\infty} f_N(x)\, \mathrm{d}x$$

where $f_N(x)$ is the χ^2 probability density function (PDF) with N degrees of freedom. For a kinematic fit, $N = n_{\text{constraints}} - n_{\text{unmeas.}}$. The fit is said to be an NC-fit.

Characteristics

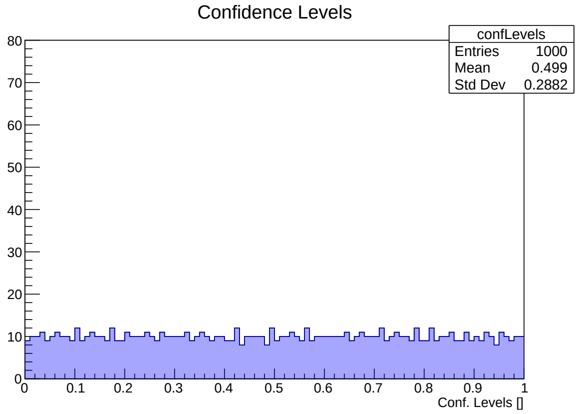

Figure 8.1: Sample of confidence level distribution with no background. Events selected are highlighted in blue.

Since this is the complement of a cumulative distribution function (CDF), we can expect it to have certain characteristics:

- If there is no background in the fit, the distribution is uniform/flat (See **Fig. 8.1**).
- In the presence of background, which need not follow a χ^2-distribution, there will be a sharp rise as $CL \rightarrow 0$, corresponding to large calculated χ^2 (See **Fig. 8.2a**).

Cutting out the sharp rise as $CL \rightarrow 0$ will cut out the much of the background while keeping much of the signal intact (See **Fig. 8.2b**). This is the confidence level cut (CLC).

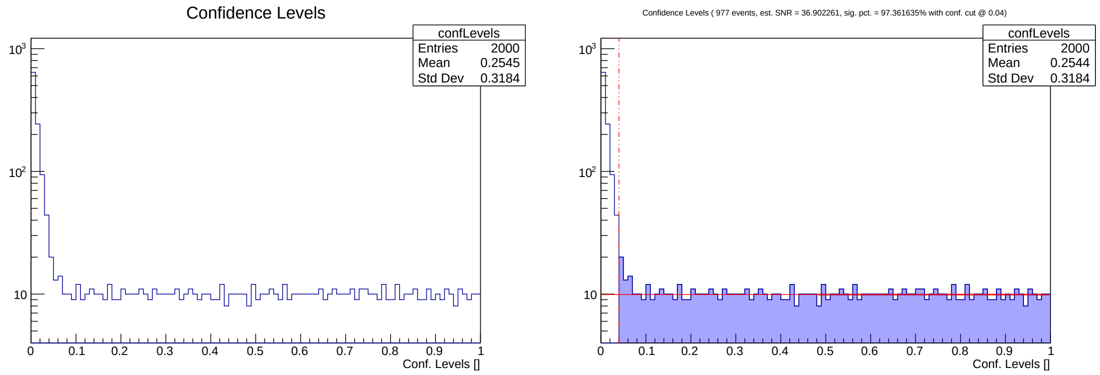

(a) Confidence level distribution with pure signal and background

(b) Confidence level distributions with confidence level cut. Events selected are highlighted in blue.

Figure 8.2: Confidence level distributions before (left) and after (right) CLC.

8.3.2 Pull Distributions

Background can creep in with low χ^2 since background need not follow any particular distribution. To protect against this, pulls are also calculated and their distributions are observed. Additionally, the pull distributions after the CLC gives insight into whether the covariance matrix is correctly taking into account all pairwise correlations between the variables.

Let's introduce $\vec{z}$ to house the pulls, z_i, defined as

$$z_i := \frac{\epsilon_i}{\sigma_{\epsilon_i}} = \frac{y_i - \eta_i}{\sqrt{\sigma_{y_i}^2 - \sigma_{\eta_i}^2}}$$

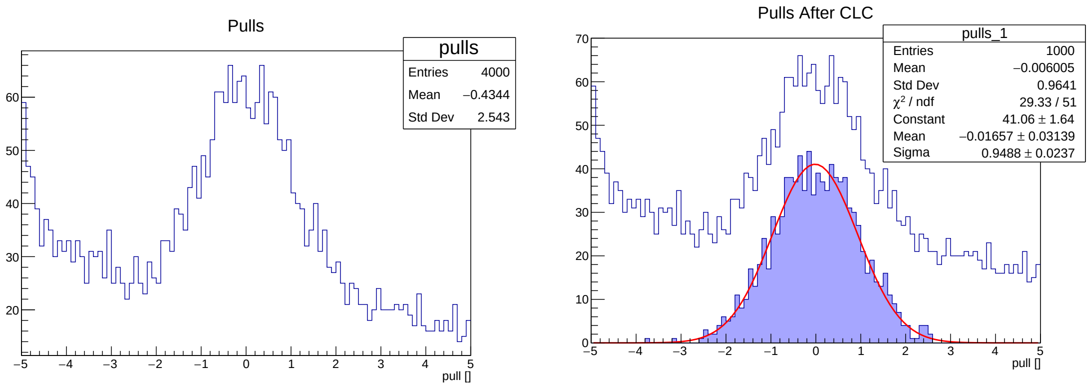

(a) Pull distribution of all events.

(b) Pull distribution after confidence level cut (highlighted in blue).

Figure 8.3: Pull distribution before (left) and and after (right) confidence level cut.

Characteristics

Since these are normalized differences, the distributions should be normally distributed and have:

- Mean: 0
- Width: 1

All of these characteristics are exhibited in **Fig. 8.3b**, the pull distribution for a single measured variable, where the blue highlighted distribution are the events selected from the confidence level cut.

Now that kinematic fitting is defined and its characteristics are laid out, we can now mold a kinematic fit appropriate for exclusive processes the EG6 experiment seeks to study.

VI. Kinematic Fitting Applied to EG6

9. Assembling Inputs for Covariance Matrix

The most nontrivial aspect of kinematic fitting is finding the correct covariance matrix to capture the errors and correlations between fitted variables. This will be tackled first.

To construct a representative covariance matrix, a thorough understanding of the errors, widths, and resolutions of the measurements is absolutely required.

Since the goal is to study exclusive coherent production of π^0 off ^{4}He, and to check DVCS, the only resolutions that are relevant are ones involving the scattered electron, the recoiled helium, and any detected photons. Resolutions were studied at nominal values [12] and simulation studies showed that these resolutions needed to be scaled. **Table 9.8** has the scaling factors needed to match these resolutions.

9.1 Errors and Widths

Let $\oplus$ denote the square-root quadrature sum. That is,

$$a \oplus b \oplus c \oplus \ldots := \sqrt{a^2 + b^2 + c^2 + \ldots}$$

Then with these resolutions, we can calculate the widths that were extracted from simulation particle-by-particle. The explicit forms of the widths are shown in the following subsections. For the following, all input momenta are in GeV$/c$, all input angles are in units denoted by the subscripts, and resolutions are in units given by **Table 9.8**.

9.1.1 Electron (DC)

Table 9.1: Parameters for DC p widths

Parameter **[Units]**	SF_{p1} []	SF_{p2} []	A_p [deg.]	B_p [ ]	C_p [A]	D_p [A]	E_p [1/GeV]	F_p [ ]
Value	3.4	1.5	35	0.7	3375	2099	0.0033	0.0018

Table 9.2: Parameters for DC angle widths

Parameter **[Units]**	**Index** i []	SF_i []	A_i [rad]	B_i [GeV · rad]
Value	θ	2.5	0.55/1000	1.39/1000
	ϕ	4.0	3.73/1000	3.14/1000

The DC widths obtained from simulation studies are

$$\begin{aligned} \sigma_{p_e}[\text{GeV}] &= p\left(\frac{SF_{p1}}{SF_{p2}}\right)\left(\frac{\theta_{\text{deg.}}}{A_p}\right)^{B_p}\left(\frac{C_p}{D_p}\right)\left[\left(E_p p\right)\oplus\frac{F_p}{\beta}\right] \\ \sigma_{\theta_e}[\text{rad}] &= SF_\theta\left[A_\theta\oplus\frac{B_\theta}{p\beta}\right] \\ \sigma_{\phi_e}[\text{rad}] &= SF_\phi\left[A_\phi\oplus\frac{B_\phi}{p\beta}\right] \end{aligned} \tag{9.1}$$

where

- β is the normalized velocity ($\beta := pc/E$),
- SF_i are the scaling factors used to scale up the resolutions extracted from simulation to better match experiment, and
- the parameters A_i through F_i, which account for contributions coming from measurement errors as well as multiple scattering [12], are listed in **Table 9.1** and **Table 9.2** above.

9.1.2 Photon (IC)

Table 9.3: Resolutions for IC

	δx (cm)
IC (Photon)	1.20

Table 9.4: Parameters used to characterize IC momentum width

Parameter [Units]	SF_E []	A_E []	B_E $\left[\sqrt{\text{GeV}/c}\right]$	C_E [GeV/c]
Value	1.33	0.024	0.033	0.019

Table 9.5: Parameters used to characterize IC angle widths

Parameter [Units]	**Index** i []	A_i $[\sqrt{\text{GeV}/c}]$	B_i [1/rad cm]
Value	θ	0.003	0.013
	ϕ	0.003	–

- -

The IC widths are

$$\begin{aligned}\sigma_{p_\gamma}[\text{GeV}] &= p\,(SF_E)\left[A_E \oplus \frac{B_E}{\sqrt{p}} \oplus \frac{C_E}{p}\right]\\ \sigma_{\theta_\gamma}[\text{rad}] &= \delta x\left[\frac{A_\theta}{\sqrt{p}} \oplus (B_\theta \theta_{\text{rad.}})\right]\\ \sigma_{\phi_\gamma}[\text{rad}] &= \delta x\left[\frac{A_\phi}{\sqrt{p}}\right]\end{aligned} \tag{9.1}$$

where the parameters A_i through C_i are listed in **Table 9.4** and **Table 9.5** above.

9.1.3 Photon (EC)

Table 9.6: Resolutions for EC

	$\boldsymbol{\delta\theta}$ (rad.)	$\boldsymbol{\delta\phi}$ (rad.)
EC (Photon)	0.004	0.004

Table 9.7: Parameter used to characterize EC momentum width

Parameter	$\boldsymbol{A_p}$ [$\sqrt{\text{GeV}/c}$]
Value	0.116

The EC widths are

$$\begin{aligned} \sigma_{p_\gamma}[\text{GeV}] &= A_p\sqrt{p} \\ \sigma_{\theta_\gamma}[\text{rad}] &= \delta\theta_{EC} \\ \sigma_{\phi_\gamma}[\text{rad}] &= \delta\phi_{EC} \end{aligned} \tag{9.1}$$

9.1.4 Helium (RTPC)

Table 9.8: Resolutions for RTPC

	$\boldsymbol{\delta p/p}$ (%)	$\boldsymbol{\delta\theta}$ (deg.)	$\boldsymbol{\delta\phi}$ (deg.)
RTPC (Helium)	10.00	4.00	4.00

A complete study of the RTPC errors has not yet been done so they are independent of the kinematics, taking fixed values of the resolutions:

$$\begin{aligned} \sigma_{p_{^4\text{He}}}[\text{GeV}] &= p\,(\delta p/p) \\ \sigma_{\theta_{^4\text{He}}}[\text{rad}] &= \delta\theta_{\text{rad}} \\ \sigma_{\phi_{^4\text{He}}}[\text{rad}] &= \delta\phi_{\text{rad}} \end{aligned} \tag{9.1}$$

VII. Verification of Coherent DVCS in CLAS EG6

To see how kinematic fitting as an event selection method compares to exclusivity cuts, kinematic fitting is first applied to previously studied [4, 15]the coherent DVCS reaction [3]:

$$e\ ^4\text{He} \rightarrow e'\ ^4\text{He}'\ \gamma \quad .$$

In addition to this previous analysis being published, some benefits are that it has higher statistics and only 3 final state particles that need to conserve energy and momentum.

10. $4C$-fit on DVCS

With the procedure outlined and a way to measure the quality of the fit, we can apply it to experimental data and/or simulation. For now, kinematic fitting is used to select events. These events passing a kinematic fit will be compared to events passing exclusivity cuts outlined in **Chapter IV.**.

The following kinematic fitting is a $4C$-fit, using the conservation of momentum and energy in an exclusive process as the constraints. The fitting is applied to momentum vectors of the final state particles in the exclusive process:

$$e^4\text{He} \rightarrow e'^4\text{He}'\gamma \quad .$$

That is, since all particles of this process are measured in CLAS EG6, with the help of the RTPC and IC, there are no unmeasured variables. The measured variables for the fit will be $\bigcup\limits_{\beta}\left\{p_\beta, \theta_\beta, \phi_\beta\right\}$, where β loops over all final state particles.

---

[3] In order to do a fair comparison, the particle identification and exclusivity cuts follow exactly as outlined in [4] for this chapter.

10.1 Setting Up Inputs

10.1.1 Covariance Matrix

A simple 9×9 covariance matrix with correlations embedded in the variances (See **Section 9.1**) along the diagonal and zeros elsewhere is used:

$$C_\eta = \mathrm{diag}\left(\sigma^2_{p_e}, \sigma^2_{\theta_e}, \sigma^2_{\phi_e}, \sigma^2_{p_{^4\mathrm{He}}}, \sigma^2_{\theta_{^4\mathrm{He}}}, \sigma^2_{\phi_{^4\mathrm{He}}}, \sigma^2_{p_\gamma}, \sigma^2_{\theta_\gamma}, \sigma^2_{\phi_\gamma}\right) = \begin{bmatrix} \sigma^2_{p_e} & 0 & \dots & \dots & \dots & 0 \\ 0 & \sigma^2_{\theta_e} & \ddots & \ddots & \ddots & \vdots \\ \vdots & \ddots & \ddots & \ddots & \ddots & \vdots \\ \vdots & \ddots & \ddots & \ddots & \ddots & \vdots \\ \vdots & \ddots & \ddots & \ddots & \sigma^2_{\theta_\gamma} & 0 \\ 0 & \dots & \dots & \dots & 0 & \sigma^2_{\phi_\gamma} \end{bmatrix}.$$

Contrary to its appearance, it is important to note that the covariance matrix is constructed event by event, since the widths are functions of the p, θ, and ϕ of each measured particle.

10.1.2 Input Kinematic Vectors

Before constructing our input vectors for the kinematic fit, it would be convenient to introduce some 4-momenta:

$$P_{\mathrm{init}} := P_e + P_{^4\mathrm{He}}$$

$$P_{\mathrm{fin}} := P_{e'} + P_{^4\mathrm{He}'} + P_\gamma$$

Then

$$P_{\mathrm{Exc}} := P_{\mathrm{init}} - P_{\mathrm{fin}} \tag{10.1}$$

houses our 4 constraint equations for exclusivity, since all components of this vector should be zero.

Now, since there are no unmeasured vectors and all measurements in input vectors are final state particles, let's omit the primes (′). The input vectors are then:

$$\vec{y_0} = \vec{\eta} = \begin{bmatrix} p_e \\ \theta_e \\ \phi_e \\ p_{^4\mathrm{He}} \\ \theta_{^4\mathrm{He}} \\ \phi_{^4\mathrm{He}} \\ p_\gamma \\ \theta_\gamma \\ \phi_\gamma \end{bmatrix} \qquad \vec{c} = \begin{bmatrix} (P_{\mathrm{Exc}})_x \\ (P_{\mathrm{Exc}})_y \\ (P_{\mathrm{Exc}})_z \\ (P_{\mathrm{Exc}})_E \end{bmatrix} .$$

10.1.3 Input Kinematic Matrices

In this $4C$-fit, there are no unmeasured variables so B is the only input matrix:

$$B = \begin{bmatrix} \frac{\partial c_1}{\partial \eta_1} & \cdots & \frac{\partial c_1}{\partial \eta_9} \\ \vdots & \ddots & \vdots \\ \frac{\partial c_4}{\partial \eta_1} & \cdots & \frac{\partial c_4}{\partial \eta_9} \end{bmatrix}$$

To see the matrix explicitly, introduce D_β:

$$D_\beta := \begin{bmatrix} -\sin\theta_\beta\cos\phi_\beta & -p_\beta\cos\theta_\beta\cos\phi_\beta & p_\beta\sin\theta_\beta\sin\phi_\beta \\ -\sin\theta_\beta\sin\phi_\beta & -p_\beta\cos\theta_\beta\sin\phi_\beta & -p_\beta\sin\theta_\beta\cos\phi_\beta \\ -\cos\theta_\beta & p_\beta\sin\theta_\beta & 0 \\ -\frac{p_\beta}{E_\beta} & 0 & 0 \end{bmatrix} \tag{10.1}$$

where β is a placeholder for a particle. We can now form the 4×9 matrix, B, by concatenating the three 4×3 D_β matrices:

$$B = \begin{bmatrix} D_e & D_{^4\text{He}} & D_\gamma \end{bmatrix}$$

10.2 Fit Outputs

From just these inputs, all other vectors and matrices from **Section 8.2.1** can be constructed and a set of fitted final state momenta can be extracted from the final fitted vector $\vec{y}$.

10.2.1 Confidence Level Distribution

To see how this kinematic fit fared, we look at the confidence level distribution. From **Fig. 10.1**, we see that there is some background from the peak at 0 and a plateau thereafter.

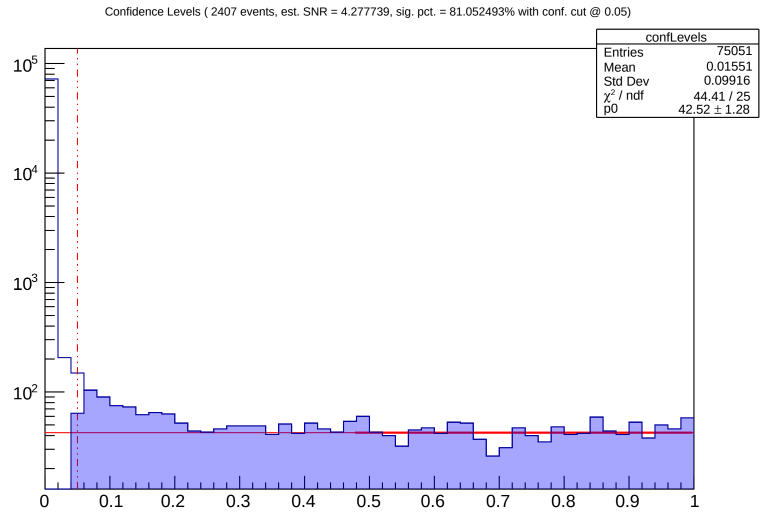

Figure 10.1: Confidence level distribution with a cut at 0.05, represented by the red vertical dashed line. The events passing the cut are represented by the light blue highlighted distribution which the right half is fitted to straight line to estimate the signal to noise ratio.

The plateau in the confidence level distribution signifies that there is an underlying distribution that follows our hypothesis that the particles involved are part of an exclusive process, conserving momentum and energy. Otherwise, the calculated χ^2 would not be coming from a χ^2-distribution and the resulting confidence level distribution would not look uniform at any point (See **Section 8.3.1** and [5]). Note that this is the only user-based cut in the entire event selection process.

10.2.2 Pull Distributions

To see how well the confidence level cut does, we look to the pull distributions. If we see each pull normally distributed with a width of 1 and a mean of 0, the quality of the fit along with the confidence level cut are satisfactory. From **Fig. 10.2**, the pull distributions look reasonable. At the very least, the distributions resemble the red curves they ought to be qualitatively.

The pull distributions tell us that although the covariance matrix is diagonal, correlations are reasonably accounted for: the variances along the diagonal have the pair-wise correlations between a particle's p, θ, ϕ embedded in them (See **Eqs. 9.1, 9.1, 9.1**). Additionally, the confidence level cut is rejecting most of the background (events that do not conserve momentum and energy of an exclusive process within detectors' errors).

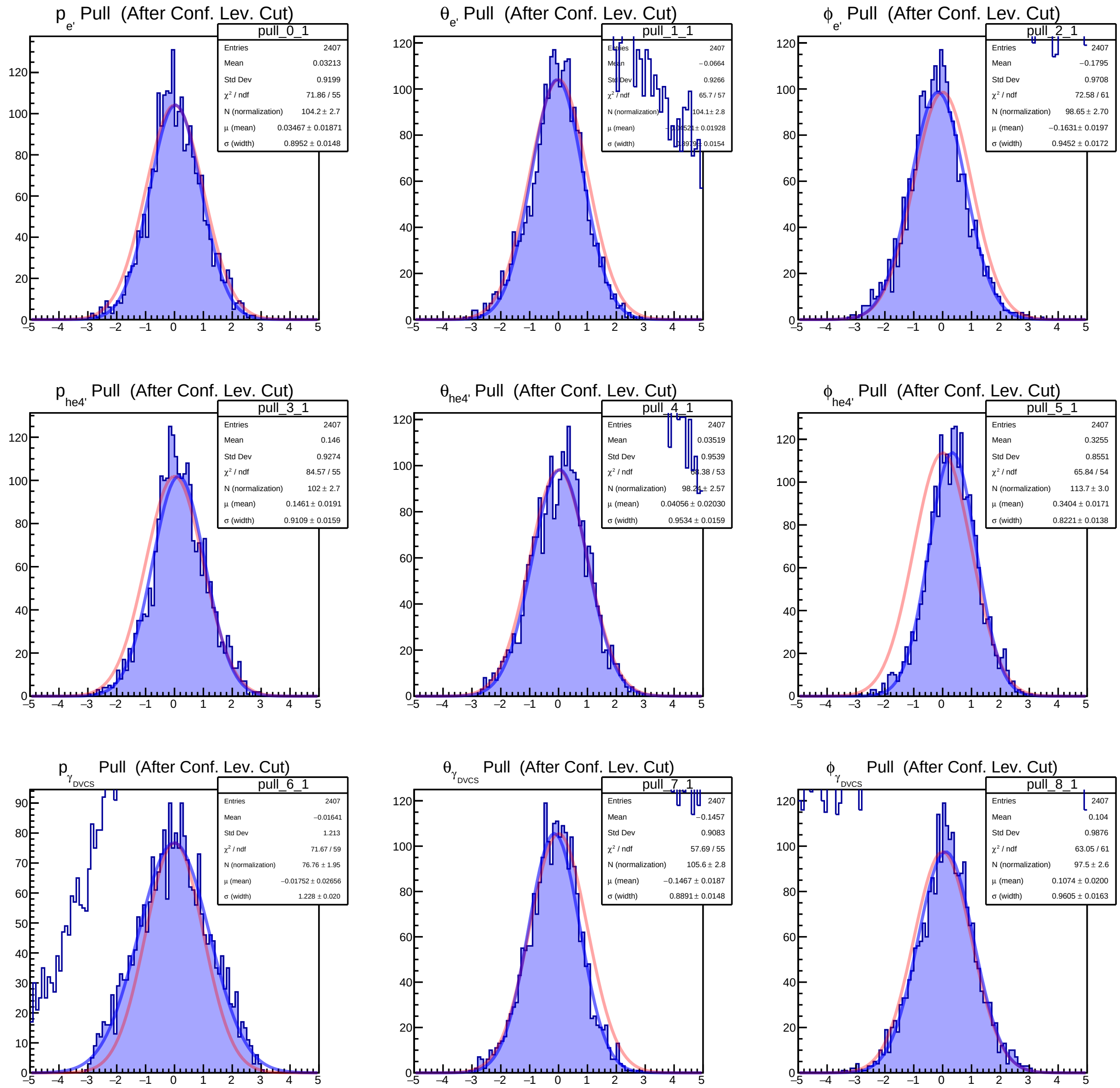

Figure 10.2: Pull distributions. From left to right we have p, θ, ϕ of the, from top to bottom, particles $e, {}^4\mathrm{He}, \gamma$. The blue curve is a gaussian fit to the distribution. The red curve is just a visual aid of what the distribution should be: a gaussian normalized to the blue curve with width 1, centered at 0.

10.3 Fit Results

The quality of the fit as shown in the previous section, **Section 10.2**, shows that the fit is satisfactory for the confidence level cut. The next subsections will show the resulting measured (in blue) and fitted (shaded green) distributions and asymmetries, as compared to the ones in the previous study [15] (in red).

10.3.1 Exclusivity Variable Distributions

The confidence and pull distributions show that it was a good fit but what do the selected events look like? The exclusivity variable distributions show how well the events selected conserve momentum and energy. Ideally, the exclusivity variable distributions will all be δ-function distributions centered at the expected values discussed in **Chapter IV.**. Detector resolutions naturally smear these distributions and background events dilute the signal. The goal is to get at the underlying signal.

The events passing the exclusivity cuts (red distributions in **Fig. 10.3**) are obtained with a 3σ cut on the values defined in **Table 10.1** which summarizes the previous analysis [4].

Table 10.1: Coherent DVCS Exclusivity Cut Values [4]

Variable	Mean (μ)	Width (σ)	Units
$M^2_{X_0}$	1.40066e+01	1.85929e+00	$(\mathrm{GeV}/c^2)^2$
$M^2_{X_1}$	−1.72013e−02	2.33988e−01	$(\mathrm{GeV}/c^2)^2$
$M^2_{X_2}$	−2.96869e−03	9.10158e−03	$(\mathrm{GeV}/c^2)^2$
px_{X_2}	−2.32102e−03	4.52945e−02	GeV/c
py_{X_2}	−8.97351e−04	3.89937e−02	GeV/c
pt_{X_2}	4.14664e−02	4.24914e−02	GeV/c
E_{X_2}	1.56814e−02	2.51492e−01	GeV
θ	5.08070e−01	4.74883e−01	deg.
$\Delta\phi$	1.79405e−01	4.53791e−01	deg.

With kinematic fitting described in this section, a single cut shapes all of these distributions: the confidence level cut. **Fig. 10.3** shows a comparison between the measured events obtained from exclusivity cuts (in red) and the kinematic fit (in blue); and the fitted events from the kinematic fit (in green).

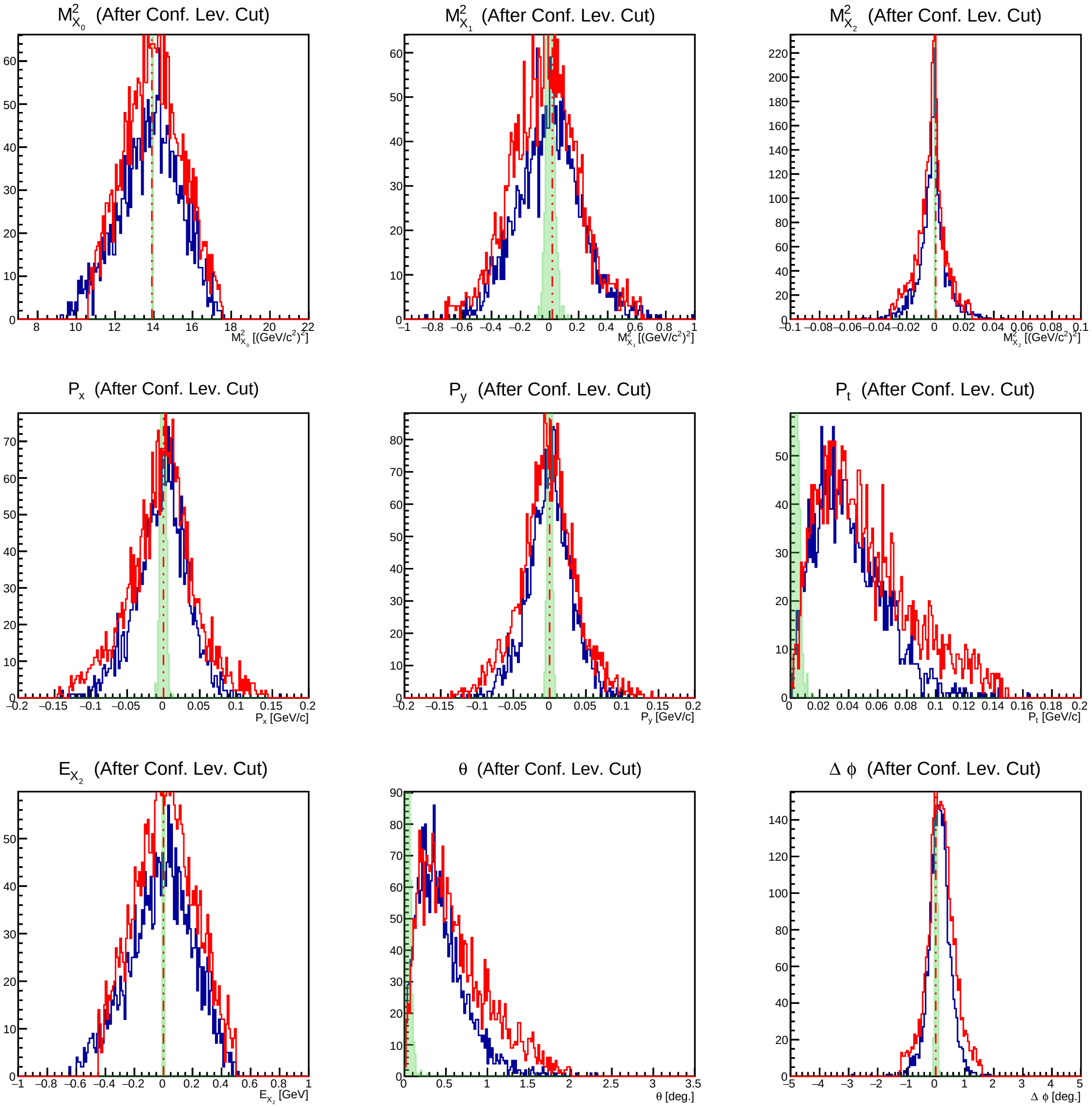

Figure 10.3: Exclusivity variable distributions for:
- Measured events passing exclusivity cuts (red)
- Measured events passing kinematic fit with 0.05 conf. level cut (blue)
- Fitted events passing kinematic fit with 0.05 conf. level cut (highlighted green)

The measured exclusivity variable distributions are very similar with the exception that the tails from the events passing the kinematic fit are suppressed. The measured events passing the CLC are used to extract the beam spin asymmetry.

10.3.2 Beam Spin Asymmetry

The raw[4] beam spin asymmetry are shown in **Fig. 10.4**. Following from the fact that the exclusivity variable distributions do not look too disimilar between events selected through exclusivity cuts and kinematic fitting, nothing sticks out in the raw asymmetries.

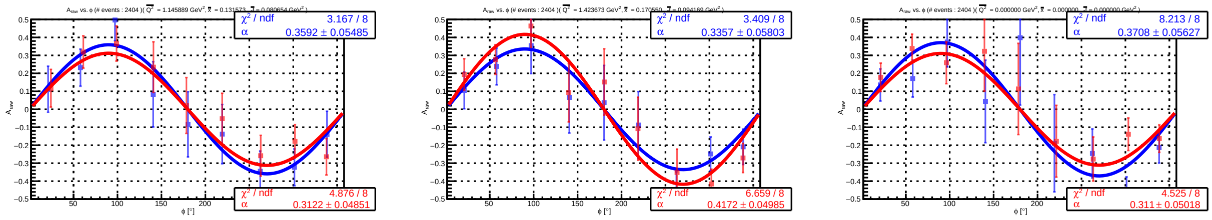

(a) Raw beam spin asymmetries in Q^2 bins with edges $\{1.00, 1.28, 1.58, 5.00\}$ $(\mathrm{GeV}/c^2)^2$, integrated over all $x, -t$ bins.

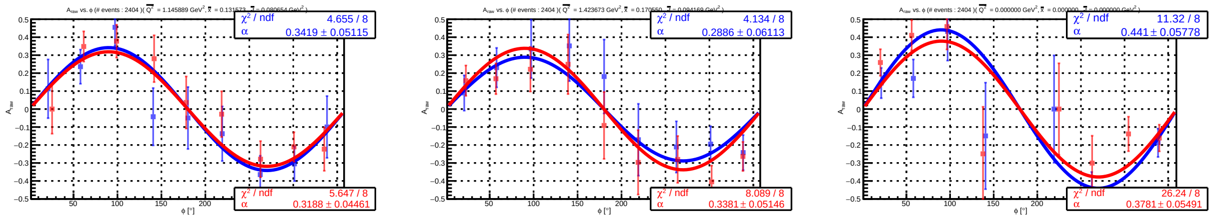

(b) Raw beam spin asymmetries in x bins with edges $\{0.000, 0.152, 0.190, 0.500\}$, integrated over all $Q^2, -t$ bins.

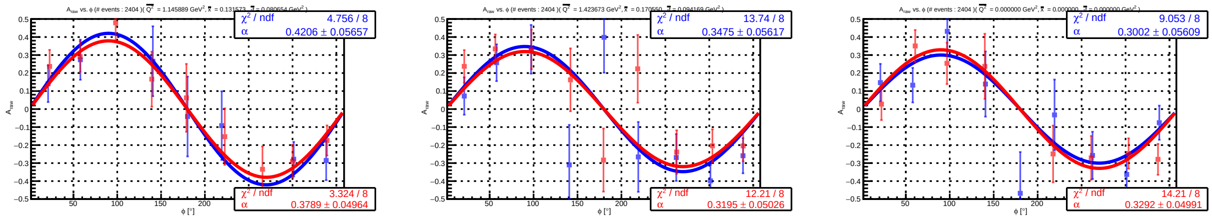

(c) Raw beam spin asymmetries in $-t$ bins (with edges $\{0.065, 0.087, 0.103, 1.000\}$) $(\mathrm{GeV}/c^2)^2$, integrated over all Q^2, x bins.

Figure 10.4: Raw beam spin asymmetry (**Figs. 10.4a, 10.4b, 10.4c**) for:
- Measured events passing exclusivity cuts (red)
- Measured events passing kinematic fit with 0.05 conf. level cut (blue)

Here we have validated the kinematic fitting as an event selection tool: it has selected similar events, and thus extracted similar beam spin asymmetries in all bins with the same binning scheme as in the previous analysis [4] where event selection was done with exclusivity cuts instead.

---

[4] purely statistical: no particular background subtraction or dilution studies applied

VIII. Looking into Coherent DVπ^0P

The kinematic fitting on DVCS events produced similar events to that which was done with exclusivity cuts, in turn producing similar beam spin asymmetries. This gives confidence into applying it to a much rarer process, coherent electroproduction of π^0 off ^{4}He.

First before going into the kinematic fit, we will again outline what was done previously to select events: exclusivity cuts and a few additional cleaning cuts [1].

Then, a $4C$-kinematic fit, using the conservation of momentum and energy in an exclusive process as the constraints, is outlined. The fitting is applied to momentum vectors of the final state particles in the exclusive process:

$$e\,{}^4\mathrm{He} \to e'\,{}^4\mathrm{He}'\pi^0 \to e'\,{}^4\mathrm{He}'\gamma\gamma \quad .$$

That is, the measured variables for the fit will be $\bigcup_\beta \left\{p_\beta, \theta_\beta, \phi_\beta\right\}$, where β loops over all final state particles: $e', {}^4\mathrm{He}', \gamma_1, \gamma_2$.

Finally, a $5C$-kinematic fit, which includes the $4C$-fit along with the constraints of the π^0-decay simultaneously, is outlined.

11. Cuts Applied to EG6

11.1 Exclusivity Cuts

Table 11.1 outlines the means (μ), widths (σ), mins, and maxes of the exclusivity cuts used in the previous analysis [1]. A 3σ and θ cut is applied to all events.

Table 11.1: Coherent DVπ^0P Cut Values [1]

Variable	**Mean (μ)**	**Width (σ)**	**Units**
$M^2_{X_0}$	1.4079e+01	1.138e+00	$(\mathrm{GeV}/c^2)^2$
$M^2_{X_2}$	−0.0050e+00	0.016e+00	$(\mathrm{GeV}/c^2)^2$
$\Delta\phi$	1.4000e−01	0.460e+00	deg.
	Min.	**Max.**	**Units**
θ	0.0	2.5	deg.

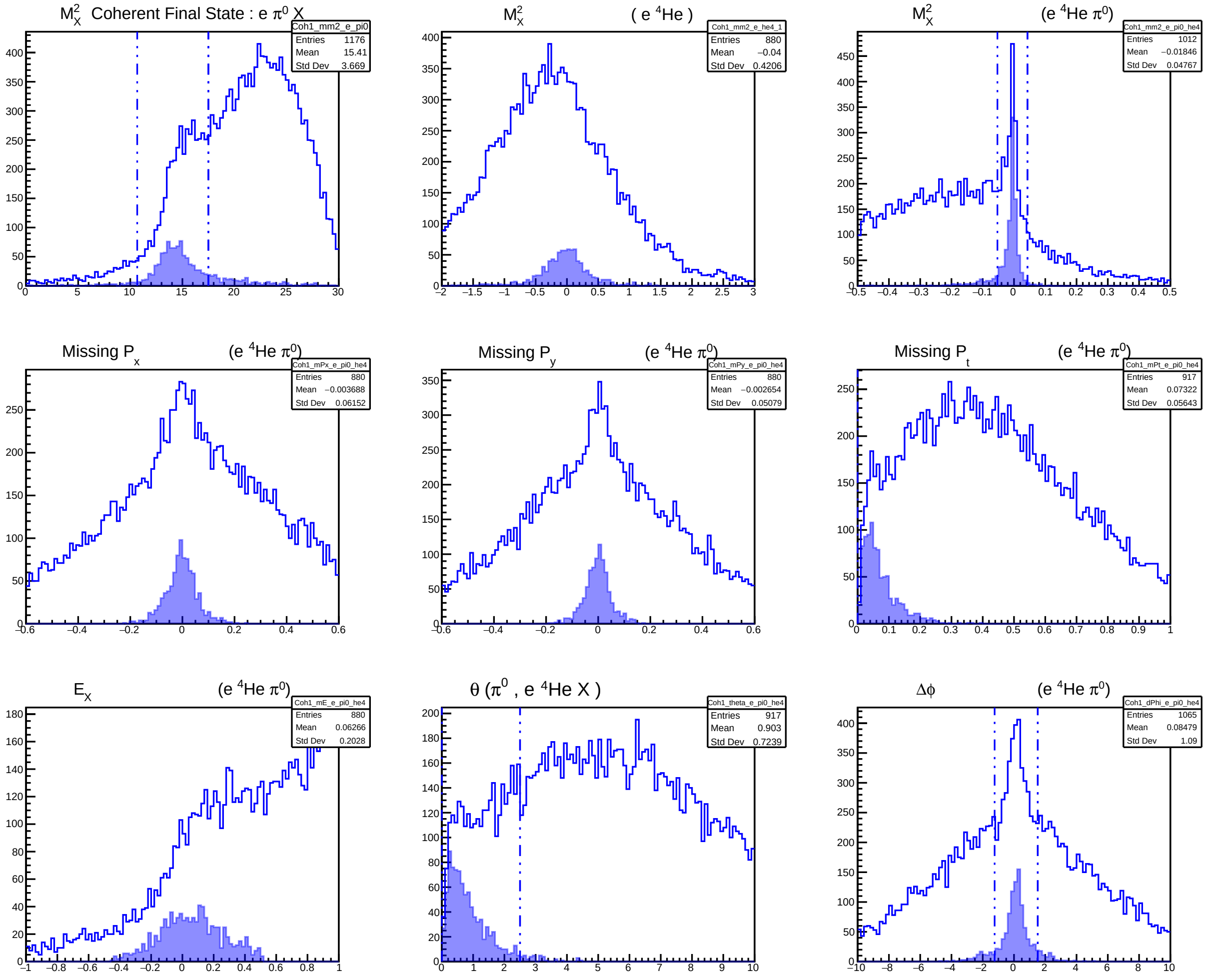

Figure 11.1: Exclusivity cuts on 4 variables shown with dashed vertical lines. The events passing all other cuts except for its own cut are highlighted in light blue. All other events detecting an electron, helium-4, and two photons is the unshaded histogram.

11.2 Additional Photon and Photon Pair Cuts

To compare event selection methods between previous work and this work, involving kinematic fitting, additional cuts [1] were applied to the exclusivity cuts. These cuts involve photon pairs and were made in an effort to help clean the signal. Since we are looking for π^0's, an invariant mass cut of two photons of 3σ (see **Table 11.2**) is applied to all events. Additionally, cuts were made to characterize the produced π^0 in the given kinematics, listed in **Table 11.2**.

Table 11.2: Photon and Photon Pair Cuts

	Mean (μ)	**Width (σ)**	**Units**
$M_{\gamma\gamma}$	0.134	0.01	GeV/c^2
	Min.	**Max.**	**Units**
$\Delta X_{\gamma_1,\gamma_2}$	3.00	7.00	cm
p_{π^0}	3.00	—	GeV/c
p_{γ_2}	0.40	—	GeV/c

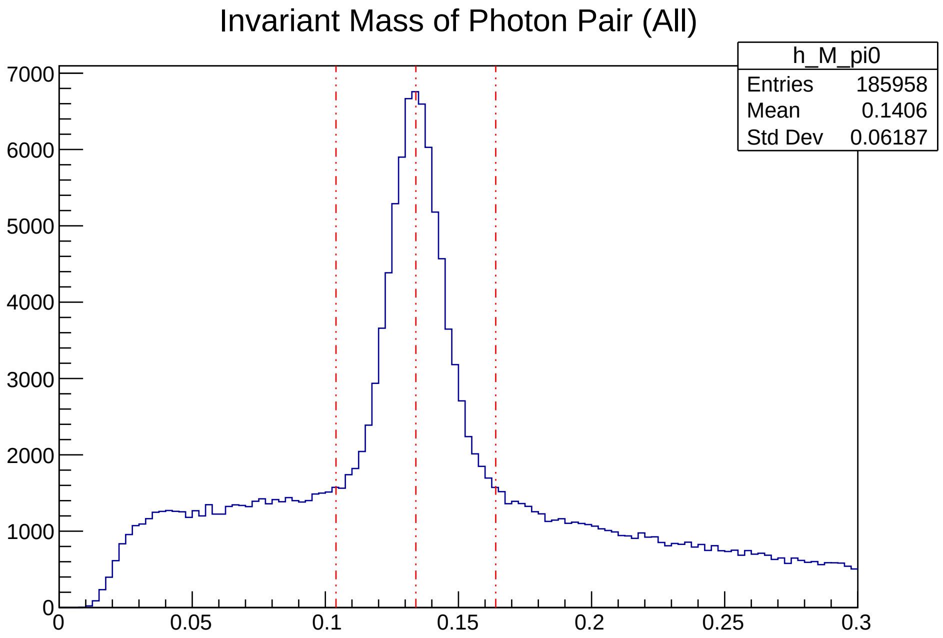

Figure 11.2: The invariant mass distribution of two photons in the IC. The central vertical dashed line is the nominal value and the ones to the left and right are the ±3σ cut values.

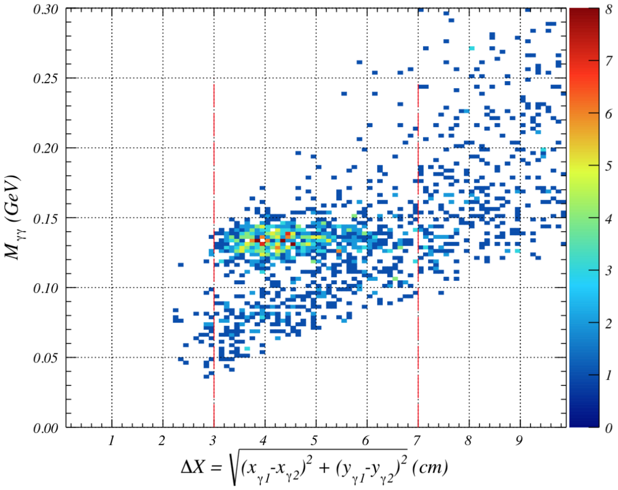

Figure 11.3: A cut on the distance between the photons is applied [1].

Here,

- $\Delta X_{\gamma_1,\gamma_2}$ is the distance between the two photons on the face of the IC (**Fig. 11.3**).
- p_{π^0} is the momentum magnitude of the π^0 formed from the two photons (**Fig. 11.4a**).
- p_{γ_2} is the momentum magnitude of the lower energy photon (**Fig. 11.4b**).

Events passing all of these cuts are taken to be coherent DVπ^0P events. These events will be used to extract a beam spin asymmetry.

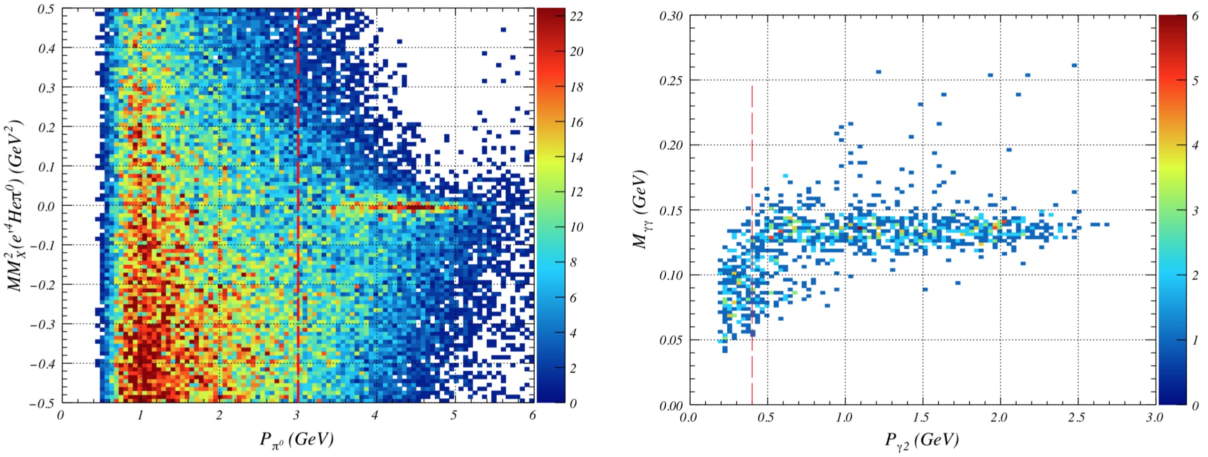

(**a**) Minimum π^0 momenum cut [1].

(**b**) Minimum photon momentum cut [1].

Figure 11.4: Minimum π^0 (**a**) and photon (**b**) momentum cuts [1].

12. $4C$-fit on DVπ^0P

As alternative, let's look at the completely independent event selection method: $4C$-kinematic fitting. Then a comparison between the two parallel methods can be made.

12.1 Setting Up Inputs

12.1.1 Covariance Matrix

The kinematic fit applied on DVCS seemed to work quite well so the same event by event covariance matrix is constructed:

$$C_\eta = \mathrm{diag}\left(\sigma^2_{p_e}, \sigma^2_{\theta_e}, \sigma^2_{\phi_e}, \sigma^2_{p_{^4\mathrm{He}}}, \sigma^2_{\theta_{^4\mathrm{He}}}, \sigma^2_{\phi_{^4\mathrm{He}}}, \sigma^2_{p_{\gamma 1}}, \sigma^2_{\theta_{\gamma 1}}, \sigma^2_{\phi_{\gamma 1}}, \sigma^2_{p_{\gamma 2}}, \sigma^2_{\theta_{\gamma 2}}, \sigma^2_{\phi_{\gamma 2}}\right)$$

12.1.2 Input Kinematic Vectors and Matrices

Again let's introduce some 4-momenta for convenience:

$$P_{\mathrm{init}} := P_e + P_{^4\mathrm{He}}$$

$$P_{\mathrm{fin}} := P_{e'} + P_{^4\mathrm{He}'} + P_{\gamma_1} + P_{\gamma_2}$$

Then

$$P_{\mathrm{Exc}} := P_{\mathrm{init}} - P_{\mathrm{fin}} \tag{12.1}$$

will hold our constraints.

Omitting the primes(’), the input kinematic vectors and matrix are:

$$\vec{y_0} = \vec{\eta} = \begin{bmatrix} p_e \\ \theta_e \\ \phi_e \\ p_{^4\mathrm{He}} \\ \theta_{^4\mathrm{He}} \\ \phi_{^4\mathrm{He}} \\ p_{\gamma_1} \\ \theta_{\gamma_1} \\ \phi_{\gamma_1} \\ p_{\gamma_2} \\ \theta_{\gamma_2} \\ \phi_{\gamma_2} \end{bmatrix}, \qquad \vec{c} = \begin{bmatrix} (P_{\mathrm{Exc}})_x \\ (P_{\mathrm{Exc}})_y \\ (P_{\mathrm{Exc}})_z \\ (P_{\mathrm{Exc}})_E \end{bmatrix}, \qquad B = \begin{bmatrix} \frac{\partial c_1}{\partial \eta_1} & \cdots & \frac{\partial c_1}{\partial \eta_{12}} \\ \vdots & \ddots & \vdots \\ \frac{\partial c_4}{\partial \eta_1} & \cdots & \frac{\partial c_4}{\partial \eta_{12}} \end{bmatrix}$$

with no unmeasured inputs.

Explicitly,

$$B = \begin{bmatrix} D_e & D_{^4\mathrm{He}} & D_{\gamma_1} & D_{\gamma_2} \end{bmatrix}$$

where D_β is defined in **Eq. 10.1**.

12.2 Fit Outputs

12.2.1 Confidence Level Distribution

The 4*C*-fit produces a confidence level distribution seen in **Fig.** 12.1. A CLC is made at 0.05.

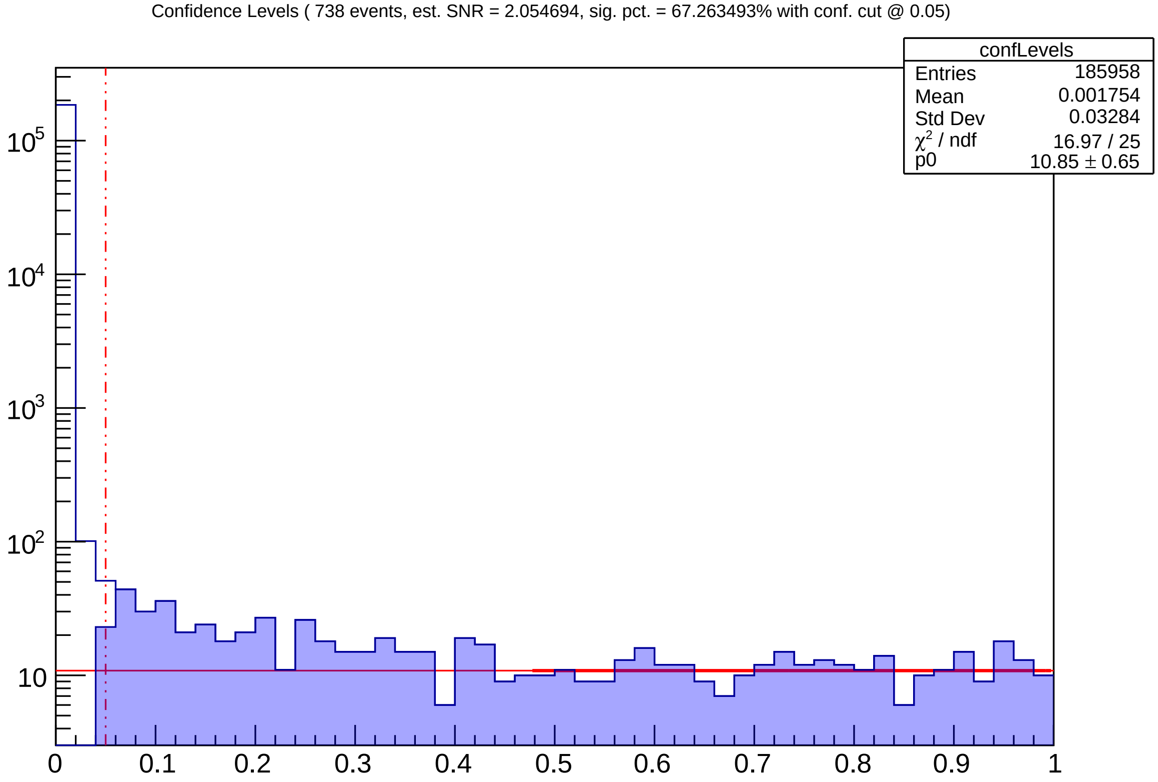

Figure 12.1: Confidence level distribution with a cut at 0.05, represented by the red vertical dashed line. The events passing the cut are represented by the blue highlighted distribution which the right half is fitted to straight line to estimate the signal to noise ratio.

12.2.2 Pull Distributions

The kinematic fit with the CLC produces the pull distributions in **Fig.** 12.2. These pull distributions too look reasonable.

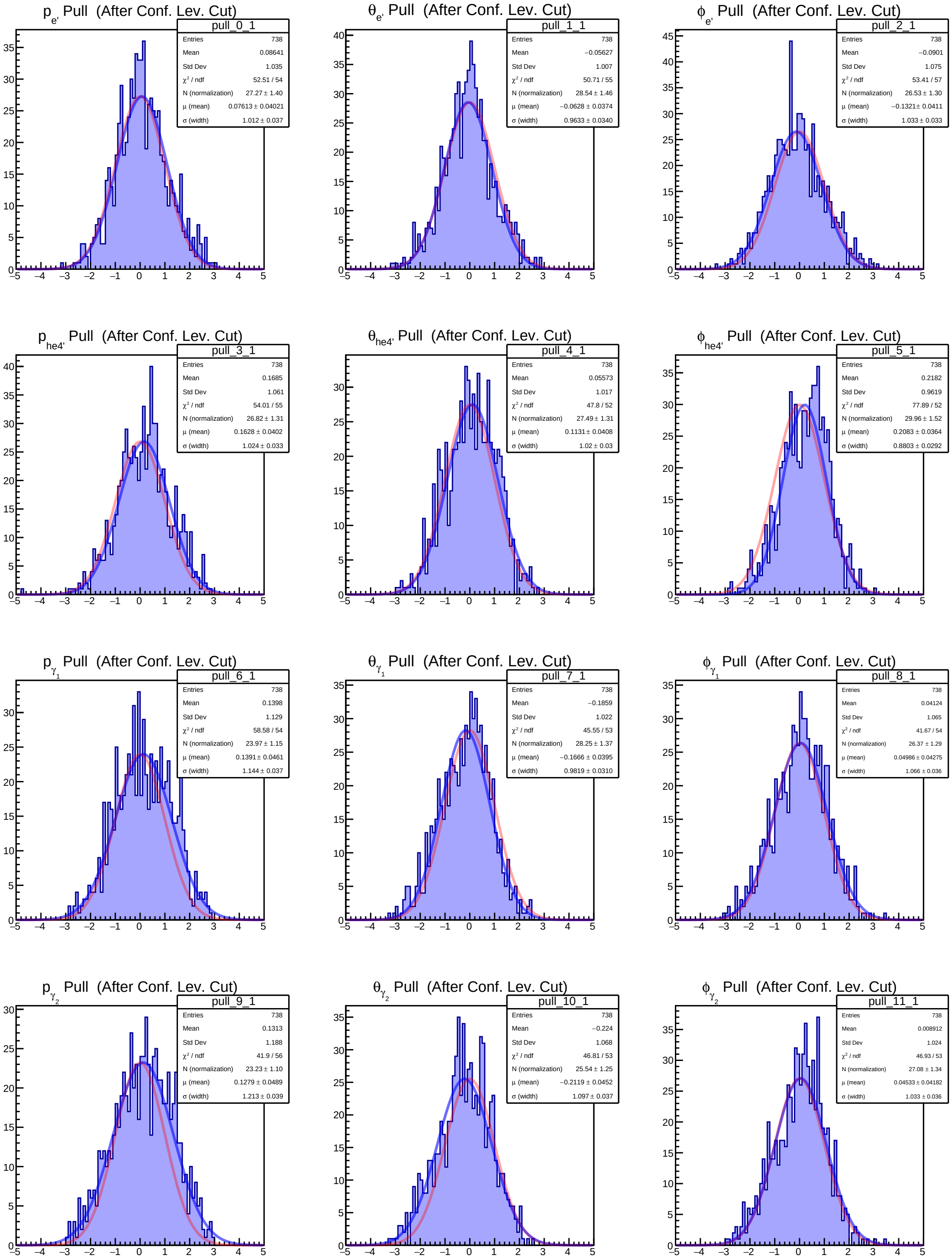

Figure 12.2: Pull distributions. From left to right we have p, θ, ϕ of the, from top to bottom, particles $e, {}^4\text{He}, \gamma_1, \gamma_2$. The blue curve is a gaussian fit to the distribution. The red curve is just a visual aid of what the distribution should be: a standard normal distribution.

12.3 Fit Results

The quality of the fit as shown in the previous section, **Section 12.2**, shows that the fit is satisfactory for the confidence level cut. The next subsections will show the resulting measured (in blue) and fitted (shaded green) distributions and asymmetries, as compared to the ones in the previous study [1] (in black).

12.3.1 Exclusivity Variable Distributions

Along with the invariant mass distribution, the exclusivity variable distributions show the quality of events selected. For the exclusivity cuts in **Section 11.1**, each cut applied shaped all other distributions. With kinematic fitting described in this section, a single cut shapes all of these distributions: the confidence level cut. **Fig. 12.3** shows a comparison between the measured events obtained from exclusivity cuts (in black) and the kinematic fit (in blue); and the fitted events from the kinematic fit (in green).

The measured exclusivity variable distributions are similar but the tails of missing energy, transverse momentum, and θ_{X_1,π^0} distributions are all sizably suppressed.

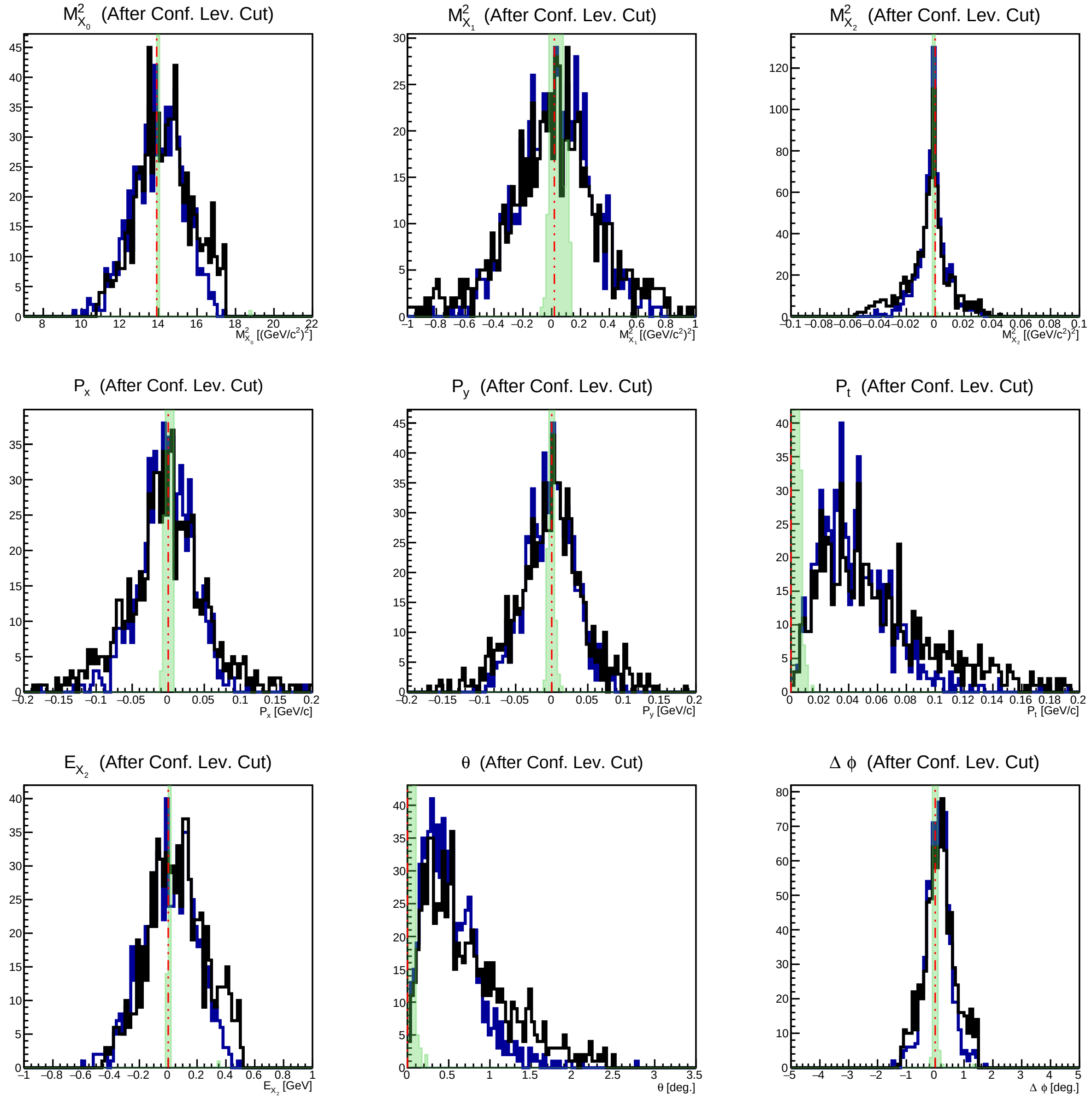

Figure 12.3: Exclusivity variable distributions for:
- Measured events passing exclusivity cuts (black)
- Measured events passing kinematic fit with 0.05 conf. level cut (blue)
- Fitted events passing kinematic fit with 0.05 conf. level cut (highlighted green)

12.3.2 Invariant Mass Distribution

Perhaps what best displays the power of kinematic fitting is the fact that even though invariant mass of the π^0 is nowhere mentioned in the fitting, the invariant mass distribution of the two photons shows a clear peak at the nominal value (see **Fig. 12.4a**). Using measured 4-momenta, the kinematic fit with conservation of momentum and energy for the exclusive process

$$e^4\text{He} \rightarrow e'^4\text{He}'\gamma\gamma$$

is already enough to rule out many of the background photon pairs (as compared to **Fig. 11.2**).

12.3.3 Beam Spin Asymmetry

Although the invariant mass distribution is not entirely clean, it's worth plotting the raw beam spin asymmetry, shown in **Fig. 12.4b**, to see how the background affects the

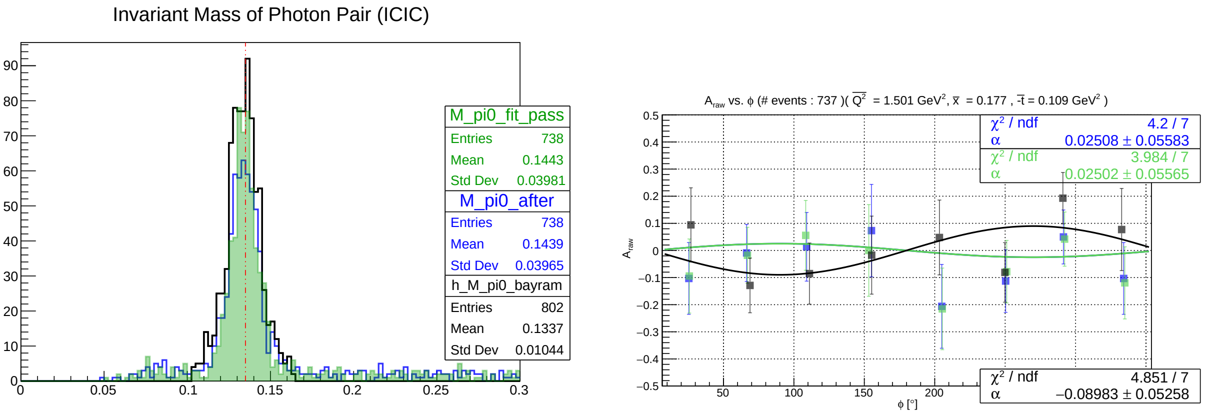

(**a**) Invariant mass distributions of photon pairs

(**b**) Raw beam spin asymmetries integrated over all $Q^2, x, -t$ bins

Figure 12.4: Invariant mass distributions of photon pairs (12.4a) and raw beam spin asymmetry (12.4b) for:
- Measured events passing exclusivity cuts (black)
- Measured events passing kinematic fit with 0.05 conf. level cut (blue)
- Fitted events passing kinematic fit with 0.05 conf. level cut (highlighted green)

asymmetry.

Still, it is clear, by the invariant mass distribution of the photon pair, that the events need to be cleaned. There are two ways to address this. One way will be outlined in the **Section 13.** but the simpler, more obvious one is to cut on the invariant mass distribution.

12.4 Adding π^0 Cut

To clean up the background and to have a better comparison between the exclusivity cuts and the kinemtic fit, the same 3σ invariant mass cut (see **Table 11.2**) is applied to the measured values of the previous section.

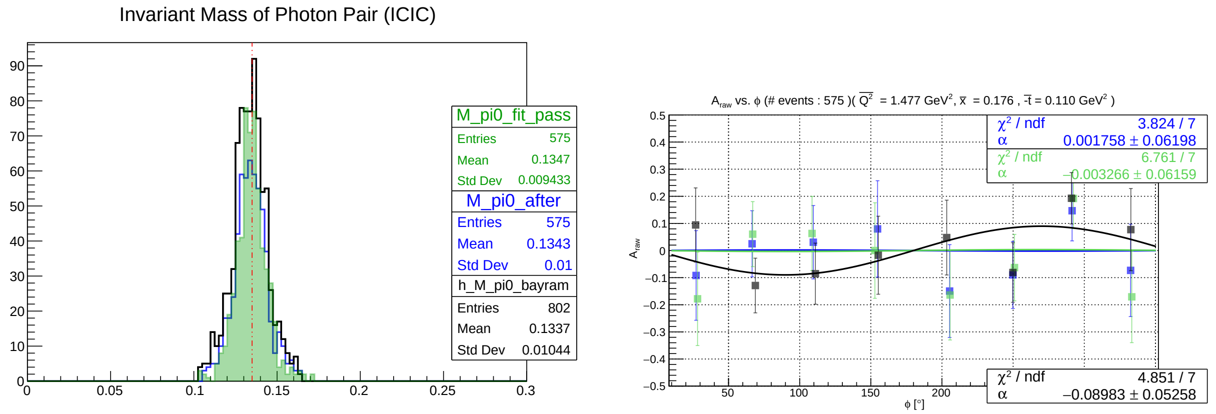

(**a**) Invariant mass distributions of photon pairs with the nominal value indicated by the vertical red line

(**b**) Raw beam spin asymmetries integrated over all $Q^2, x, -t$ bins

Figure 12.5: Invariant mass distributions of photon pairs (12.5a) and raw beam spin asymmetry (12.5b) for:
- Measured events passing exclusivity cuts (black)
- Measured events passing kinematic fit with 0.05 conf. level cut (blue)
- Fitted events passing kinematic fit with 0.05 conf. level cut (highlighted green)

This is one way to clean the events but we can do better, discussed in the next section.

13. 5C-fit on DVπ^0P

Instead of just relying on exclusivity of

$$e\,^4\mathrm{He} \rightarrow e'\,^4\mathrm{He}'\gamma\gamma \quad ,$$

we can fold in that the two photons come from the decay of π^0. That is, we create a 5C-fit, that simulataneously conserves momentum and energy of the two processes:

$$e\,^4\mathrm{He} \rightarrow e'\,^4\mathrm{He}' X_{\pi^0}$$

$$X_{\pi^0} \rightarrow \gamma\gamma$$

Since the momentum of the π^0 is not directly measured but reconstructed from the two photons, there will now be unmeasured variables associated with the missing particle, X_{π^0} $(p_{X_{\pi^0}}, \theta_{X_{\pi^0}}, \phi_{X_{\pi^0}})$. The measured variables for the fit will be the same $\bigcup_{\beta}\left\{p_\beta, \theta_\beta, \phi_\beta\right\}$, where β loops over all final state particles: $e', {}^4\mathrm{He}', \gamma_1, \gamma_2$. This will also fold the invariant mass "cut" into the confidence level cut, leaving one less systematic to worry about. Additionally, the invariant mass "cut" will know about the detectors' resolutions.

13.1 Setting Up Inputs

13.1.1 Covariance Matrix

The covariance matrix is the exact same as the previous one, as there are no additional measured variables added:

$$C_\eta = \mathrm{diag}\left(\sigma^2_{p_e}, \sigma^2_{\theta_e}, \sigma^2_{\phi_e}, \sigma^2_{p_{^4\mathrm{He}}}, \sigma^2_{\theta_{^4\mathrm{He}}}, \sigma^2_{\phi_{^4\mathrm{He}}}, \sigma^2_{p_{\gamma_1}}, \sigma^2_{\theta_{\gamma_1}}, \sigma^2_{\phi_{\gamma_1}}, \sigma^2_{p_{\gamma_2}}, \sigma^2_{\theta_{\gamma_2}}, \sigma^2_{\phi_{\gamma_2}}\right)$$

13.1.2 Input Kinematic Vectors

Before constructing our input vectors for the kinematic fit, let's define some momenta for the π^0:

$$\begin{aligned} \vec{\boldsymbol{p}}_{X_{\pi^0}} &:= \vec{\boldsymbol{p}}_{\gamma_1} + \vec{\boldsymbol{p}}_{\gamma_2} \\ E_{X_{\pi^0}} &:= \sqrt{\|\vec{\boldsymbol{p}}_{X_{\pi^0}}\|^2 + M_{\pi^0}^2} \\ P_{X_{\pi^0}} &:= \left(\vec{\boldsymbol{p}}_{X_{\pi^0}}, E_{X_{\pi^0}}\right) \end{aligned} \quad ,$$

Here, we explicitly use the nominal value of the π^0 invariant mass, $M_{\pi^0} = 0.1349766$ GeV/c^2 [2]. For exclusivity:

$$\begin{aligned} P_{\text{init}} &:= P_e + P_{^4\text{He}} \\ P_{\text{fin}} &:= P_{e'} + P_{^4\text{He}'} + P_{X_{\pi^0}} \end{aligned} \quad .$$

Then our constraints will come from:

$$\begin{aligned} P_{\text{Exc}} &:= P_{\text{init}} - P_{\text{fin}} \\ P_{\text{Decay}} &:= P_{X_{\pi^0}} - \left(P_{\gamma_1} + P_{\gamma_2}\right) \end{aligned} \quad .$$

Omitting primes(’), the input vectors are:

$$\vec{\boldsymbol{y}}^0 = \vec{\boldsymbol{\eta}} = \begin{bmatrix} p_e \\ \theta_e \\ \phi_e \\ p_{^4\mathrm{He}} \\ \theta_{^4\mathrm{He}} \\ \phi_{^4\mathrm{He}} \\ p_{\gamma_1} \\ \theta_{\gamma_1} \\ \phi_{\gamma_1} \\ p_{\gamma_2} \\ \theta_{\gamma_2} \\ \phi_{\gamma_2} \end{bmatrix} , \qquad \vec{\boldsymbol{x}}^0 = \begin{bmatrix} p_{X_{\pi^0}} \\ \theta_{X_{\pi^0}} \\ \phi_{X_{\pi^0}} \end{bmatrix} , \qquad \vec{\boldsymbol{c}} = \begin{bmatrix} (P_{\mathrm{Exc}})_x \\ (P_{\mathrm{Exc}})_y \\ (P_{\mathrm{Exc}})_z \\ (P_{\mathrm{Exc}})_E \\ \left(P_{\mathrm{Decay}}\right)_x \\ \left(P_{\mathrm{Decay}}\right)_y \\ \left(P_{\mathrm{Decay}}\right)_z \\ \left(P_{\mathrm{Decay}}\right)_E \end{bmatrix} .$$

Initially, the x-, y-, and z-components of P_{Decay} will be identically zero by definition but after the first iteration, the values will change accordingly.

13.1.3 Input Kinematic Matrices

In this $5C$-fit, there are both measured and unmeasured variables so we have both matrices B and A:

$$B = \begin{bmatrix} \frac{\partial c_1}{\partial \eta_1} & \cdots & \frac{\partial c_1}{\partial \eta_{12}} \\ \vdots & \ddots & \vdots \\ \frac{\partial c_8}{\partial \eta_1} & \cdots & \frac{\partial c_8}{\partial \eta_{12}} \end{bmatrix} , \qquad A = \begin{bmatrix} \frac{\partial c_1}{\partial x_1^0} & \cdots & \frac{\partial c_1}{\partial x_3^0} \\ \vdots & \ddots & \vdots \\ \frac{\partial c_8}{\partial x_1^0} & \cdots & \frac{\partial c_8}{\partial x_3^0} \end{bmatrix} .$$

We can now form the 8×12 matrix, B, and 8×3 matrix, A, by concatenating the eight 4×3 D_β matrices for B and two 4×3 D_β for A:

$$B = \begin{bmatrix} D_e & D_{^4\mathrm{He}} & 0 & 0 \\ 0 & 0 & D_{\gamma_1} & D_{\gamma_2} \end{bmatrix} \quad , \tag{13.1}$$

$$A = \begin{bmatrix} D_{X_{\pi^0}} \\ -D_{X_{\pi^0}} \end{bmatrix} \quad . \tag{13.2}$$

where D_β is defined in **Eq. 10.1**. The zeros from **Eq. 13.1** are 4×3 matrices with all 0.

13.2 Fit Outputs

13.2.1 Confidence Level Distribution

The kinematic fit produced the confidence level distribution seen in **Fig. 13.1** and a cut at 0.05 is applied.

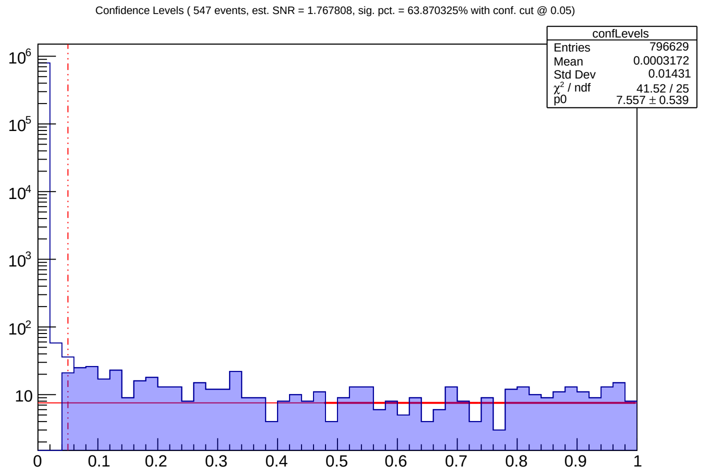

Figure 13.1: Confidence level distribution with a cut at 0.05, represented by the red vertical dashed line. The events passing the cut are represented by the light blue highlighted distribution which the right half is fitted to straight line to estimate the signal to noise ratio.

Note again that this is the only user-based cut in the entire event selection process.

13.2.2 Pull Distributions

The resulting pull distributions, **Fig. 13.2**, also look reasonable.

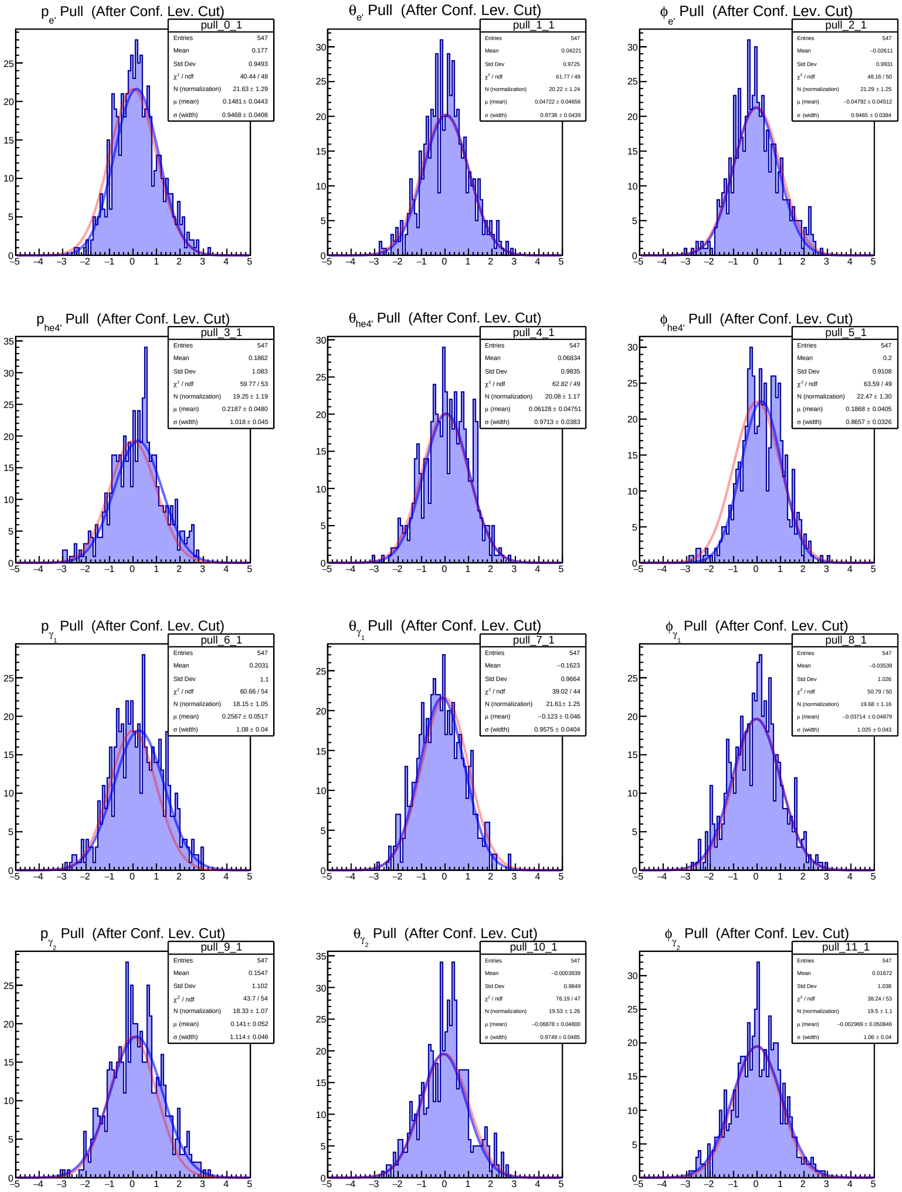

Figure 13.2: Pull distributions. From left to right we have p, θ, ϕ of the, from top to bottom, particles $e, {}^4\text{He}, \gamma_1, \gamma_2$. The blue curve is a gaussian fit to the distribution. The red curve is just a visual aid of what the distribution should be: a gaussian normalized to the blue curve with width 1, centered at 0.

13.3 Fit Results

13.3.1 Exclusivity Variable Distributions

The resulting exclusivity variable distributions obtained from the 5C-fit and CLC at 0.05 are shown in **Fig.** 13.3. Again, despite the similar distributions, the measured variables passing the kinematic fit (blue) have tails that are suppresed as compared to the ones passing the exclusivity cuts (black).

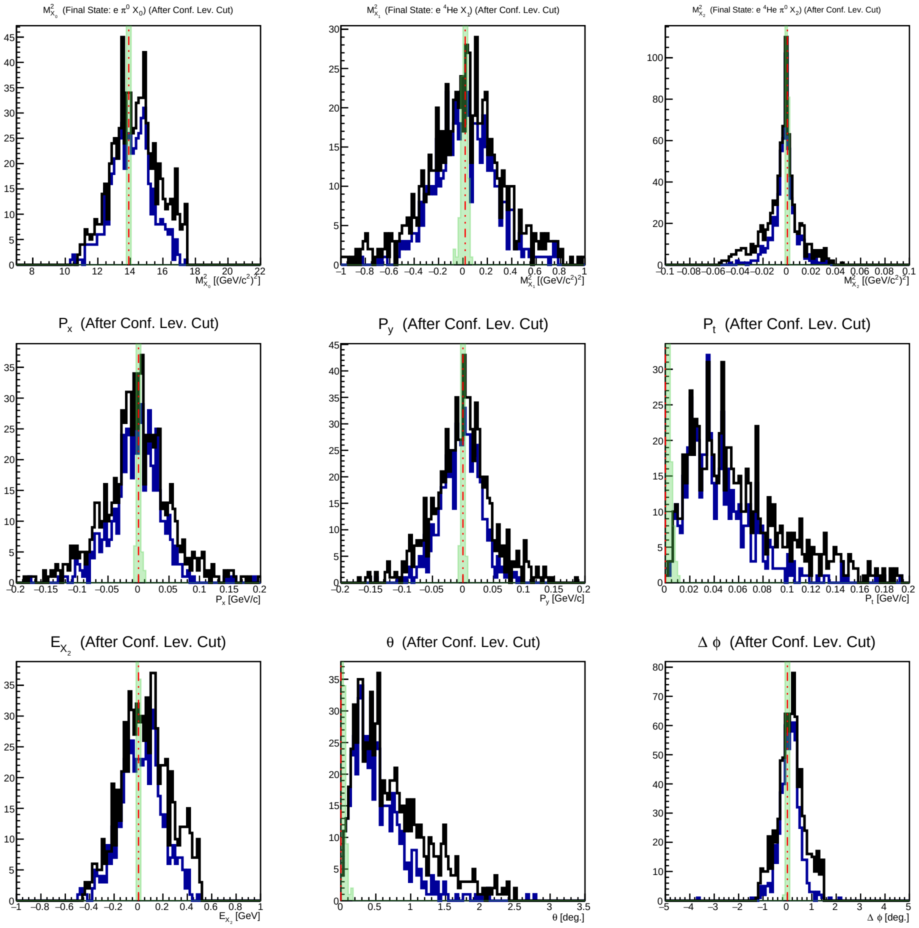

Figure 13.3: Exclusivity variable distributions for:
- Measured events passing exclusivity cuts (black)
- Measured events passing kinematic fit with 0.05 conf. level cut (blue)
- Fitted events passing kinematic fit with 0.05 conf. level cut (highlighted green)

13.3.2 Invariant Mass Distribution

The invariant mass distribution photon pairs is shown in **Fig. 13.4a** are within the previous study's cut but are not applied. Note that the fitted distribution (green) is more like a δ-function distribution with this additional constraint.

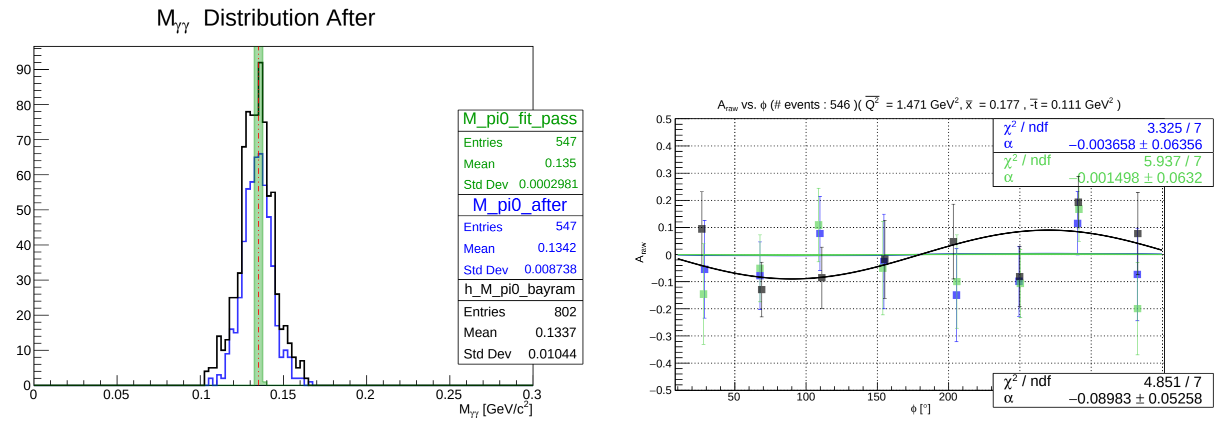

(**a**) Invariant mass distributions of photon pairs with the nominal value indicated by the vertical red line

(**b**) Raw beam spin asymmetries integrated over all $Q^2, x, -t$ bins

Figure 13.4: Invariant mass distributions of photon pairs (13.4a) and raw beam spin asymmetry (13.4b) for:
- Measured events passing exclusivity cuts (black)
- Measured events passing kinematic fit with 0.05 conf. level cut (blue)
- Fitted events passing kinematic fit with 0.05 conf. level cut (highlighted green)

13.3.3 Beam Spin Asymmetry

The raw beam spin asymmetries are shown in **Fig. 13.4b**. There is a major discrepancy between the previously measured beam spin asymmetry, A_{Raw} of $-8.9 \pm 5.3\%$ and the one obtained from this study using kinematic fitting more closely resembling no asymmetry ($-0.5 \pm 6.3\%$). This discrepancy needs to be looked into.

IX. Resolving Discrepancies in DVπ^0P Results

14. Resolving Discrepancies

Event selection through a set of exclusivity cuts and through kinematic fitting with a confidence level cut produce two very different asymmetries. To resolve these differences, we have to look at different subsets to pin down where the differences are coming from.

14.1 Breaking Down the Datasets

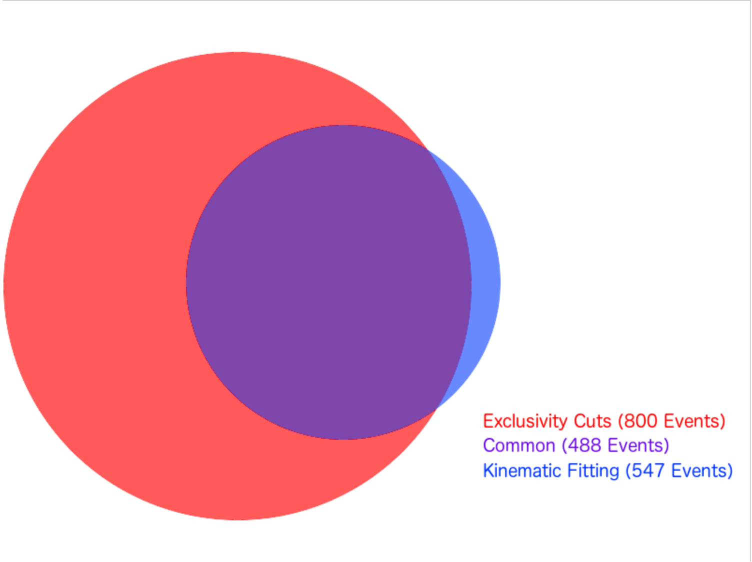

Figure 14.1: Venn diagram of events passing:
- Exclusivity cuts (red)
- Kinematic fitting with CLC: 0.05 (blue)

First, we form the union between all events passing exclusivity cuts and all events passing the 5C kinematic fitting (see **Fig.** 14.1). Then we can break it down to look at the different subsets. For a quick reference, we introduce Venn diagrams for the different subsets (see **Fig.** 14.2).

(a) Events passing exclusivity cuts **(b)** Events passing only exclusivity cuts

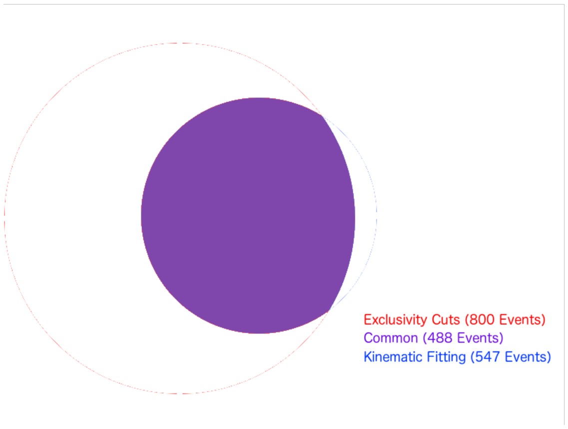

(c) Common events

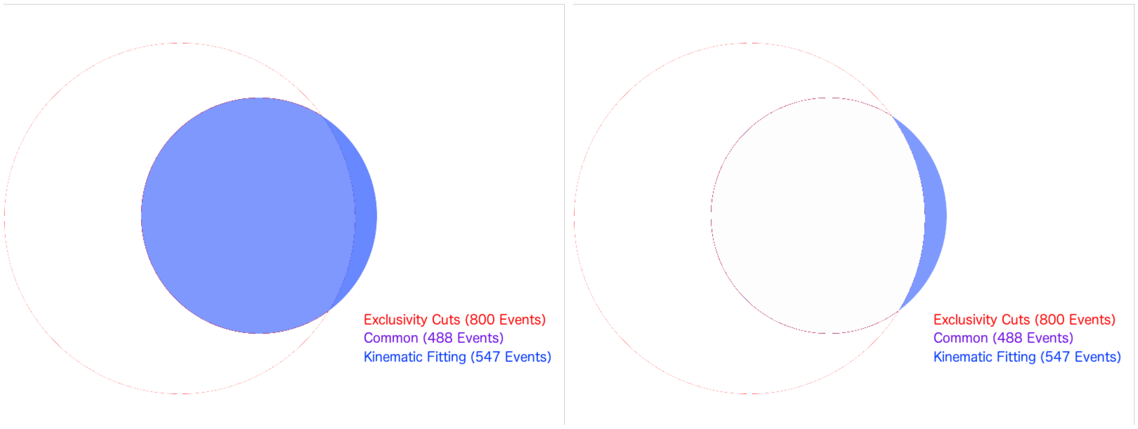

(d) Events passing kinematic fitting **(e)** Events passing only kinematic fitting

Figure 14.2: Proper subsets of the union of events passing exclusivity cuts and events passing kinematic cuts

14.2 Beam Spin Asymmetry

The first thing to look at to resolve the discrepancies is the each asymmetry to see if anything sticks out with this partitioning. Again, starting with the two results: all events passing exclusivity cuts (**Fig.** 14.3) from the previous study [1] and all events passing kinematic fitting (**Fig.** 14.4) from this study.

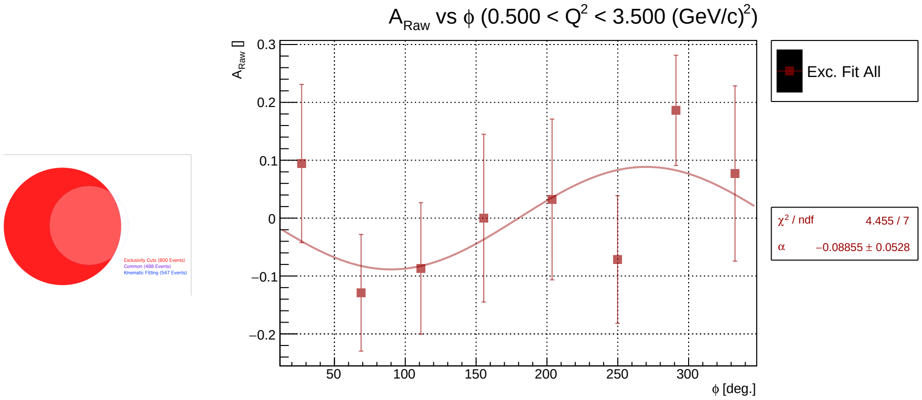

(**a**) 800 events (**b**) $A_{\text{Raw}} = -8.9 \pm 5.3\%$

Figure 14.3: Beam spin asymmetry (b) of selected events (a): All events passing exclusivity cuts

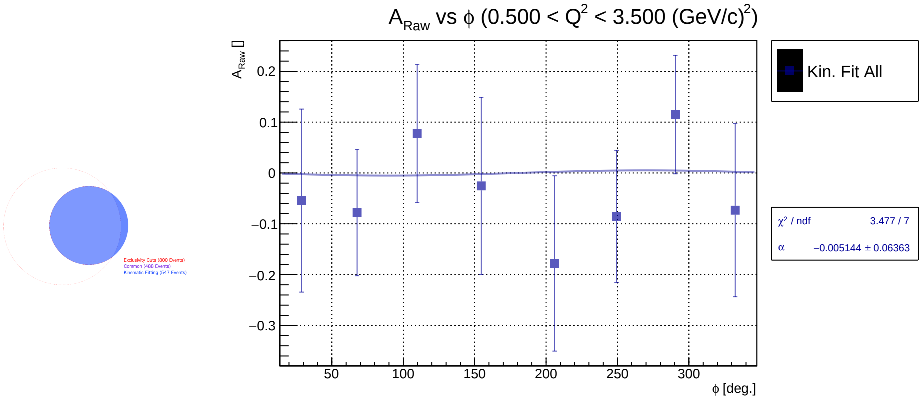

(**a**) 547 events (**b**) $A_{\text{Raw}} = -0.5 \pm 6.4\%$

Figure 14.4: Beam spin asymmetry (b) of selected events (a): All events passing kinematic fitting

To see if the discrepancy is beyond a difference in statistics, we look to the common events between the two methods produces an asymmetry (**Fig.** 14.5).

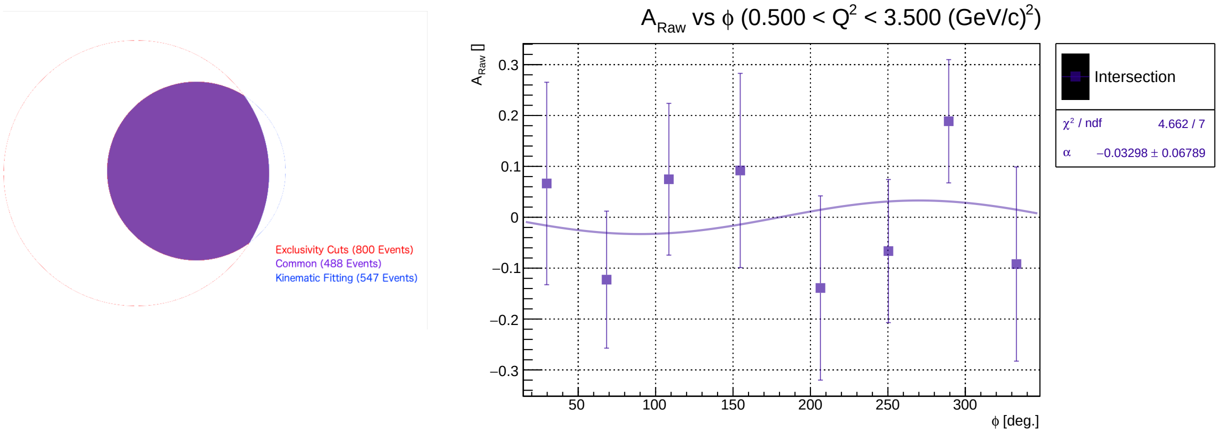

(a) 488 events

(b) $A_{\mathrm{Raw}} = -3.3 \pm 6.8\%$

Figure 14.5: Beam spin asymmetry (b) of selected events (a): Events passing both exclusivity cuts and kinematic fitting

What we see is that the set of common events brings asymmetry from events selected by exclusivity cuts substantially down (in magnitude) and brings the asymmetry from kinematic fitting up (in magnitude). That is, the common events' central value asymmetry ($-3.3 \pm 6.8\%$) has moved well outside the range of the previous study's asymmetry ($-8.9 \pm 5.3\%$). In comparison, the common events' central value asymmetry is within the kinematic fitting's asymmetry range ($-0.5 \pm 6.4\%$).

Although the common events do not reveal anything conclusive, the exercise of partitioning the dataset shows its benefit when looking into events passing only exclusivity cuts.

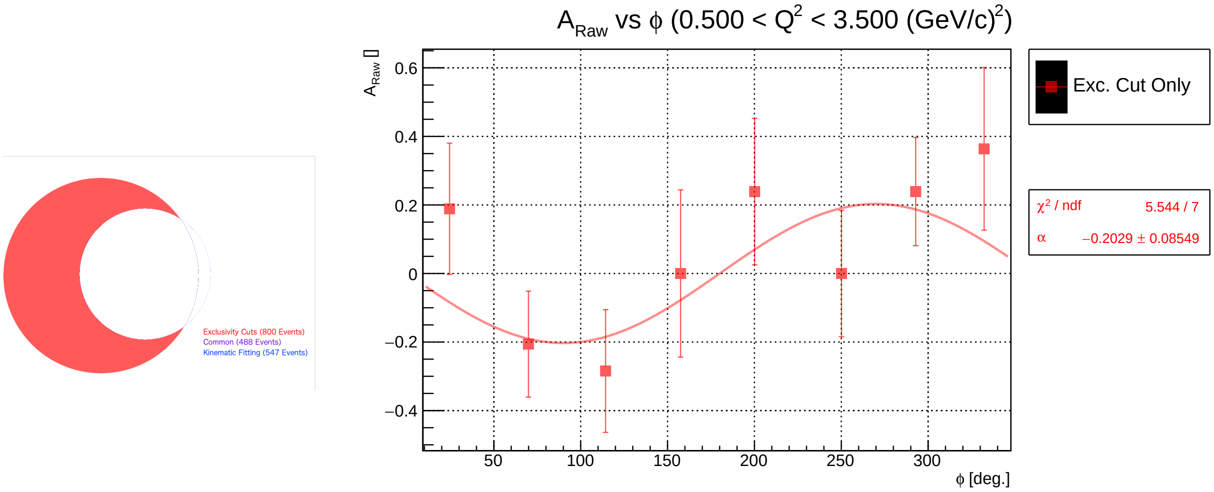

(a) 312 events (b) $A_{\mathrm{Raw}} = -20.3 \pm 8.5\%$

Figure 14.6: Beam spin asymmetry (b) of selected events (a): Events passing only exclusivity cuts

When taking events that only pass the exclusivity cuts, we see in **Fig. 14.6** that the asymmetry of these events are $-20.3 \pm 8.5\%$. This strong asymmetry is coming from over one-third of the events passing exclusivity cuts. To understand why it is these events that have such a high asymmetry, we look at the different distributions they produce.

14.3 Invariant Mass

An obvious first check would be to look to the invariant mass distribution of the photon pair to see if anything stands out. Looking at the invariant mass distribution of the disjointed sets in **Fig.** 14.7, there is nothing of note between the three distributions except maybe for the fact that the red distribution is wider.

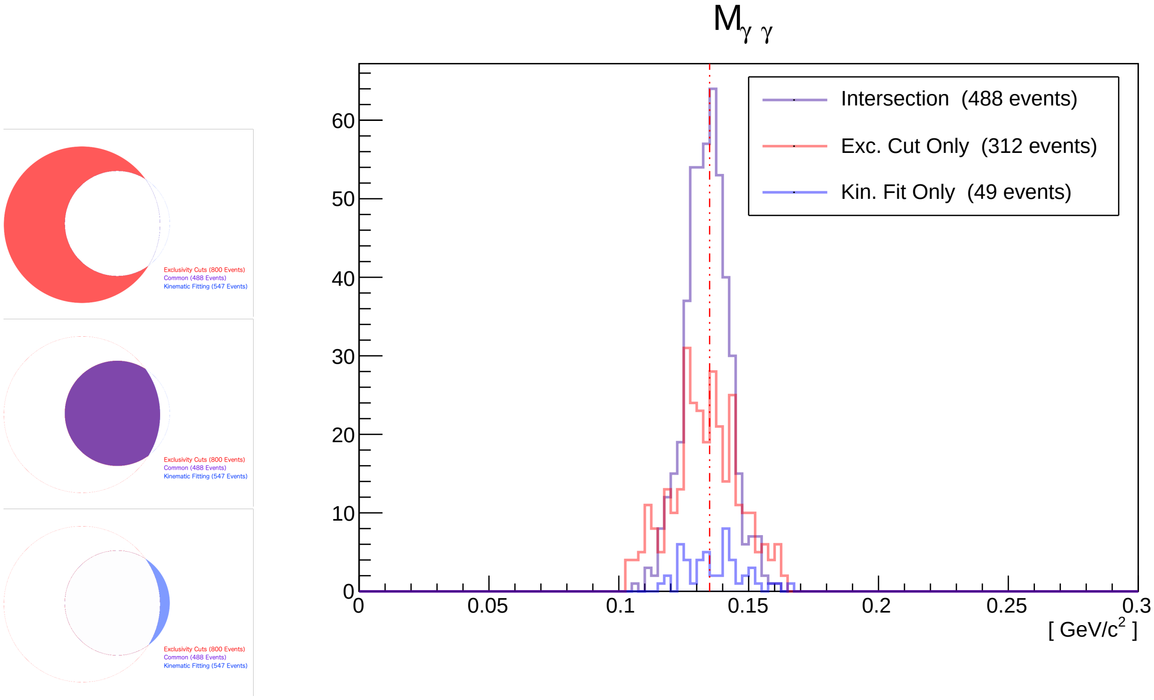

(**a**) Reference sets (**b**) Invariant mass distributions

Figure 14.7: Invariant mass distributions of the disjoint sets: passing exclusivity cuts only, common events, and kinematic fitting only

14.4 Exclusivity Variable Distributions

The exclusivity variable distributions show the interplay between the measured particles. These distributions should show whether the set of particles are part of the same event.

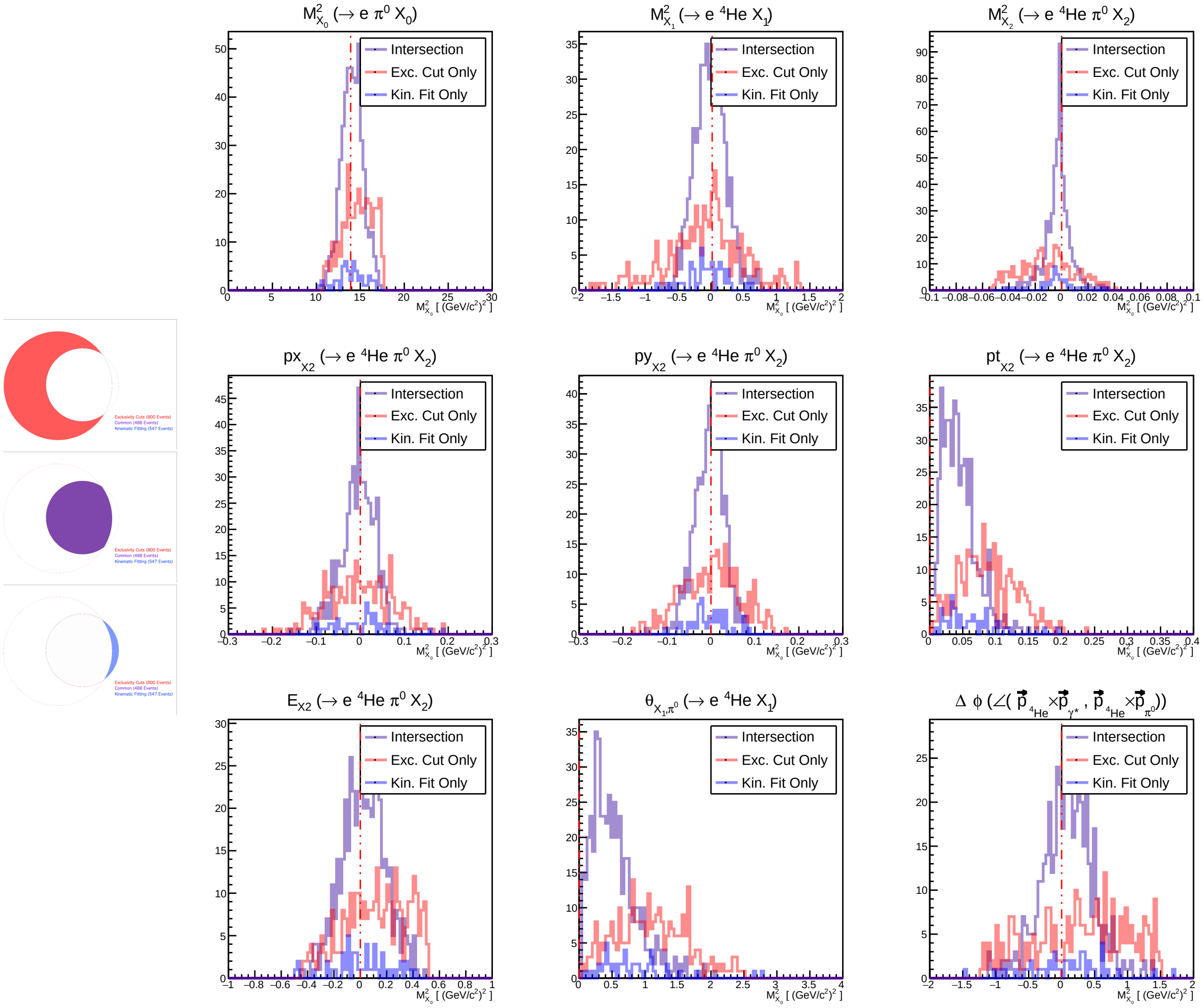

(a) Reference sets (b) Exclusivity variable distributions

Figure 14.8: Exclusivity variable distributions of the disjoint sets:
- passing exclusivity cuts only (red)
- common events (purple)
- kinematic fitting only (blue)

We see from **Fig. 14.8** that the blue distributions just look like more of the same of the purple distributions. However, the red distributions are much wider, having longer tails. In particular, the events passing only the exclusivity cuts (red), have:

- Distributions are centered farther out from their expected value of zero for:
  - the missing transverse momentum (pt_{X_2}),
  - the angle between the measured and missing π^0 (θ_{X_1,π^0})
- The coplanarity ($\Delta\phi$) is uniformly distributed with no clear peak
- The distributions have many events in the tail for:
  - The missing mass-squared ($M^2_{X_0}$) of the process $e^4\text{He} \rightarrow e'\pi^0 X_0$
  - The missing energy (E_{X_2}) of the process $e^4\text{He} \rightarrow e'^4\text{He}'\pi^0 X_2$

It is clear why these events fail the kinematic fitting: the events in the tails do not conserve momentum and energy within the detectors' errors. What is not obvious is why these events have such a higher magnitude in its asymmetry.

14.5 Summary

If we focus on just the previous dataset, obtained from exclusivity cuts, we can reframe the results.

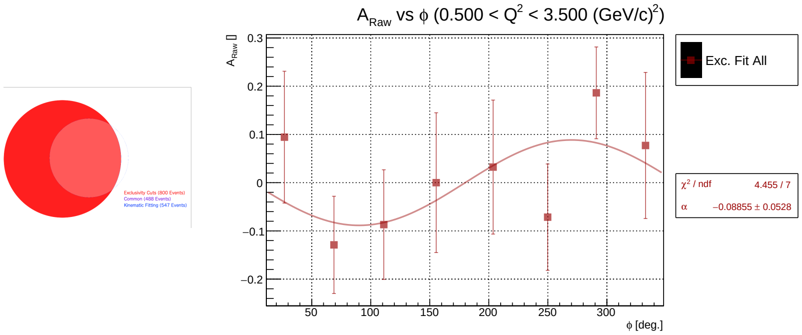

(a) 800 events

(b) $A_{\mathrm{Raw}} = -8.9 \pm 5.3\%$

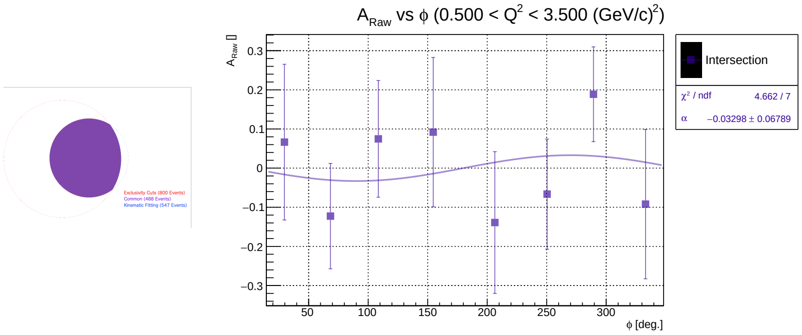

(c) 488 events

(d) $A_{\mathrm{Raw}} = -3.3 \pm 6.8\%$

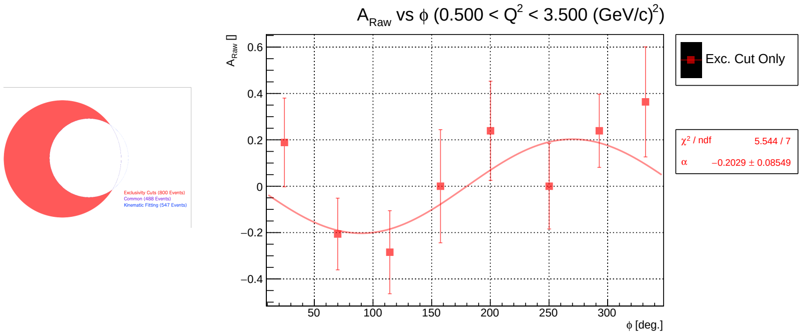

(e) 312 events

(f) $A_{\mathrm{Raw}} = -20.3 \pm 8.5\%$

Figure 14.9: Beam spin asymmetries of selected events:
(b) Events passing exclusivity cuts
(d) Events passing kinematic fitting
(f) Events failing kinematic fitting

The kinematic fitting has the surprising effect of partitioning the previous study's 800 coherent π^0 events into 312 events with a strong asymmetry ($-20.3\pm8.5\%$) and 488 events with little to no asymmetry ($-3.3 \pm 6.8\%$), as can be seen in **Fig. 14.9**. The difference between the events is just whether or not they pass kinematic fitting.

Admittedly, it is not clear where exactly this large background asymmetry is coming from. However, it is clear that events passing both exclusivity cuts and kinematic fitting is diluting this large asymmetry and producing the asymmetry from the previous study.

X. Conclusion and Outlook

Kinematic fit, as formulated and outlined, works well based on a myriad of observations.

From fit quality:

- Confidence level distribution: Sharp peak at zero and a plateau thereafter as expected
- Pull distributions: All look normally distrbuted with means near 0 and widths close to 1

From fit results:

- Exclusivity variable distributions: Very similar distribution to ones passing all exclusivity cuts but with suppressed tails
- Invariant mass distribution: Without any input or reference to the nominal π^0 invariant mass, the events passing the $4C$ kinematic fit produces a very clean invariant mass distribution

- Beam spin asymmetries: All A_{raw} vs. ϕ data points are consistently within error bars of previous studies with χ^2/ndf of the asymmetry fit (mostly) less than previously measured.

The higher statistics DVCS events show that the kinematic fit is consistent with exclusivity cuts, validating the procedure. The power of this method is shown when dealing with the lower statistics DVπ^0P events, wherein the fit is able to throw away bad events that no obvious set of traditional cuts can eliminate. The kinematic fit is able to separate a high asymmetry background from an asymmetry consistent with zero for DVπ^0P.

Improvements in kinematic fitting can be made. Errors and widths can be studied in full detail for both the RTPC and the EC to improve the covariance matrix used in kinematic fitting.

More impactful, recalibration of the RTPC can increase statistics. Additionally, the variances of the ^{4}He tracking variables are not well studied, as the calculated variance are independent of one another. Worse yet, the varaiances of θ and ϕ are fixed numbers, not depending on the kinematics of ^{4}He in the RTPC at all. At its core, to get more out of kinematic fitting, the RTPC needs to be revisted. A calibration of the tracking variables, p, θ, ϕ itself may even improve the number of coherent events. Combined with the kinematic dependence of the (co)variances and a good understanding of energy loss effects, the use of the kinematic fit can go beyond just selecting good, clean events; kinematic fitting can be used to improve measurements coming from the detectors.

Appendices

A. Corrections and Calibrations

A.1 Electron Vertex Correction

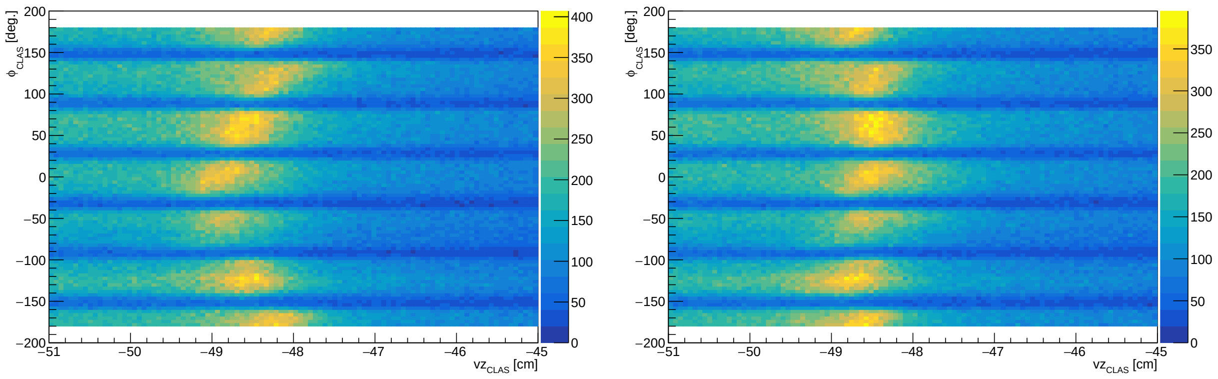

(**a**) Before correction

(**b**) After correction

Figure A.1: Vertex Correction: An azimuthal angle dependent vertex shift is implemnted to account for changes in beam position.

Reconstruction assumes the beam to be fixed at the origin CLAS, when projecting CLAS along the beam axis. However, changes in the experiment reveal the position moves. To account for beam movement over the course of the experimental run, a correction to the vertex is developed by N. Baltzell [22]. The correction has the form:

```
vz_corr = vz[ipart] - r/tan(theta) cos( phi - phi_0 )
```

where the parameters `r` and `phi_0` are given in **Table A.1** and `theta` and `phi` are the polar and azimuthal angle measured in CLAS given by the direction unit-vector $\hat{\boldsymbol{p}}$ in **Eq. A.1**.

$$\hat{\boldsymbol{p}} = \begin{bmatrix} \texttt{cx[ipart]} \\ \texttt{cy[ipart]} \\ \texttt{cz[ipart]} \end{bmatrix} \tag{A.1}$$

Table A.1: Vertex Correction Paramters

Variable	**Value**	**Units**
r	0.24	cm
phi_0	-186.6	deg.

A.2 RTPC Corrections

A.2.1 θ_{RTPC} Correction

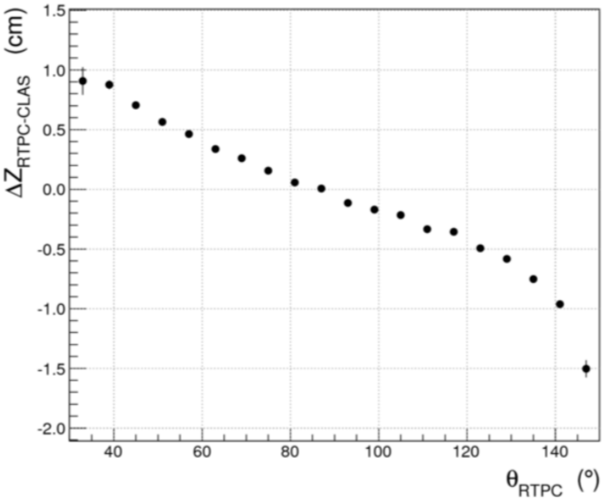

Figure A.2: RTPC Vertex Correction: Δz vs θ showing a linear dependence [23].

When checking the vertex measured by CLAS and the RTPC, there was a strong linear dependence in the reconstructed RTPC θ vertex. First a correction to the polar angle, developed by N. Baltzell [23], is applied:

$$\theta_{\text{RTPC}} = \frac{\Delta z}{\texttt{r}} \sin(2\theta) \tag{A.1}$$

from **Fig. A.2**, we see that Δz, in cm, is linear in θ:

$$\Delta z = \texttt{m}\theta_{\text{deg}} + \texttt{b} \tag{A.2}$$

where the parameters of the slope `m` and intercept `b` are given by

```
m = -0.017
b = 1.53
```

θ and θ_{deg} are the uncorrected the RTPC polar angle ($\theta_\circ$ is in degrees) and the parameter `r` = 4.5 cm is the radial position half way through the drift region.

A.2.2 vz_{RTPC} Correction

Now that the polar angle is corrected, the vertex can be shifted into place:

$$vz_{\text{RTPC}} = z_{\text{cm}} - \Delta z \tag{A.1}$$

and z_{cm} is the original, uncorrected RTPC vertex from the `GCPB` bank but in cm.

A.3 EC Calibration

The need for calibration of the EC becomes apparent when looking at the invariant mass distribution of photon pairs coming from the EC, as can be seen in **Fig. A.3**. There is clear peak near the nominal mass of π^0 but there is about a 10% shift that is consistent over all runs. First, a check is made on the sampling fraction over the course of the experiment for each sector. Then, an in-depth look at the energy dependent scaling, with the constraint of the π^0 invariant mass, is applied to each of the photons in the pair.

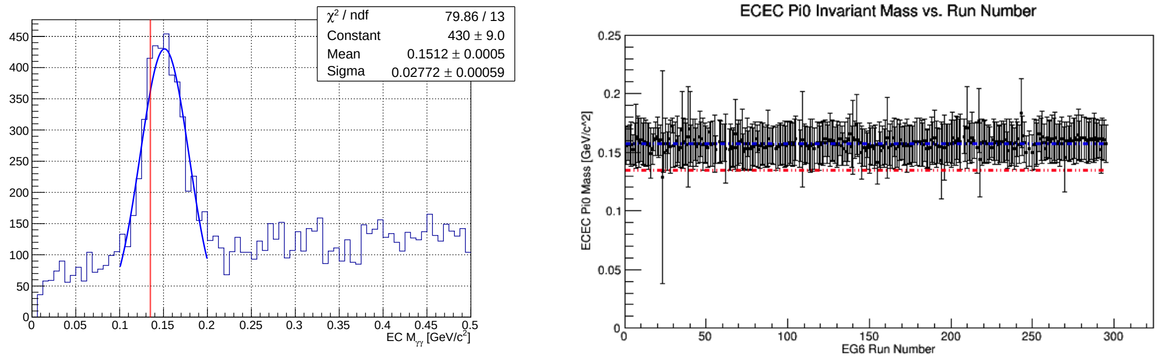

(a) The invariant mass distribution over a single run (Run Number 61510).

(b) The invariant mass over all runs.

Figure A.3: The invariant mass distribution of EC photon pairs over one run (A.3a) and all runs (A.3b). The red line represents the nominal π^0 mass and the blue represents the mean from fit to the data.

A.3.1 Sampling Fraction Correction

The sampling fraction is the fraction of the energy that a particle traversing the EC deposits in the sensitive scintillating material. Energy is deposited in the lead blocks too but that area is not sensitive to measurement. Although the sampling fraction was optimized by simulation to be 0.293, measurements show that this valued varied as a function of time (explicitly, of run number and event number). To explicitly see what its effect on each sector, a measurement of the sampling fraction over the EG6 run for each sector was made as seen in **Fig.** A.4.

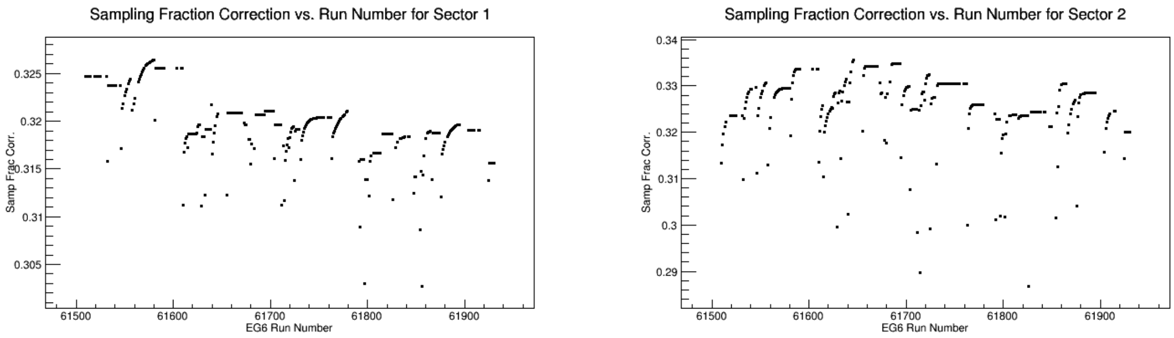

(a) Sector 1 **(b)** Sector 2

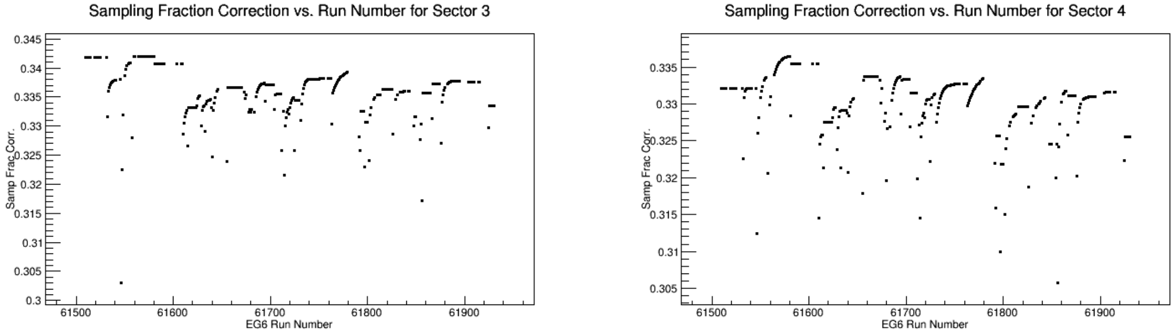

(c) Sector 3 **(d)** Sector 4

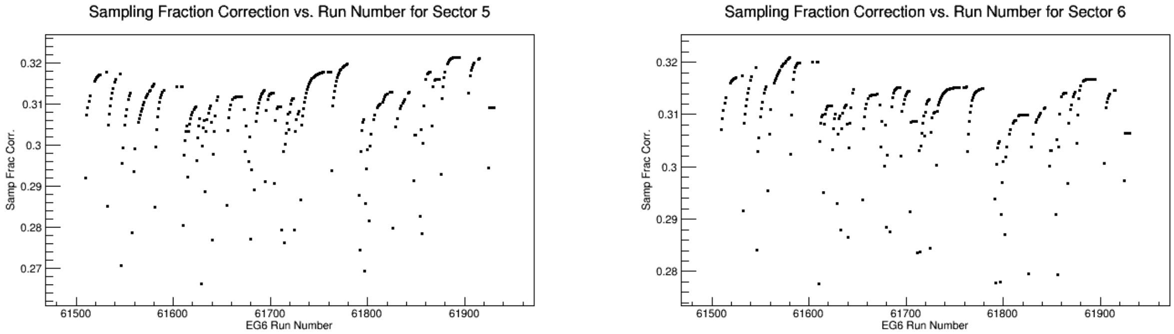

(e) Sector 5 **(f)** Sector 6

Figure A.4: Sampling Fraction vs. Run Number for each EC sector.

Each of these six sector sampling fractions can be fit to replace the fixed sampling fraction of 0.293. An extensive study was done by Cole Smith and then Nathan Baltzell [20] to determine the parameters of the functional form:

$$\texttt{sampFrac}(s,x) = E_0 + A\left(\exp\left[-\alpha\left(x-x_0\right)\right] + \exp\left[-\beta\left(x-x_0\right)\right]\right) \tag{A.1}$$

where the sampling fraction depending on the sector, s, and the effective time, $x := r + f/150$, with r and f representing the run and file number, respectively.

The other parameters, E_0, A, α, β, and x_0 all also depend on s and x. Overall, `sampFrac` is piece-wise in x, for each sector, as can be seen in **Fig.** A.5. The values of all of these parameters are tabulated and can be found in [20].

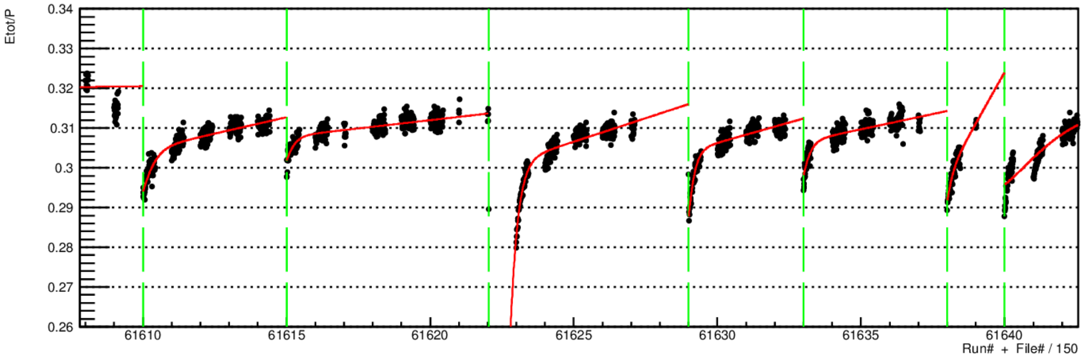

Figure A.5: A fit to the measured sampling fraction as a function of event number [20].

The result of the fit gives a better invariant mass distribution over the entire EG6 run, as can be seen in **Fig.** A.6.

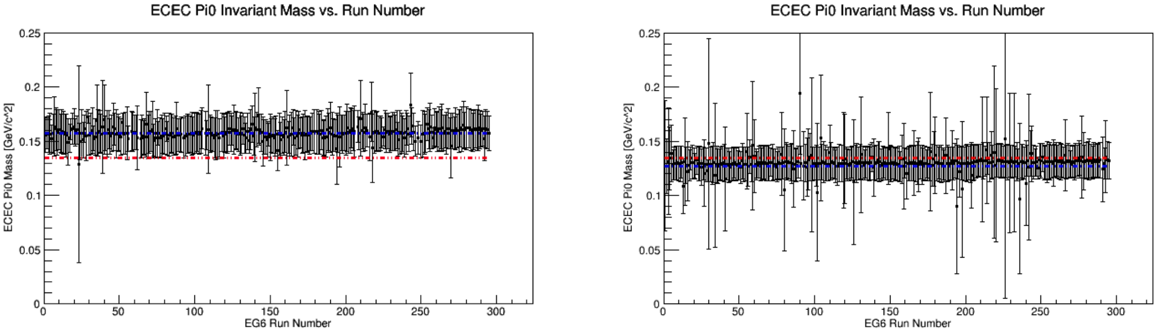

(a) Before sampling fraction correction

(b) After sampling fraction correction

Figure A.6: Comparison of the invariant mass distribution before (A.6a) and after (A.6b) the sampling fraction correction.

A.3.2 Scaling Factor Correction

Taking a closer look at the π^0 invariant mass as a function of run number, there is a still a uniform shift over all sectors, over all run numbers.

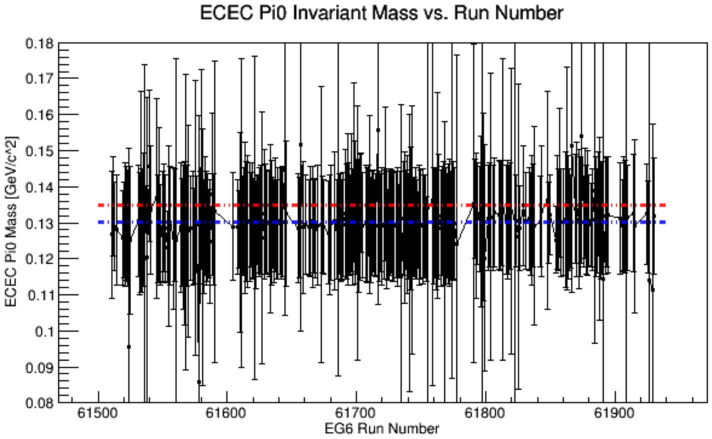

Figure A.7: Invariant mass distribution vs run number zoomed in.

Comparing this to the IC photon pairs, in **Fig. A.8**, we see that even when zoomed in, the shift is not as dramatic.

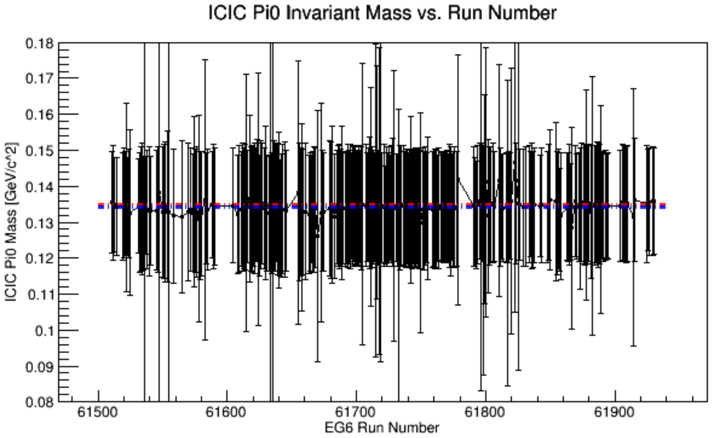

Figure A.8: Invariant mass distribution vs run number of IC photons.

To see where this shift is coming from, we check to see if there is an energy dependence in the two-photon invariant mass. In **Fig. A.9**, the two-photon invariant mass is plotted against the lower energy photon. It reveals that the invariant mass may be linearly dependent on the energy of the lower photon.

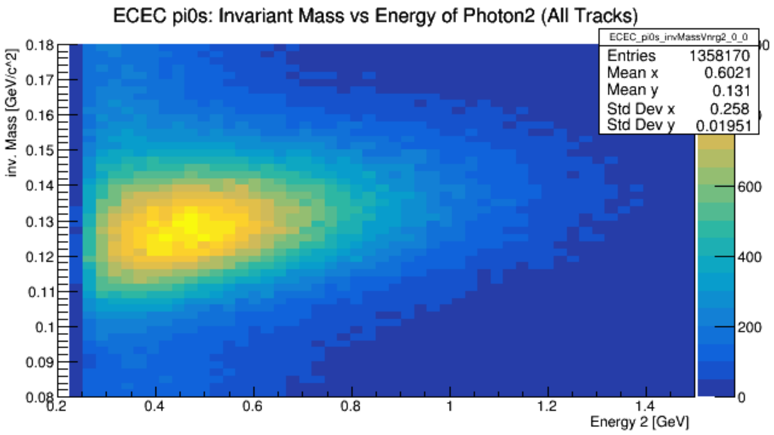

Figure A.9: Invariant mass of two EC photons vs. energy of the lower energy photon : The peak of the invariant mass is dependent on the energy of the lower energy photon.

Assuming that the measured EC energy, E'_γ, has a scaling factor, c, we can rewrite the energy as:

$$E'_\gamma = cE_\gamma$$

where E_γ is the true photon energy. Then the measured invariant mass, $M_{\gamma\gamma}$ will be expressed as, in terms of the scaling factor, c as:

$$\begin{aligned} M^2_{\gamma\gamma} &= \left(E'_{\gamma_1} + E'_{\gamma_2}\right)^2 - \|\vec{\boldsymbol{p}}_{\gamma_1} + \vec{\boldsymbol{p}}_{\gamma_2}\|^2 \\ &= 2E'_{\gamma_1}E'_{\gamma_2}\left(1 - \cos\theta_{\gamma\gamma}\right) \\ &= 2c_1c_2E_{\gamma_1}E_{\gamma_2}\left(1 - \cos\theta_{\gamma\gamma}\right) \end{aligned}$$

To do this systematically, let us consider symmetric π^0. That is, π^0 formed from two photons with equal energy, $E_1 = E_2 =: E$ and $c_1 = c_2 =: c$. Then,

$$M^2_{\gamma\gamma} = 2\,(cE)^2\left(1 - \cos\theta_{\gamma\gamma}\right)$$

and solving for the factor, c, gives

$$c = \frac{M_{\gamma\gamma}}{E\sqrt{2\left(1-\cos\theta_{\gamma\gamma}\right)}} \quad . \tag{A.1}$$

Experimentally, choosing truly symmetric π^0 is too restrictive. Instead, closely symmetric π^0, with an energies satisfying $|E_1 - E_2| < 100$ MeV, are chosen. Then **Eq. A.1** becomes:

$$\bar{c} = \frac{M_{\gamma\gamma}}{\bar{E}\sqrt{2\left(1-\cos\theta_{\gamma\gamma}\right)}} \tag{A.2}$$

where $\bar{E}$ is the average photon energy and $\bar{c}$ is the effective scaling factor.

In **Fig. A.10** the scaling factor, $\bar{c}$, as a function of the average photon energy, $\bar{E}'$ is plotted. We see that this scaling factor is dependent on $\bar{E}'$:

$$\bar{c} \equiv \bar{c}\left(\bar{E}'\right) \quad . \tag{A.3}$$

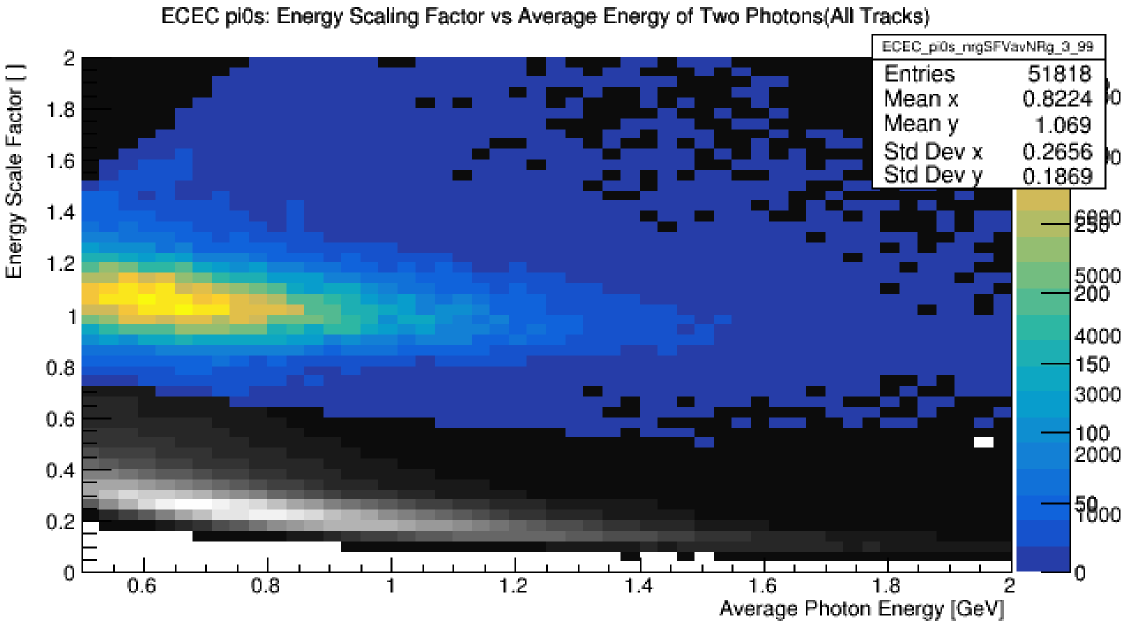

Figure A.10: Scaling factor vs. average energy: The energy scaling factor decreases with increasing energy.

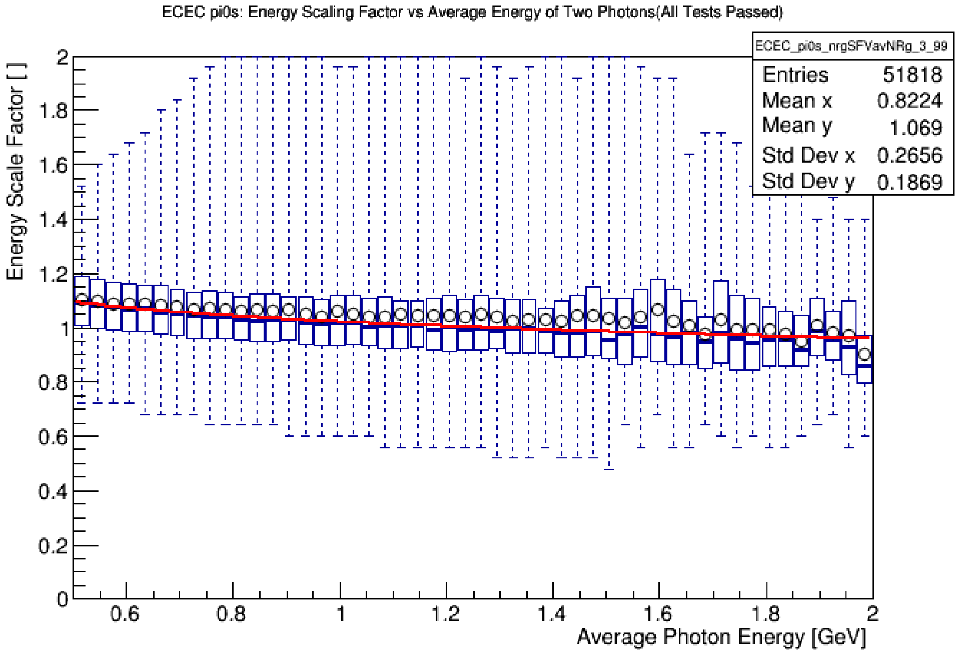

Figure A.11: Scaling factor vs. average energy: Candle-plot profile of **Fig. A.10** with fit **Eq. A.4**.

Although on first glance it looks linear, slicing the distribution into strips, the candle-plot of the profile in **Fig. A.11** reveals that the relationship is not as trivial as a linear one.

Omitting the bars, a fit of the form:

$$c(E) = 1 + aE + \frac{b}{E} \tag{A.4}$$

is applied and a qualitative look can be seen in **Fig. A.11**. The values of fit parameters a and b are listed in **Table A.2**.

Table A.2: Scaling Factor Paramters

Parameter	Value	Units
a	-0.0354677	GeV^{-1}
b	0.0563963	GeV

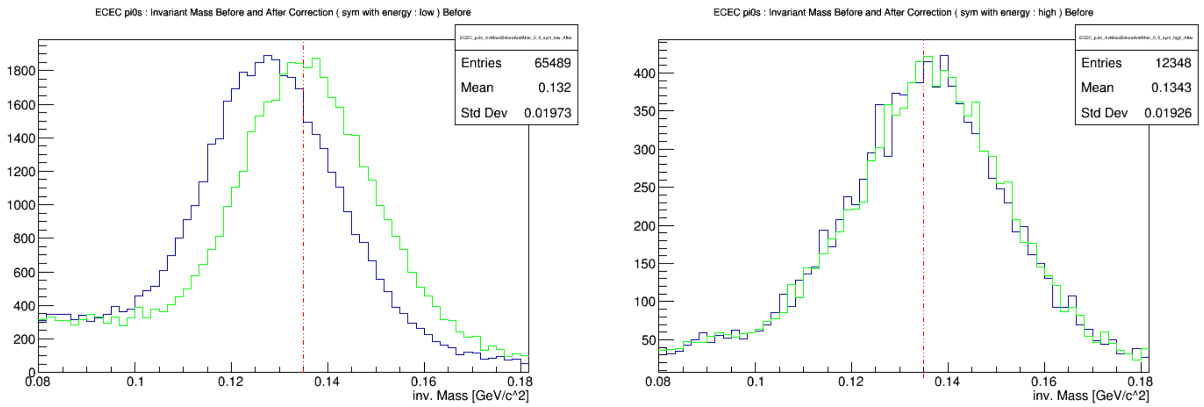

(a) Low energy ($E_{\gamma\gamma} < 1.8 GeV$) invariant mass distribution.

(b) High energy ($E_{\gamma\gamma} > 1.8 GeV$) invariant mass distribution.

Figure A.12: Invariant mass distribution for low (A.12a) and high (A.12b) energy symmetric EC π^0. The blue and green are the uncorrected and corrected distributions, respectively. The red line represents the nominal value of the π^0 invariant mass.

To see how it affects the invariant mass of EC photon pairs, we partition the symmetric π^0's into low energy and high energy π^0's (see **Fig. A.12**).

We see that this correction does exactly what we want: it scales up the poorly reconstructed low energy EC photons, while leaving the well reconstructed EC photons essentially unchanged (see **Fig. A.12**). To check if this correction only works for symmetric π^0, this symmetric criterion is lifted and the invariant mass is checked again.

Again, we see from **Fig. A.13**, that higher energy π^0 are unchanged and the lower energy π^0 are shifted in the right direction. This shows that although the symmetric π^0 were used to simplify the correction, the correction cares only on the energy of the individual photons, justifying the omission of the bars in **Eq. A.4**.

Here, we can see that the invariant mass is shifted much closer to the nominal value for each run (**Fig. A.15**), and integrated over all runs (**Fig. A.14**).

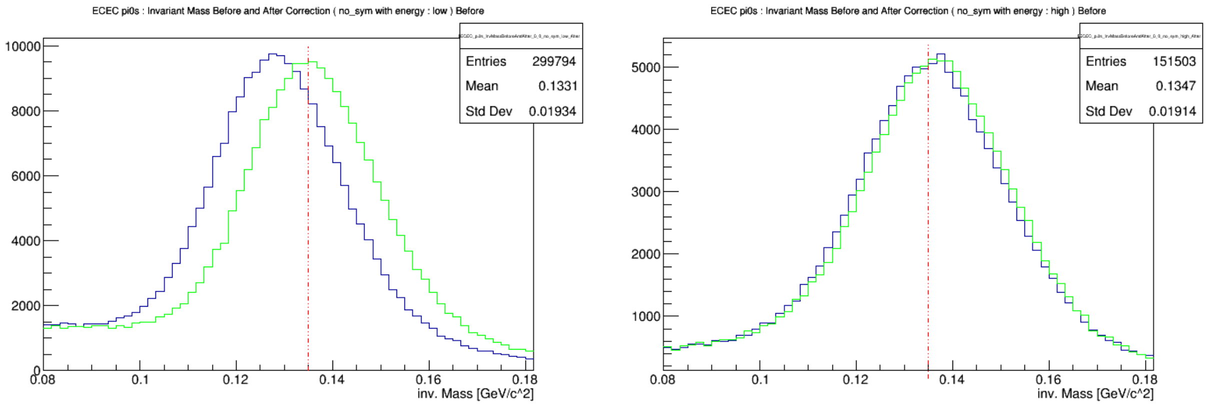

(**a**) Low energy ($E_{\gamma\gamma} < 1.8 GeV$) invariant mass distribution. (**b**) High energy ($E_{\gamma\gamma} > 1.8 GeV$) invariant mass distribution.

Figure A.13: Invariant mass distribution for low (A.13a) and high (A.13b) energy generic EC π^0. The blue and green are the uncorrected and corrected distributions, respectively. The red is the nominal value of the π^0 invariant mass.

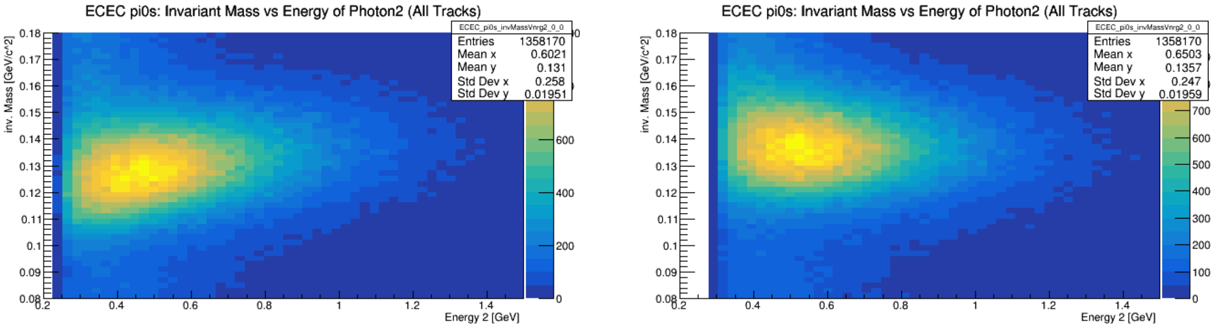

(**a**) Before sampling fraction correction (**b**) After sampling fraction correction

Figure A.14: Comparison of the invariant mass distribution vs energy of lower energy photon before (A.14a) and after (A.14b) the sampling fraction correction.

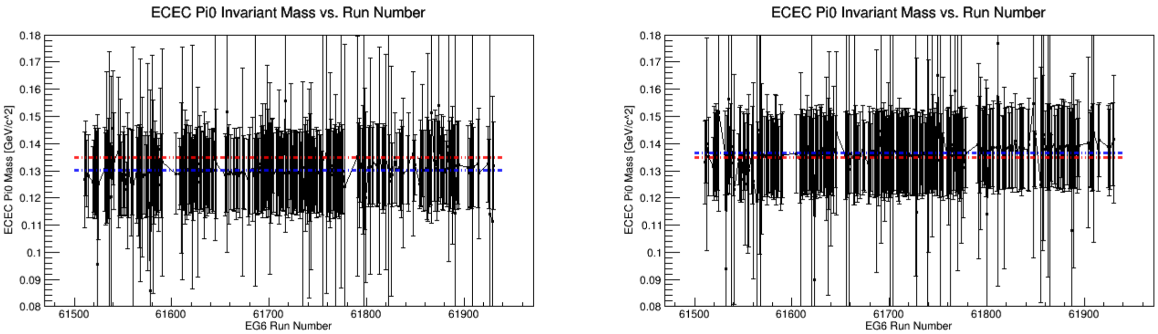

(**a**) Before scaling factor correction (**b**) After scaling factor correction

Figure A.15: Comparison of the invariant mass distribution vs run number before (A.15a) and after (A.15b) the scaling factor correction (but after sampling fraction correction).

In summary, the sampling fraction correction shifts the invariant mass closer to nominal value but overshoots by quite a bit. A study of the symmetric π^0 reveal that this overshoot was due to poorly reconstructed low EC energy photons. These are corrected and combined, giving a better measurement of energy coming from the EC.

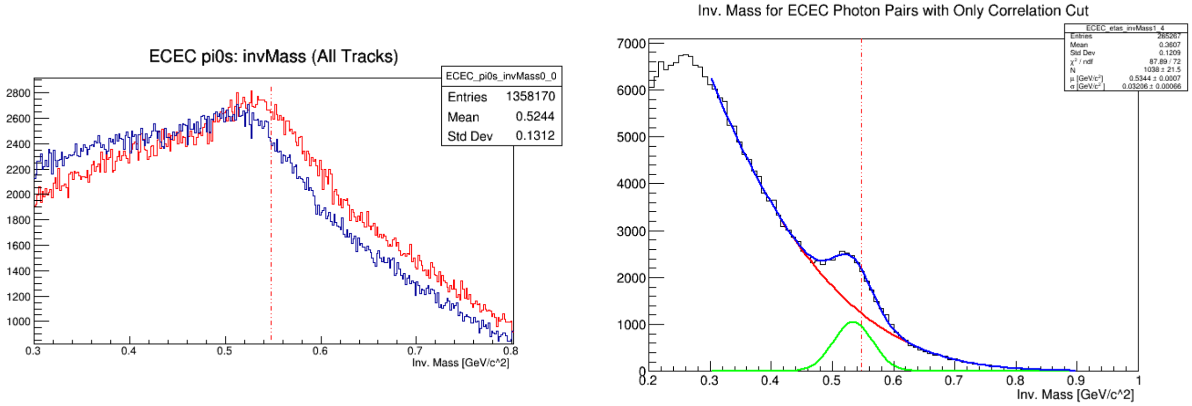

(a) All EC photon pairs: The blue and red are the uncorrected and corrected distributions, respectively.

(b) EC photon pairs coming from neighboring sectors: The blue, red, and green are the full corrected, fitted background, and the extracted signal (from subtracting fitted background distribution from full distribution) distributions, respectively.

Figure A.16: Invariant mass distribution EC photons: The red line represents the nominal value of the η invariant mass.

Furthermore, the invariant mass of the photon pairs show an enhancement of the peak right around the nominal value for η. An additional selection of photons in neighboring sectors $\left(\Delta\phi_{\gamma\gamma} \approx 60^\circ\right)$ reveals a clear η signal buried under a smooth background. Although there are very few events that pass event selection, a yield can be estimated with the right cuts.

B. Supplemental Pseudocode for PID

B.1 EC Fiducial Cut

`u`, `v`, and `w` make up the coordinates of the EC's scintillating strips, are explicitly given by

```
u = (y_rel - y_lo)/sin(rho)
v = (y_hi - y_lo)/tan(rho) - x_rel + (y_hi - y_rel)/tan(rho)
w = (0.5/cos(rho))*((y_hi - y_lo)/tan(rho) + x_rel + (y_hi - y_rel)/tan(rho))
```

having relative `x_rel` and `y_rel` coming from the linear transformation:

$$\begin{bmatrix} \texttt{x\_rel} \\ \texttt{y\_rel} \\ \texttt{z\_rel} \end{bmatrix} = \begin{bmatrix} \cos(\theta_{\mathrm{EC}})\cos(\phi_{\mathrm{EC}}) & -\sin(\phi_{\mathrm{EC}}) & \sin(\theta_{\mathrm{EC}})\cos(\phi_{\mathrm{EC}}) \\ \cos(\theta_{\mathrm{EC}})\sin(\phi_{\mathrm{EC}}) & \cos(\phi_{\mathrm{EC}}) & \sin(\theta_{\mathrm{EC}})\sin(\phi_{\mathrm{EC}}) \\ -\sin(\theta_{\mathrm{EC}}) & 0. & \cos(\theta_{\mathrm{EC}}) \end{bmatrix} \begin{bmatrix} \texttt{x\_ec} \\ \texttt{y\_ec} \\ \texttt{z\_ec} \end{bmatrix} - \begin{bmatrix} 0.00 \\ 0.00 \\ 510.32 \end{bmatrix} .$$

Here `x_ec`, `y_ec`, and `z_ec` are the $x-$, $y-$, and $z-$ coordinates of the EC hit with

```
x_ec = ech_x[ec[ipart]-1]
y_ec = ech_y[ec[ipart]-1] .
z_ec = ech_z[ec[ipart]-1]
```

The EC sector's central azimuthal angle, ϕ_{EC}, is determined from sector index, `isect` ($\in \{0, \ldots, 5\}$), which depends on the particle's shifted azimuthal angle, ϕ_{shifted} ($\in [0, 360]^\circ$):

$$\phi_{\text{EC}} = \texttt{isect} * \frac{2\pi}{6}; \qquad .$$
$$\texttt{isect} = \lfloor \phi_{\text{shifted}} / 60^\circ \rfloor$$

The rest of the variables, listed in **Table B.1**, are hard-coded, fixed values representing the geometrical configuration of the EC.

Table B.1: Hard-Coded EC Values

Variable	**Value**	**Units**
θ_{EC}	0.4363323	rad.
`rho`	1.0976200	rad.
`y_lo`	-182.974	cm
`y_hi`	189.956	cm

B.2 IC Hot Channels Cut

Table B.2: Index of bad crystals

Index i	`ix_bad[i]`	`iy_bad[i]`
0	-8	-2
1	-4	-6
2	-2	-6
3	-1	-6
4	3	-8
5	8	-10
6	-5	8
7	-9	-6

The hot channels that are overactive are taken out by explicitly looping over the bad crystals:

```
isInICHotChannel(ix, iy){
  for( int ii = 0; ii < 8; ii++ ){
    x_bad = ix_bad[ii]
    y_bad = iy_bad[ii]
    if( ix == x_bad && iy == y_bad )
      return true
  }
  return false
}
```

where `ix_bad` and `iy_bad` are arrays tabulated in **Table B.2**.

B.3 IC Fiducial Cuts

The IC Fiducial is defined as:

```
isInICFiducial(x,y){
  if( isOutICOuterEdge(x,y) ) return false
  if( isInICnnerEdge(x,y)   ) return false
  return true
}
```

where the cut requires passing the inner and outer edge cuts of the calorimeter.

B.3.1 IC Fiducial Outer Edge Cut

The outer calorimeter cut, `isOutICOuterEdge(x,y)`, can be expressed as:

```
isOutICOuterEdge(x,y){
  if( abs(x)/dx          >= nout           ||
      abs(y)/dy          >= nout           ||
      abs( x/dx - y/dy ) >= nout * sqrt(2) ||
      abs( x/dx + y/dy ) >= nout * sqrt(2)
    ) return true
  return false
}
```

returning `false` if the hit is outside the outer fiducial region and `true` if it is inside.

B.3.2 IC Fiducial Inner Edge Cut

The inner calorimeter cut, `isInICInnerEdge(x,y)`, can be expressed as

```
isInICInnerEdge(x,y){

  if( abs(x)/dx           <= nin           &&

      abs(y)/dy           <= nin           &&

      abs( x/dx - y/dy ) <= nin * sqrt(2) &&

      abs( x/dx + y/dy ) <= nin * sqrt(2)

    ) return true

  return false

}
```

returning `false` if the hit is outside the inner fiducial region and `true` if it is inside.

- -

The hard-coded parameters in the expressions above are listed in **Table B.3**, represent the size of the pixel and the number of pixels to the inner and outer diagonal of the octagonal cut applied to the IC.

Table B.3: IC Parameters

Variable	Value	Units
dx	1.346	cm
dy	1.360	cm
nin	3.25	–
nout	10.75	–

B.4 RTPC Fiducial Cuts

The RTPC Fiducial Cut, `isInRTPCFiducial`, depends on three other cuts:

```
isInRTPCFiducial(vz, theta, phi){
  if( !isInRTPCDrift(vz, theta)   ) return false
  if(  isInRTPCSupport(phi)       ) return false
  if(  isInRTPCHolder(vz, theta)  ) return false
  return true
}
```

Failing any one of these other cuts results in rejection of the RTPC track entirely.

B.4.1 Drift Region Fiducial Cut

To ensure the track is coming inside the drift region, a fiducial cut is place:

```
isInRTPCDrift(vz, theta){
   if( abs(z1) > 10 ) return false
   if( abs(z2) > 10 ) return false
}
```

where `z1` and `z2` are the reconstructed particle's projected z-components when it hits the inner cathode, at `rinner`, and outer anode, at `router`, respectively:

```
z1 = (vz+64) + cos(theta)*rinner/abs(sin(theta))
z2 = (vz+64) + cos(theta)*router/abs(sin(theta))
```

with

```
rinner = 3

router = 6
```

in cm. The shift of 64 cm is to account for the target being placed at -64 cm with respect to the nominal center of CLAS.

B.4.2 Support Region Fiducial Cut

The left and right sides of the RTPC is separated by two mechanical supports, one at the top and and one at the bottom, with an azimuthal angular extent of 30°. Tracks reconstructed that hit these supports are rubbish. The cut is introduced to deal with these:

```
isInRTPCSupport(phi){
   if( abs(phi_shifted -  90) < 30 ) return false
   if( abs(phi_shifted - 270) < 30 ) return false
}
```

where `phi_shifted` is the reconstructed azimuthal angle, ϕ, in degrees, so that the top support is centered at `phi_shifted`= 90° and the bottom support is centered at `phi_shifted`= 270°

```
phi_shifted = phi
if( phi_shifted < 0 ) while( phi_shifted <  0    ) phi_shifted += 2*pi
else                  while( phi_shifted >= 2*pi ) phi_shifted -= 2*pi
```

B.4.3 Target Holder Fiducial Cut

To remove the tracks originating from the target holder, the fiducial cut is used:

```
isInRTPCHolder(vz, theta){
  cz = cos(theta)
  vz = 10 * (vz + 64)
  dz = z_targ - vz
  if( cz < cos( atan2(r_targ, dz) ) ) return false
}
```

where `vz` is shifted from the center of CLAS, `z_targ` is the position of the target's downstream end and `r_targ` is the target's radius:

```
r_targ =   2.5
z_targ = -84.0
```

are all in mm.

C. Solving for Kinematic Fitting Variables

The conditions to minimize the Lagrangian in **Section 8.2.1**:

$$\vec{\mathbf{0}} \equiv \frac{1}{2}\left(\frac{\partial\mathcal{L}}{\partial\vec{\boldsymbol{\delta}}}\right)^{\nu} = C_{\eta}^{-1}\vec{\boldsymbol{\epsilon}}^{\,\nu} + \left(B^{\nu}\right)^{T}\vec{\boldsymbol{\mu}}^{\nu} = C_{\eta}^{-1}\left(\vec{\boldsymbol{\delta}}^{\,\nu} + \vec{\boldsymbol{\epsilon}}^{\,\nu-1}\right) + \left(B^{\nu}\right)^{T}\vec{\boldsymbol{\mu}}^{\nu} \tag{C.1a}$$

$$\vec{\mathbf{0}} \equiv \frac{1}{2}\left(\frac{\partial\mathcal{L}}{\partial\vec{\boldsymbol{\mu}}}\right)^{\nu} = A^{\nu}\vec{\boldsymbol{\xi}}^{\,\nu} + B^{\nu}\vec{\boldsymbol{\delta}}^{\,\nu} + \vec{\boldsymbol{c}}^{\,\nu} \tag{C.1b}$$

$$\vec{\mathbf{0}} \equiv \frac{1}{2}\left(\frac{\partial\mathcal{L}}{\partial\vec{\boldsymbol{\xi}}}\right)^{\nu} = \left(\vec{\boldsymbol{\mu}}^{\nu}\right)^{T}A^{\nu} = \left(A^{\nu}\right)^{T}\vec{\boldsymbol{\mu}}^{\nu} \quad , \tag{C.1c}$$

where identity $\vec{\boldsymbol{\epsilon}}^{\,\nu} \equiv \vec{\boldsymbol{\delta}}^{\,\nu} + \vec{\boldsymbol{\epsilon}}^{\,\nu-1}$ is used in **Eq. C.1a** from the fact that:

$$\begin{aligned}
\vec{\boldsymbol{\epsilon}}^{\,\nu} &:= \vec{\boldsymbol{y}}^{\,\nu} - \vec{\boldsymbol{\eta}} = \vec{\boldsymbol{y}}^{\,\nu} - \vec{\boldsymbol{y}}^{\,0} \\
&= \vec{\boldsymbol{y}}^{\,\nu} + \left[\left(-\vec{\boldsymbol{y}}^{\,\nu-1} + \vec{\boldsymbol{y}}^{\,\nu-1}\right) + \ldots + \left(-\vec{\boldsymbol{y}}^{\,1} + \vec{\boldsymbol{y}}^{\,1}\right)\right] - \vec{\boldsymbol{y}}^{\,0} \\
&= \left(\vec{\boldsymbol{y}}^{\,\nu} - \vec{\boldsymbol{y}}^{\,\nu-1}\right) + \ldots + \left(\vec{\boldsymbol{y}}^{\,1} - \vec{\boldsymbol{y}}^{\,0}\right) \\
&= \sum_{j=1}^{\nu}\vec{\boldsymbol{\delta}}^{\,j} \quad .
\end{aligned}$$

To solve for each $\vec{\boldsymbol{\mu}}^{\nu}, \vec{\boldsymbol{\delta}}^{\,\nu}, \vec{\boldsymbol{\xi}}^{\,\nu}$ that satisfy **Eqs. C.1**s' conditions, we start with $\vec{\boldsymbol{\xi}}^{\,\nu}$, multiplying $\left[B^{\nu}C_{\eta}\right]$ to **Eq. C.1a**:

$$\begin{aligned}
\left[B^{\nu}C_{\eta}\right]\left(C_{\eta}^{-1}\left(\vec{\boldsymbol{\delta}}^{\,\nu} + \vec{\boldsymbol{\epsilon}}^{\,\nu-1}\right) + \left(B^{\nu}\right)^{T}\vec{\boldsymbol{\mu}}^{\nu}\right) &\equiv \vec{\mathbf{0}} \\
B^{\nu}\left(\vec{\boldsymbol{\delta}}^{\,\nu} + \vec{\boldsymbol{\epsilon}}^{\,\nu-1}\right) + \left[B^{\nu}C_{\eta}\left(B^{\nu}\right)^{T}\right]\vec{\boldsymbol{\mu}}^{\nu} &\equiv \vec{\mathbf{0}}
\end{aligned}$$

$$\Rightarrow \qquad B^{\nu}\vec{\boldsymbol{\delta}}^{\,\nu} = -\left(\left[B^{\nu}C_{\eta}\left(B^{\nu}\right)^{T}\right]\vec{\boldsymbol{\mu}}^{\nu} + B^{\nu}\vec{\boldsymbol{\epsilon}}^{\,\nu-1}\right) \quad . \tag{C.2}$$

Rearranging **Eq. C.1b** and equating expressions for $-B^{\nu}\vec{\boldsymbol{\delta}}^{\,\nu}$ with **Eq. C.2**, we obtain

$$A^{\nu}\vec{\boldsymbol{\xi}}^{\,\nu} + \vec{\boldsymbol{c}}^{\,\nu} = \left[B^{\nu}C_{\eta}\left(B^{\nu}\right)^{T}\right]\vec{\boldsymbol{\mu}}^{\nu} + B^{\nu}\vec{\boldsymbol{\epsilon}}^{\,\nu-1}$$

$$A^{\nu}\vec{\boldsymbol{\xi}}^{\,\nu} + \vec{\boldsymbol{c}}^{\,\nu} - B^{\nu}\vec{\boldsymbol{\epsilon}}^{\,\nu-1} = \left[B^{\nu}C_{\eta}\left(B^{\nu}\right)^{T}\right]\vec{\boldsymbol{\mu}}^{\nu} \quad . \tag{C.3}$$

Eliminating the $\vec{\mu}$ term by using **Eq. C.1c**, we have

$$\left[(A^\nu)^T C_B^\nu\right]\left(A^\nu \vec{\xi}^{\,\nu} + \vec{c}^{\,\nu} - B^\nu \vec{\epsilon}^{\,\nu-1}\right) = \left[(A^\nu)^T C_B^\nu\right]\left[B^\nu C_\eta (B^\nu)^T\right]\vec{\mu}^{\,\nu}$$

where C_B^ν is defined as

$$C_B^\nu := \left[B^\nu C_\eta (B^\nu)^T\right]^{-1} \quad .$$

Then,

$$\left[(A^\nu)^T C_B^\nu\right]\left(A^\nu \vec{\xi}^{\,\nu} + \vec{c}^{\,\nu} - B^\nu \vec{\epsilon}^{\,\nu-1}\right) \equiv \vec{\mathbf{0}}$$

$$\Rightarrow \left[(A^\nu)^T C_B^\nu A^\nu\right]\vec{\xi}^{\,\nu} = -\left[(A^\nu)^T C_B^\nu\right]\left(\vec{c}^{\,\nu} - B^\nu \vec{\epsilon}^{\,\nu-1}\right)$$

$$\vec{\xi}^{\,\nu} = -C_x^\nu \left[(A^\nu)^T C_B^\nu\right](\vec{r}^{\,\nu}) \tag{C.4}$$

where $\vec{r}^{\,\nu}$ and C_x^ν are defined as

$$\begin{aligned} \vec{r}^{\,\nu} &:= \vec{c}^{\,\nu} - B^\nu \vec{\epsilon}^{\,\nu-1} \\ C_x^\nu &:= \left[(A^\nu)^T C_B^\nu A^\nu\right]^{-1} \end{aligned} \quad ,$$

respectively.

To get $\vec{\mu}^{\,\nu}$ we go back and rewrite **Eq. C.3** with our newly defined variables:

$$\left(C_B^\nu\right)^{-1} \vec{\mu}^{\,\nu} = A^\nu \vec{\xi}^{\,\nu} + \vec{r}^{\,\nu}$$

$$\vec{\mu}^{\,\nu} = C_B^\nu \left(A^\nu \vec{\xi}^{\,\nu} + \vec{r}^{\,\nu}\right) \tag{C.5}$$

Finally, to get $\vec{\delta}^{\,\nu}$, we go back to **Eq. C.2**:

$$B^\nu \vec{\delta}^{\,\nu} = -\left(\left[B^\nu C_\eta (B^\nu)^T\right]\vec{\mu}^{\,\nu} + B^\nu \vec{\epsilon}^{\,\nu-1}\right)$$

$$\vec{\delta}^{\,\nu} = -C_\eta (B^\nu)^T \vec{\mu}^{\,\nu} - \vec{\epsilon}^{\,\nu-1} \tag{C.6}$$

- -

In summary, we obtain the vectors that minimize the Lagrangian **Eq. 8.1**, meeting minimization conditions **Eq. 8.1** that are listed in **Eq. 8.2** and below:

$$\vec{\boldsymbol{\xi}}^{\nu} = -C_x^{\nu} \left(A^{\nu}\right)^T C_B^{\nu} \vec{\boldsymbol{r}}^{\nu}$$

$$\vec{\boldsymbol{\mu}}^{\nu} = C_B^{\nu} \left(A^{\nu} \vec{\boldsymbol{\xi}}^{\nu} + \vec{\boldsymbol{r}}^{\nu}\right)$$

$$\vec{\boldsymbol{\delta}}^{\nu} = -C_{\eta} \left(B^{\nu}\right)^T \vec{\boldsymbol{\mu}}^{\nu} - \vec{\boldsymbol{\epsilon}}^{\nu-1}$$

References

[1] B. Torayev, “Electroproduction of Neutral Pion Off ^{4}He,” *CLAS Note*, December 2016.

[2] C. Patrignani *et al.*, “Review of Particle Physics,” *Chin. Phys.*, vol. C40, no. 10, p. 100001, 2016.

[3] K. O. et al., “Review of Particle Physics,” *Chin. Phys.*, vol. C38, p. 090001, 2014.

[4] M. Hattawy, *Deeply Virtual Compton Scattering Off ^{4}He*. PhD thesis, Institut de Physique NuclÃľaire (IPN), September 2015.

[5] A. G. Frodesen, O. Skjeggestad, and H. Tofte, *Probability and Statistics in Particle Physics*. Universitetsforlaget, 1971.

[6] M. Williams and C. A. Meyer, “Kinematic Fitting in CLAS,” *CLAS Note*, November 2003.

[7] M. Williams, D. Applegate, and C. A. Meyer, “Determining Momentum and Energy Corrections for g1c Using Kinematic Fitting,” *CLAS Note*, June 2004.

[8] P. T. Mattione, “Kinematic Fitting of Detached Vertices,” Master’s thesis, Rice University, 2007.

[9] P. T. Mattione and D. S. Carman, “CLAS g13 Experiment Studies,” *CLAS Note*, 2017.

[10] D. Keller, “Techniques in Kinematic Fitting,” *CLAS Note*, November 2010.

[11] N. Baltzell, *A Search for the Exotic Θ^+ Pentaquark in $\gamma d \to ppK^0K^-$*. PhD thesis, University of South Carolina, September 2001.

[12] B. A. Mecking *et al.*, “The CEBAF Large Acceptance Spectrometer (CLAS),” *Nucl. Instrum. Meth.*, vol. A503, pp. 513–553, 2003.

[13] M. M. et al, “The CLAS Drift Chamber System,” *Nuclear Instruments and Methods in Physics Research Section A: Accelerators, Spectrometers, Detectors and Associated Equipment*, vol. 449, no. 1, pp. 81 – 111, 2000.

[14] H.-S. Jo, *Deeply Virtual Compton Scattering on the Nucleon with the CLAS Detector of Jefferson Lab : Measurement of the polarized and unpolarized Cross Sections*. Theses, Université Paris Sud - Paris XI, Mar. 2007.

[15] M. Hattawy, N. A. Baltzell, and R. Dupré, “First Exclusive Measurement of Deeply Virtual Compton Scattering off ^{4}He: Toward the 3D Tomography of Nuclei,” *Phys. Rev. Lett.*, vol. 119, p. 202004, Nov 2017.

[16] M. A. et al, “The CLAS Forward Electromagnetic Calorimeter,” *Nuclear Instruments and Methods in Physics Research Section A: Accelerators, Spectrometers, Detectors and Associated Equipment*, vol. 460, no. 2, pp. 239 – 265, 2001.

[17] H. A. et al, “Deeply Virtual Compton Scattering with CLAS at 6 GeV,” *Research Proposal to Jefferson Lab PAC*, vol. PAC 29 PR 06-003, 2005.

[18] K. H. et al, “Deeply Virtual Compton Scattering off ^{4}He,” *Research Proposal to Jefferson Lab PAC*, vol. PAC 33 PR 08-024, 2007.

[19] W. R. Leo, *Techniques for Nuclear and Particle Physics Experiments*. Springer-Verlag, 1994.

[20] N. Baltzell, “EG6 EC Sampling Fraction Time Dependence Correction,” August 2013. https://clasweb.jlab.org/rungroups/lowq/wiki/index.php/EG6_EC_Sampling_Fraction_Time-Dependence_Correction.

[21] F. Girod, “Simulation of CLAS/DVCS Inner Calorimeter: Optimization of Position Resolution, Edge Effects and Fiducial Cuts, Photon Energy Reconstruction, and Neutral Pions Events,” *CLAS Note*, November 2005.

[22] N. Baltzell and S. Stepanyan, “Beam XY-Position at the Target for CLAS/EG6,” *CLAS Note*, April 2013.

[23] N. Baltzell, “RTPC Vertex and Angle Correction,” August 2013. https://clasweb.jlab.org/rungroups/lowq/wiki/index.php/User:RTPC_Vertex_and_Angle_(Aug_7,_2013).